FUGRO CONSULTANTS, INC.

UPDATE OF THE THREE-DIMENSIONAL VELOCITY MODEL FOR THE DIABLO CANYON POWER PLANT (DCPP) FOUNDATION AREA

Prepared for:
PACIFIC GAS AND ELECTRIC

May 2015
Fugro Job No. 04.76140022

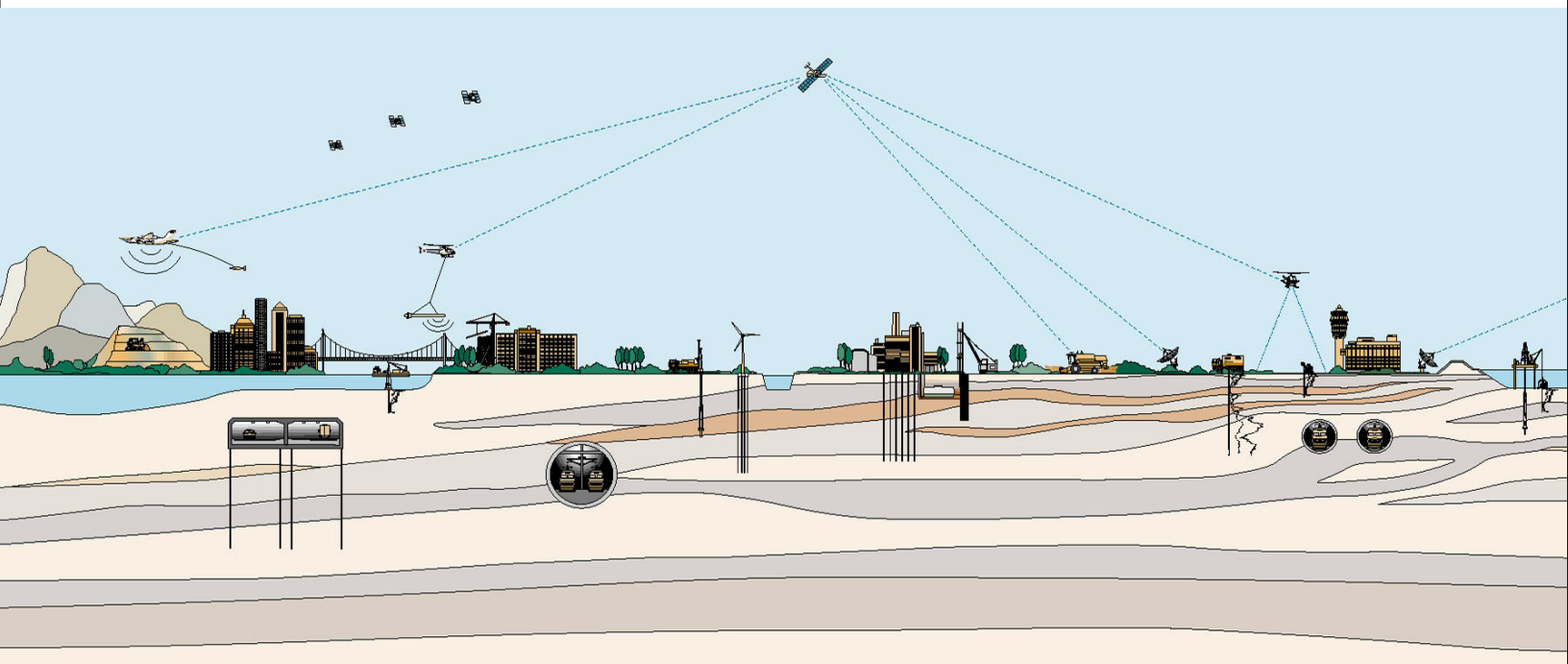

FUGRO CONSULTANTS, INC.

1000 Broadway, Suite 440
Oakland, California 94607
Tel: (510) 268-0461
Fax: (510) 268-0137

May 29, 2015
Project No. 04.76140022

Pacific Gas and Electric
77 Beale Street #100
San Francisco, California 94105

Attention: Dr. Norm Abrahamson

Subject: Update of the Three-Dimensional Velocity Model for the Diablo Canyon Power Plant (DCPP) Foundation Area

Dear Dr. Norm Abrahamson:

Fugro Consultants Inc. is providing engineering services to Pacific Gas and Electric (PG&E) for the Diablo Canyon Power Plant (DCPP) under the work authorization (CWA No. 2501115798). This report presents the methodology and results of the update and validation of the three-dimensional velocity model for the DCPP Foundation Area. We thank you for the opportunity to work on this project and are looking forward to continuing providing our services in the future. Should you have any questions don't hesitate to contact Thaleia Travasarou at +1 (510) 267-4410 or by e-mail at ttravasarou@fugro.com.

Sincerely,

FUGRO CONSULTANTS, INC.

Wei-Yu Chen, Ph.D., P.E., G.E.
Principal Engineer

REGISTERED PROFESSIONAL ENGINEER
CHEN WEI-YU
No. GE3068
Expires 12/31/15
GEOTECHNICAL
STATE OF CALIFORNIA

Alfredo Fernandez, Ph.D., P.E.
Senior Engineer

REGISTERED PROFESSIONAL ENGINEER
J. ALFREDO FERNANDEZ
No. 76905
Exp. 12/31/2016
CIVIL
STATE OF CALIFORNIA

Daniel R.H. O'Connell, Ph.D.
Senior Principal Geophysicist

Thaleia Travasarou, Ph.D., P.E., G.E.
Principal Engineer

REGISTERED PROFESSIONAL ENGINEER
THALEIA TRAVASAROU
No. GE3034
Exp. 6/30/16
GEOTECHNICAL
STATE OF CALIFORNIA

Copies Submitted: (1) PDF, Addressee

CONTENTS

TABLES

FIGURES

APPENDICES

1.0 INTRODUCTION

An estimate of the tree-dimensional (3-D) acoustic-wave (Vp) and shear-wave (Vs) velocity structure beneath the Diablo Canyon Power Plant (DCPP) foundation area was provided in Chapter 10 of PG&E (2014b). The estimated 3-D Vs structure was derived starting with a 3-D Vp structure obtained from a 3-D traveltime-gravity inversion of active seismic data collected in 2011 and 2012 in the Irish Hills and the DCPP foundation area (FCL, 2014a) as discussed in Chapter 10 of PG&E (2014b). Surface-wave dispersion constraints from six locations north and west of the DCPP foundation area provided the Vp/Vs-depth functions used to estimate 3-D Vs from 3-D Vp. No specific Vs-depth constraints were used in the southern or eastern portions of the DCPP foundation area in the construction of the 3-D Vs model for the DCPP foundation. Quantitative estimates of 3-D Vs uncertainties were provided in Chapter 10 of PG&E (2014b).

The progress report of Fugro (2015) documented 3-D dynamic numerical analyses to assess the effects of the 3-D velocity structure on the local site response in the immediate vicinity of the Diablo Canyon Power Plant (DCPP). The 3-D velocity structure discussed above was used in these analyses. The progress and analytical results documented in Fugro (2015) were presented to a peer review panel during four review meetings held between December 18th, 2014 and February 6th, 2015.

After the review meeting held on February 6th, the review panel raised comments associated primarily with the need for additional 3-D velocity model calibration to increase confidence in the numerical model and analytical approach. The reviewers recommended to update the 3-D velocity model to better fit existing data and potentially consider larger uncertainty.

Following the recommendations of the reviewers, additional active seismic data collected during the 2012 Vibroseis field program that operated within the DCPP foundation area and over several kilometers of the surrounding area are presented and analyzed in this report. These additional data from 100 sites and Vs traveltime measurements from three deep boreholes in the DCPP foundation area provide more specific Vs-depth constraints over a larger portion of the DCPP foundation and surrounding area. Surface-wave dispersion and full-waveform analyses provide quantitative estimates of 3-D Vs uncertainties for the DCPP foundation area.

Resulting Vs-depth and lateral changes in Vs across the DCPP foundation area strongly correlate with first-order geology. In particular, the largest changes in Vs-depth and lateral changes in Vs observed in the region containing the DCPP foundation are associated with velocity differences between shallow sedimentary deposits, highly weathered rock, and relatively unweathered rock in the subsurface, and large-scale lateral variations in first-order geologic structure. Thus, it is important to understand first-order geologic characteristics of the DCPP foundation area and surrounding area to understand the 3-D Vs structure observed in the DCPP foundation area.

1.1 GEOLOGIC SETTING OF THE DCPP FOUNDATION

Bedrock in DCPP's vicinity includes highly deformed Mesozoic and Cenozoic sedimentary and volcanic rocks. Foundations of principal plant buildings are founded directly on

volcaniclastic rocks of the Miocene Obispo Formation (Fm.). The geology of DCPP's site area consists of Tertiary Obispo Fm. resistant tuff, volcaniclastic strata, and later-stage Obispo Fm. diabase that intruded into the Obispo Fm. volcaniclastics, Quaternary surficial deposits, and engineered fill.

Four map-scale Obispo Fm. sub-units, or lithofacies, are recognized within the DCPP site area. From oldest to youngest, these sub-units are as follows: a) Resistant, bedded to massive tuffaceous rocks, including possible "peperite," a near-source intrusive tuff (Tmor) b) Bedded, shaley siltstone with tuffaceous fine sandstone interbeds (Tmofc) c) Bedded, tuffaceous and dolomitized fine sandstone and siltstone (Tmofb) d) Massive to jointed diabase (Tmod). The diabase sub-unit intrudes all the other lithologies, and thus is the youngest (PG&E 2014b, Chapter 9).

Diabase is widely distributed around the DCPP foundation area (Figure 1.1-1) but is not present in the mapped DCPP foundation. The distribution of diabase relative to the DCPP foundation is relevant because diabase and possibly nearby regions of dolomitic alteration are associated with Vp velocities 2-3 times larger than non-diabase Obispo Fm lithofacies Vp. Thus, to first-order seismic velocities are likely to scale in inverse proportion to distance from diabase intrusives.

Magnetic noise from the DCPP turbines, transmission lines, and containment structures preclude recovering meaningful magnetic anomaly signals in the DCPP foundation area but helicopter magnetic measurements illustrate how saucer-shaped subsurface diabase complexes are distributed around the DCPP region (Figure 1.1-2). Saucer-shaped sills are associated with shallow intrusion into relatively weak, and often anisotropic, sedimentary sequences (Galland et al., 2009; Gressier et al., 2010) typical of the Obispo Fm. Saucer-shaped diabase intrusive complexes are particularly well imaged in 3-D seismic data (Malthe-Sørenssen et al., 2004; Hansen and Cartwright, 2006a,b; Cartwright and Hansen, 2006; Poulteau et al., 2008), particularly when combined with gravity and magnetic data (Rocchi et al., 2007).

A large-scale saucer-shaped diabase sill complex is particularly well imaged in active-seismic 3-D traveltime-gravity Vp tomography 100-200 m east and northeast of the DCPP foundation area at the north-south cross-section position shown in Figure 1.1-3 as presented in Figure 1.1-4 in 3-D perspective relative to Diablo Cove and the DCPP. The closest large-scale diabase to the west side of the DCPP foundation is located about 300-400 m offshore of the DCPP (Figures 1.1-1 and 1.1-2). Thus, the east side of the DCPP foundation is closest to a large-scale diabase intrusive and is the portion of the DCPP foundation most likely to have elevated seismic velocities associated with diabase intrusion and related dolomitic alteration. The rest of the DCPP foundation area is in a local hole between intrusive complexes located on virtually all sides of the larger area containing the DCPP foundation (Figures 1.1-1 and 1.1.2).

1.2 HIGH-RESOLUTION SUSPENSION LOG VS-DEPTH MEASUREMENTS

Vs-depth estimates at 0.5 m intervals are available from two boreholes located within 60 m of each other (Agbabian Associates, 1998) in the footprint of the Independent Spent Fuel Storage Installation (ISFSI) northeast of the DCPP foundation area as shown in Figure 1.1-3. These suspension-log data provide the highest resolution Vs-depth measurements in the larger area near the DCPP foundation and extend to 60-68 m depth. Suspension-log velocity measurements were performed in three cased boreholes designated BA 93-1, 93-3 and 93-4. In

borehole BA 93-1, it was not possible to continue logging below a depth of 44 m due to abandoned steel casing in borehole 93-1. Consequently, a second borehole, 93-4, was placed within 8 m of BA 93-1 to continue velocity logging to 68 m depth. Vs-depth data are combined from BA 93-1 and 93-4 (93-1-4) to obtain a Vs-depth profile over a comparable depth range to BA 93-3 (Figure 1.2-1). Since the boreholes started at elevations of 98.3 m (BA 93-3) and 113.6 (BA 93-1 and 93-4) the bottoms of both ISFSI boreholes are located above sea level.

The two boreholes show substantial short-wavelength (0.5 m depth spacing) velocity variability in the left plot in Figure 1.2-1. Averaging the 0.5 m depth samples of Vs using a 3-m-wide boxcar average (right-plot in Figure 1.2-1) simulates depth resolution comparable to surface-wave dispersion constraints. The right plot of smoothed Vs-depth in Figure 1.2-1 shows that intervals of velocity reversal (low-velocity zones) are characteristic of Obispo Formation Vs-depth in the 10-60 m depth range in the ISFSI area even after smoothing. The Vs oscillations with depth correlate with 1-10-m-thick alternating depth intervals of dolomitic alternation and unaltered Obispo Fm. noted in borehole logging (WLA, 2001). Ln-mean Vs in both boreholes in the 5-40.5 m depth interval (blue and orange lines) illustrate that long-wavelength velocity variations are relatively small over the 60 m borehole separation distance with ln-mean Vs differences of < 5% (1154 m/s for BA 93-3 and 1209 m/s for BA 93-1-4). The ln-mean of the 0.5 m depth interval Vs estimates between the two boreholes has short-wavelength median ln-standard-deviation of 0.11 but is consistently centered close to the long-wavelength Vs-depth of both boreholes.

The depth where Vs substantially increases varies from 46 m in borehole 93-3 to 53 m in borehole 93-1-4. This depth difference is a 13% difference in the depth or a 16% difference in elevation (accounting for the borehole elevations) to the change to significantly higher velocities in each borehole over a separation distance of 60 m between the boreholes. This is a more significant change in lateral velocity than observed in the shallow rock.

As illustrated in Figures 1.1-3 and 1.1-4, these ISFSI boreholes are located above and close to large-scale diabase intrusive complex that occurs at depths of 50-150 m below sea level near the boreholes. The closest portion of the diabase intrusive complex indicated by Vp of 5-6 km/s in Figure 1.1-4 is about 50-100 m below the bottom of the two boreholes. Thus, the ISFSI suspension log boreholes are located much closer to large-scale shallow diabase intrusive bodies than the DCPP foundation. Average Vs measured near the bottom of the ISFSI boreholes at depths of 45-60 m and greater is 1500-1900 m/s (Figure 1.2-1).

1.3 EXTENT OF DCPP FOUNDATION EXCAVATION

Foundation excavation at the DCPP removed surficial deposits over an area extending beyond the principal DCPP structures of the turbine building, the containment structures, and the auxiliary buildings (Figure 1.3-1). As noted in Chapters 9 and 10 of PG&E (2014b) and FCL (2014), the largest velocity variations in the DCPP area and the Irish Hills, in general, were observed in the first 5-10 m of depth. Over most of the span of the DCPP turbine building, the containment structures, and the auxiliary buildings the depth of excavation exceeds 5 m (Figures 1.3-1 and 1.3-2).

Foundation excavation removed surficial material (soil, colluvium, and the shallowest portions of weathered rock, etc.) to expose a portion of the weathering rind of the Obispo Fm. Excavation to a consistent excavation-equipment rippability (Caterpillar, 2000) exposed bedrock

marine terrace surfaces mapped in boring investigations in and around the DCPP foundation area (PG&E, 1989) as shown in Figure 1.3-2. Generally, the most variability of Vs is associated with surficial deposits. Consequently, the shallow variability of Vs in the DCPP excavated foundation area may be lower than observed in areas where surficial deposits were not excavated.

1.4 ORGANIZATION OF THE REPORT

Data and analyses of surface wave dispersion to estimate Vs-depth and 100 sites in the DCPP foundation area are presented in Section 2.0 along with Vs-depth uncertainties. The update and analysis, verification, and validation of the 3-D velocity model are presented in Section 3.0. A discussion of the results is presented in Section 4.0.

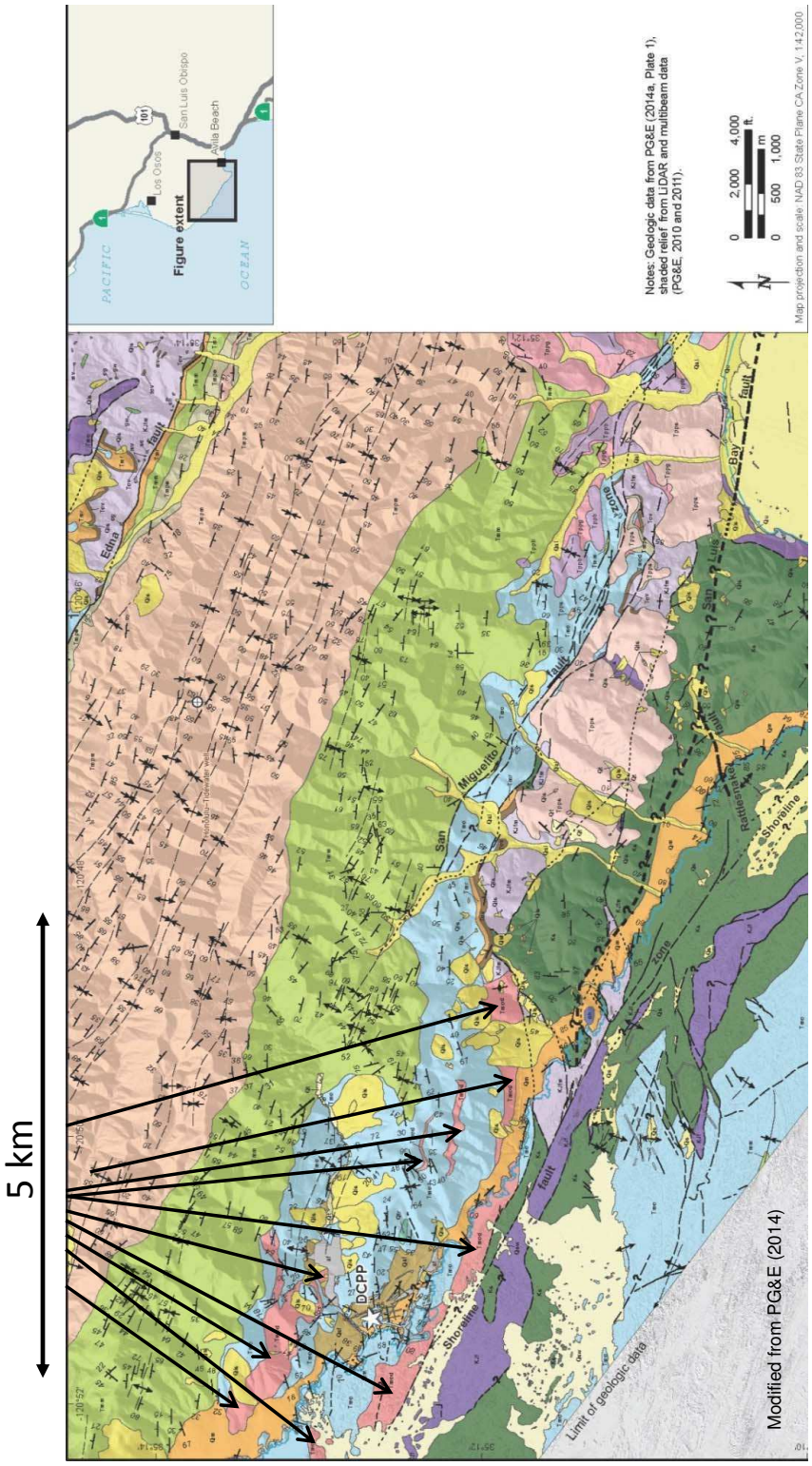

DIABASE/BASALT OUTCROP LOCATIONS SURROUNDING THE DCPP
Update of the 3−D Velocity Model for the DCPP Foundation Area
San Luis Obispo, California

FIGURE 1.1−1

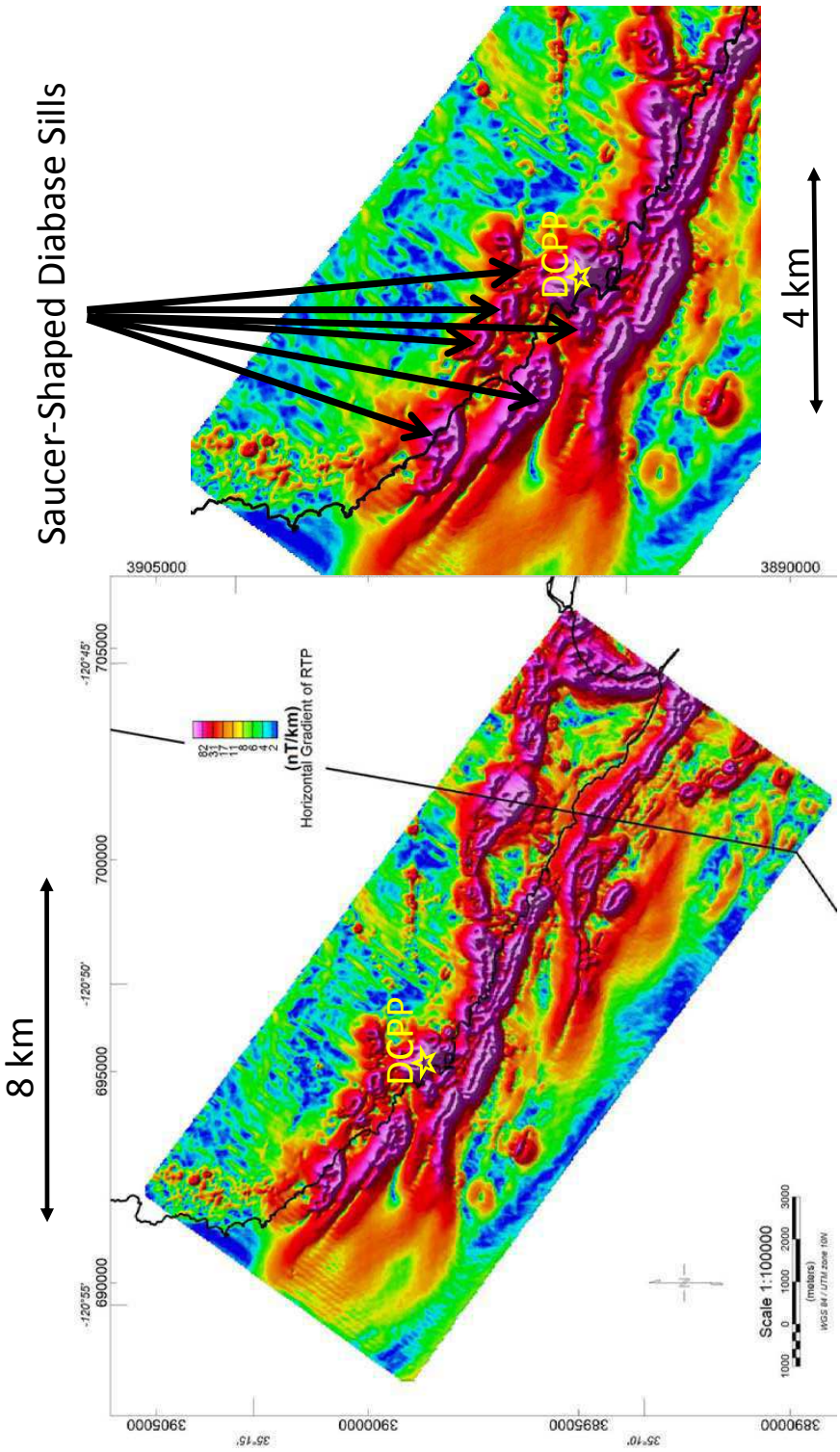

MAP OF HORIZONTAL GRADIENT OF HELICOPTER MAGNETIC RTP ANOMALY FIELD AND LOCATIONS OF SAUCER−SHAPED SILLS

Update of the 3−D Velocity Model for the DCPP Foundation Area
San Luis Obispo, California

FIGURE 1.1−2

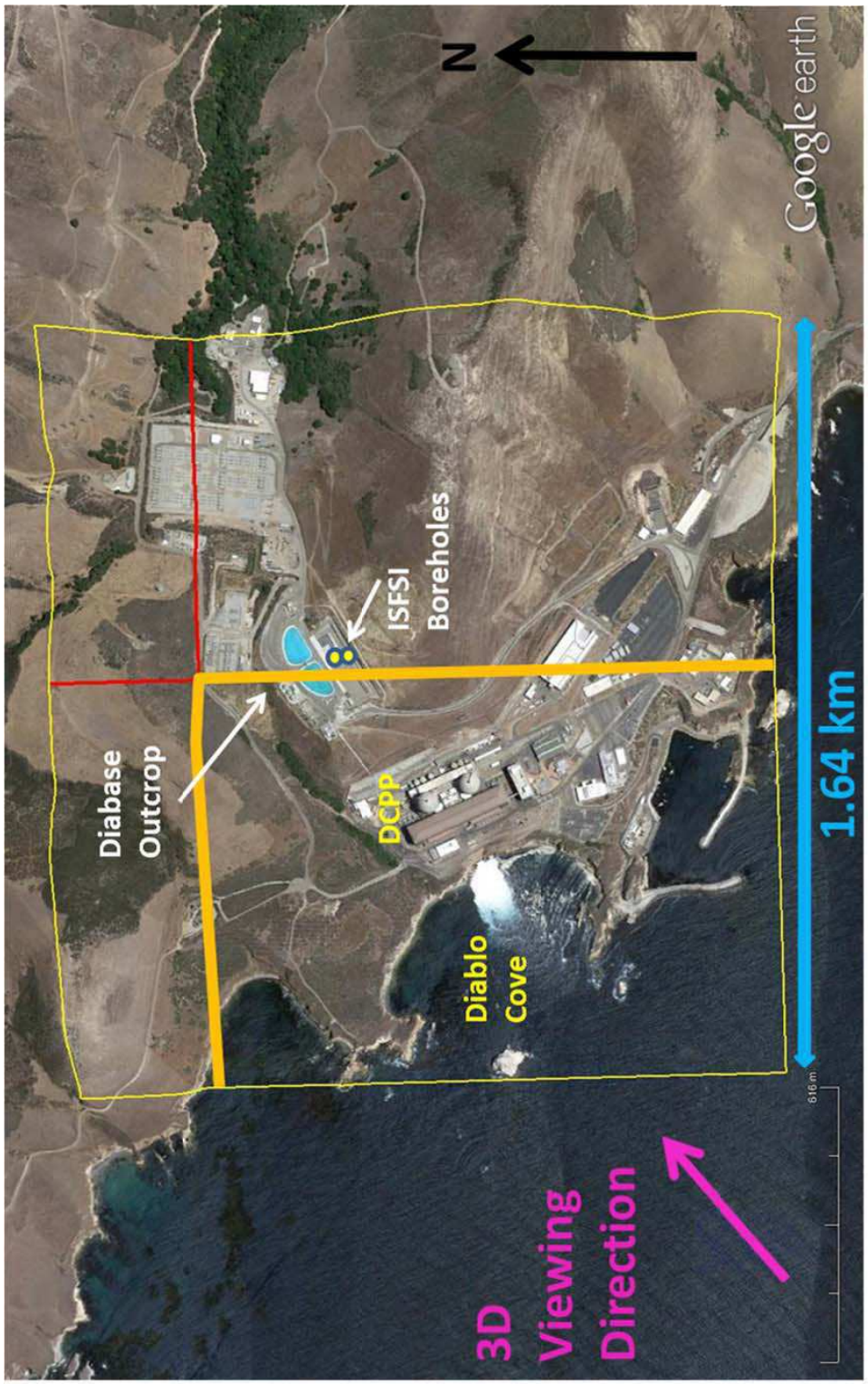

MAP SHOWING THE PORTIONS OF 3D VP PERSPECTIVE SLICES (THICK ORANGE LINES) VISIBLE IN FIGURE 1.1−4
Update of the 3−D Velocity Model for the DCPP Foundation Area
San Luis Obispo, California

FIGURE 1.1−3

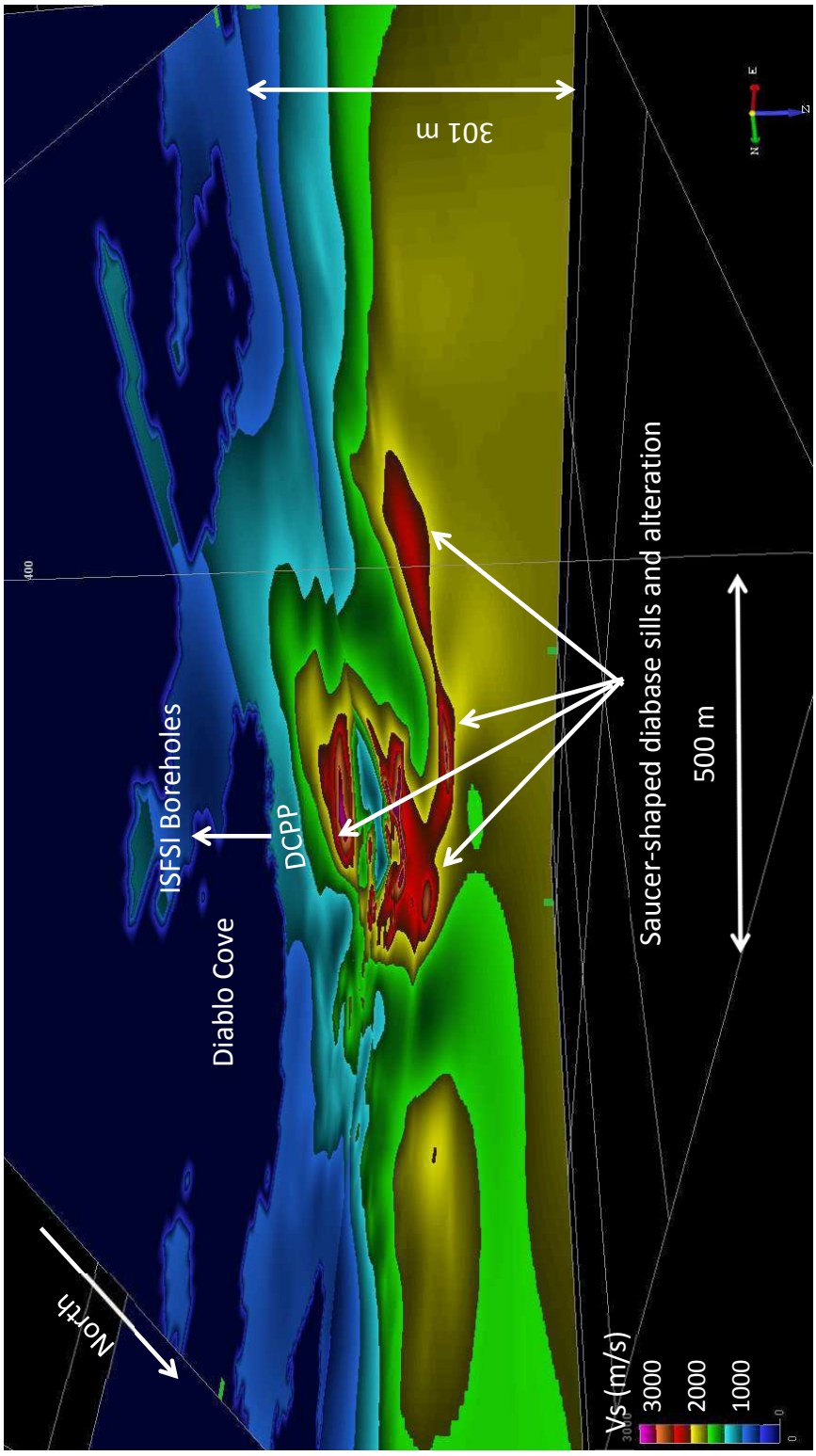

3D PERSPECTIVE OF THE TWO VP−DEPTH CROSS SECTIONS SLICES AND SEA LEVEL ELEVATION SLICE SHOWN IN FIGURE 1.1−3
Update of the 3−D Velocity Model for the DCPP Foundation Area
San Luis Obispo, California

FIGURE 1.1−4

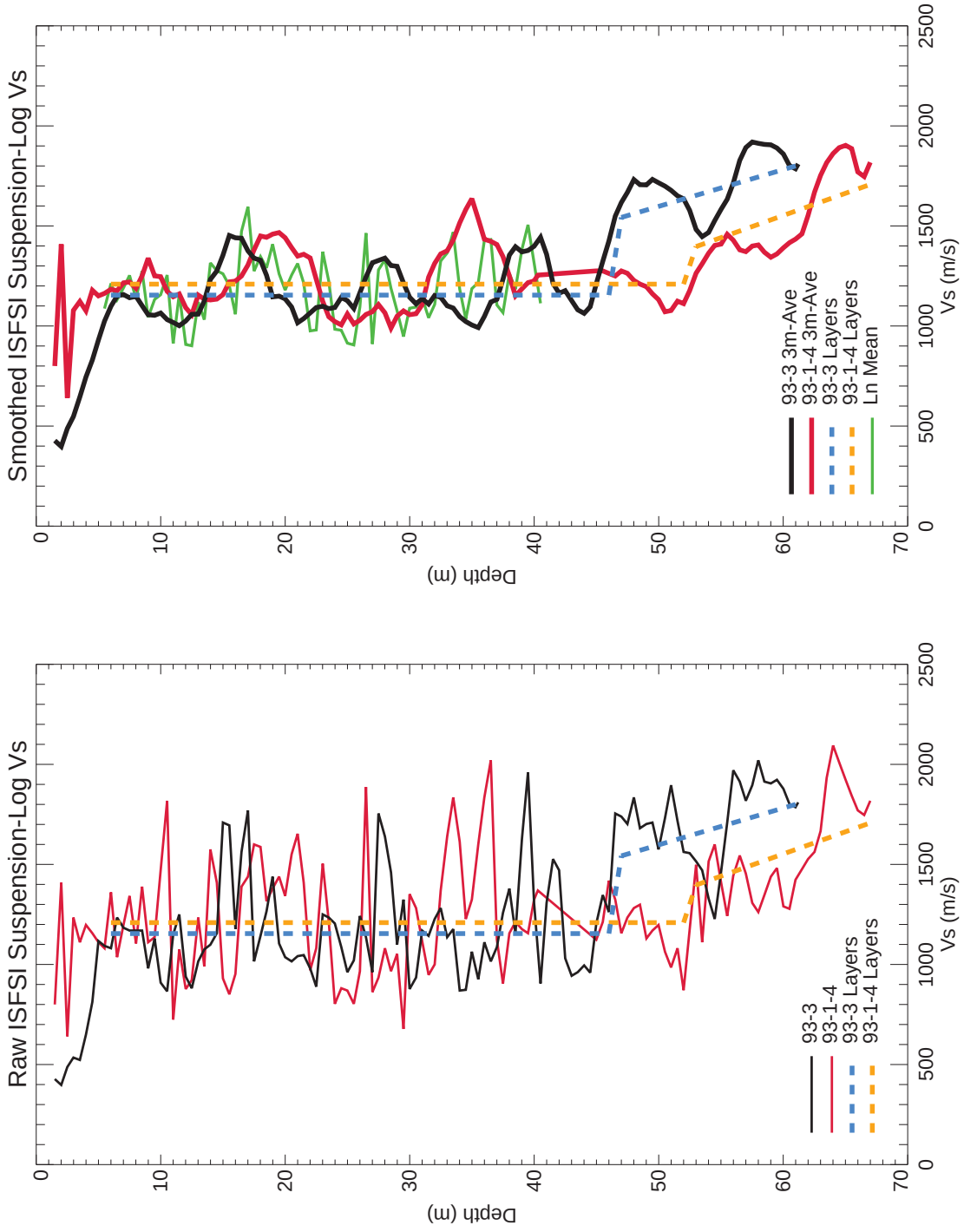

ISFSI SUSPENSION−LOG DEPTH RAW (LEFT) AND SMOOTHED (RIGHT) VS− PROFILES
Update of the 3−D Velocity Model for the DCPP Foundation Area
San Luis Obispo, California

FIGURE 1.2−1

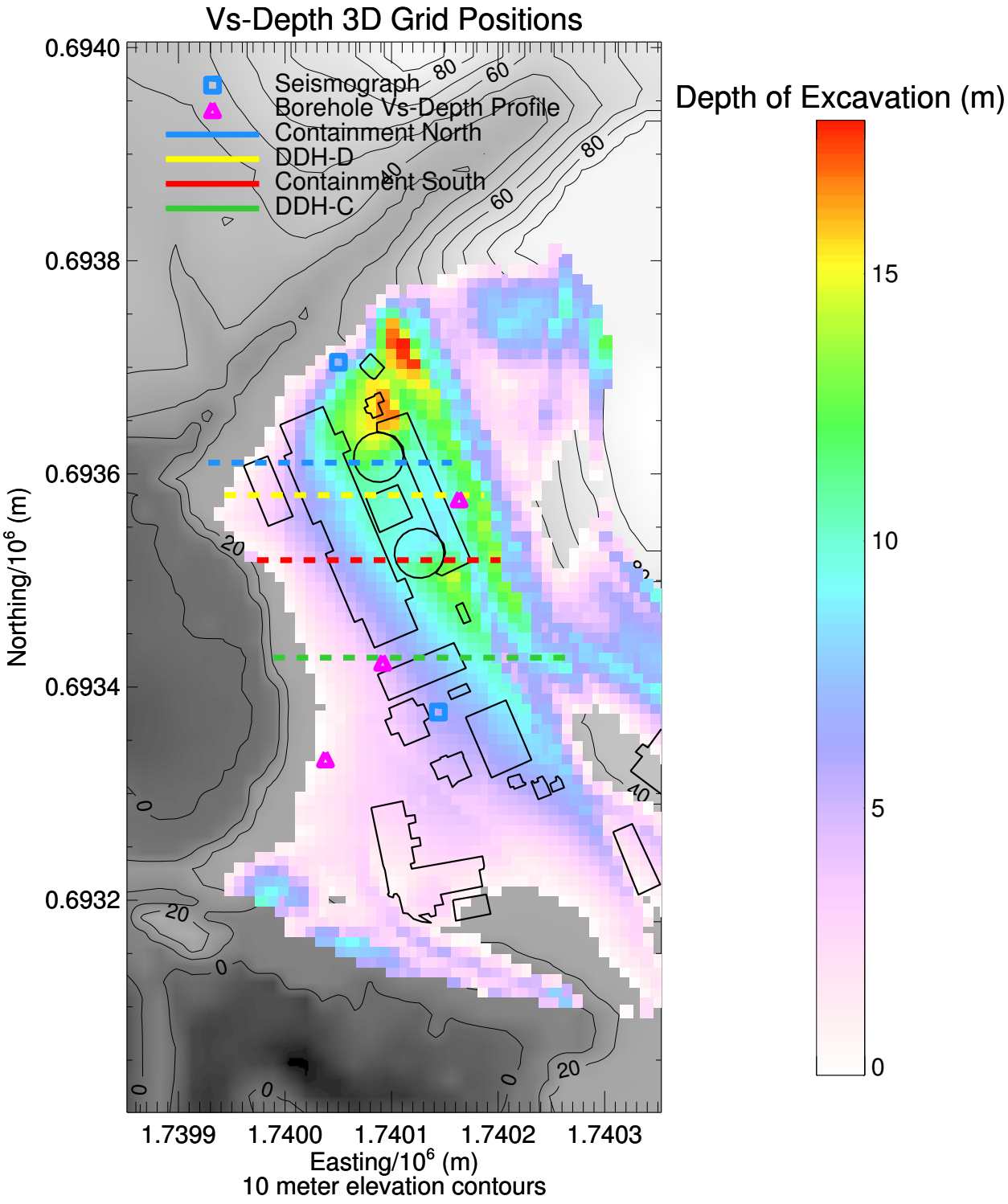

COLOR−SHADING SHOWING DEPTH OF EXCAVATION IN THE DCPP FOUNDATION AREA
Update of the 3−D Velocity Model for the DCPP Foundation Area
San Luis Obispo, California

FIGURE 1.3−1

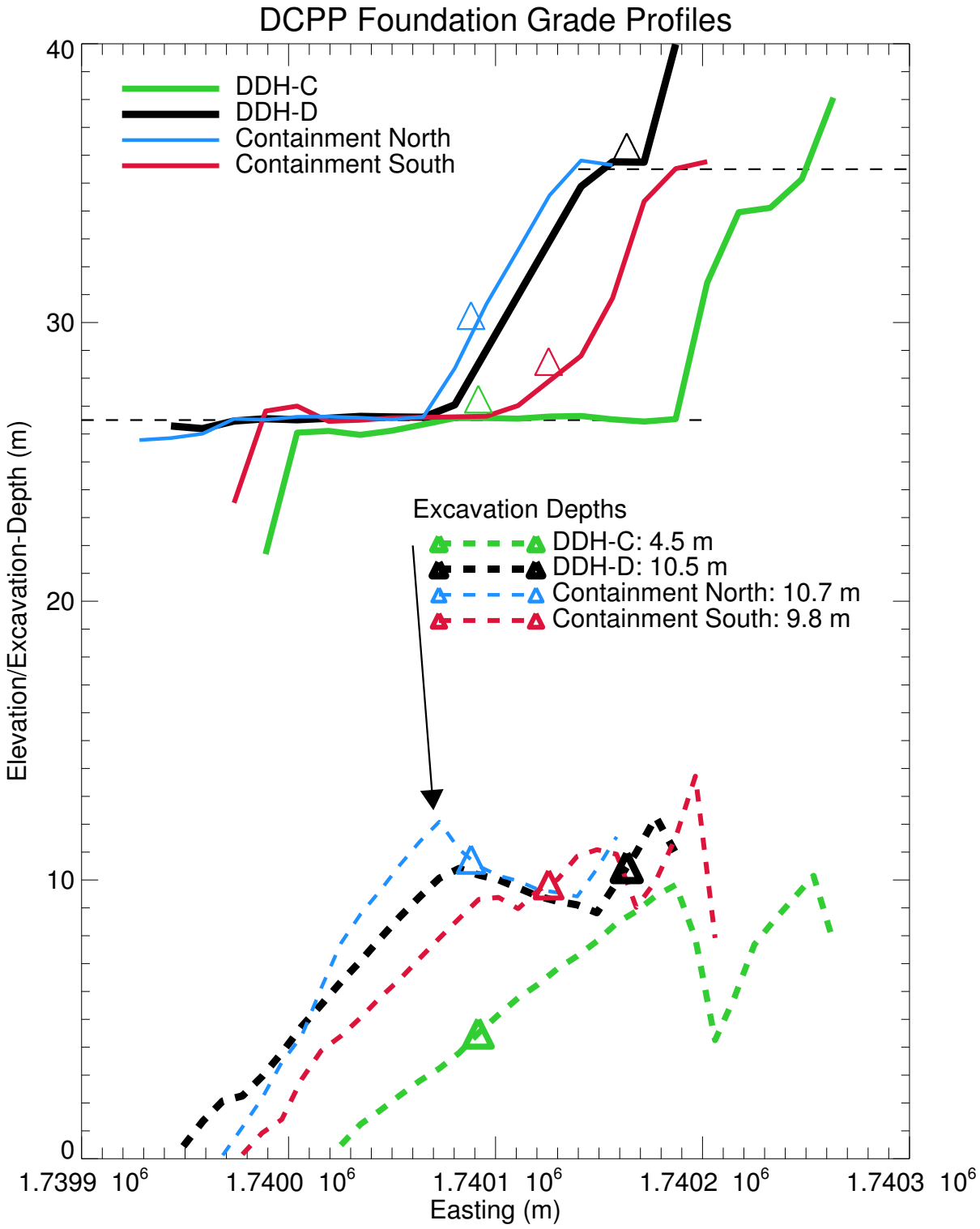

DCPP FOUNDATION ELEVATION AND EXCAVATION DEPTH PROFILES
Update of the 3−D Velocity Model for the DCPP Foundation Area
San Luis Obispo, California

FIGURE 1.3−2

2.0 UPDATE OF THE 3-D VS MODEL

The original 3-D DCPP Vs model (Chapter 10 of PG&E, 2014b) was based on Vp/Vs-depth functions used to convert a 3-D Vp to Vs. Vs-depth estimates from surface-wave dispersion obtained at six positions (Figure 2.0-1) were used to calculate Vs/Vp-depth adjustments to convert 3-D Vp to 3-D Vs (Chapter 10 of PG&E, 2014b). In this section additional surface-wave dispersion are presented and used to update the original 3-D Vs model from Chapter 10 of PG&E (2014b) and to develop estimates of 3-D Vs-depth uncertainties and spatial variability. These surface-wave dispersion analyses are followed by additional 3-D Vs model refinements and uncertainty analyses using Vibroseis ground motion time history data and full-waveform modeling in Section 3.

Critical evaluation of the reliability and resolution of non-invasive surface-wave methods to estimate Vs-depth have been the focus of several intensive investigations. The most comprehensive analyses has been conducted as the InterPacific (Intercomparison of methods for site parameter and velocity profile characterization) project to assess the reliability of seismic site characterization methods (borehole and surface-wave methods) used for estimating Vs-depth profiles and corresponding lumped parameters (e.g. Vs_{30} [time-weighted average shear wave velocity in the top 30 meters]) summarized by Garofalo et al. (2015). The InterPacific project used three different sites, representative of different geological conditions relevant for the evaluation of seismic site response effects. These sites include, a hard rock outcrop, a deep soft deposit, and an intermediate case with thick stiff soils, a velocity inversion and large bedrock depth. Two to three boreholes have been drilled at these sites and various companies were invited to perform in-hole measurements (cross-hole, down-hole and PS-logging). Both active and passive surface wave data were also collected, all of them located in the vicinity of the boreholes for a better comparison between the results from invasive and non-invasive methods. The same experimental non-invasive datasets without any prior information about the sites were provided to 14 different teams, which were asked to retrieve the Vs profiles working on the preferred subset of available experimental data. For surface-wave methods, results outline that the dispersion curves provided by the participants were in very good agreement with each other. Inverted Vs profiles were also found to be very consistent at least in the reliable resolution depth range of these techniques. Results from invasive methods show a variability of Vs estimates of the same order as the variability of Vs estimates obtained from non-invasive methods.

A key InterPacific project finding is that surface-wave methods provide Vs estimates with comparable variability to invasive methods. Surface-wave dispersion measurements provide a comparable Vs resolution alternative to invasive methods where site access is difficult or impossible due to a large number of buildings and facilities that prevent invasive measurements at many locations at a site. Surface waves can probe Vs structure below small buildings with small foundations where invasive measurements cannot be made. However, within the DCPP foundation area there are large structures with 6-10 m-deep foundation blocks that will generally scatter and/or completely block shallow high-frequency surface waves. At DCPP these structures include the turbine building and the two containment structures.

2.1 VIBROSEIS DATA FOR SURFACE-WAVE DISPERSION ANALYSES

The best velocity constraints are provided by Vibroseis source data in and around the DCPP foundation area (Figures 2.1-1 and 2.1-2). It was difficult to locate subsets of the

recorded Zland node data in the DCPP foundation area with excellent signal-to-noise since the DCPP foundation area is extremely noisy. However, searching through the entire Zland node database of 16+ million traces, 30,000+ waveforms were found in the DCPP foundation area (within the red polygon in Figure 2.1-2) with sufficient signal-to-noise to calculate Rayleigh-wave dispersion at 93 distinct locations in the DCPP foundation area (Figures 2.1-1 and 2.1-2).

All the 93 distinct Zland receiver group centroid locations have at least 20 Vibroseis source points so that high-quality surface-wave dispersion can be estimated and 15-20 Zland receivers per group distributed over a radius of 100-200 m; the median number of source points in each receiver group is 65 with 28 receiver groups having 100 or more shotpoints of data. As the two receiver groups in Figure 2.1-3 demonstrate the large number of Vibroseis shotpoints provides dense wide-azimuth surface-wave path coverage around each of the centroid positions shown in Figures 2.1-1 and 2.1.2. On Figure 2.1-3, the green squares to the northeast and southwest of the turbine building represent seismic stations ESTA 28 and ESTA 27, respectively. The wide range of source-receiver azimuths and 2-D wide distribution of the receivers in the Zland receiver groups reduces the susceptibility to dispersion estimation biases that are associated with linear receiver arrays when linear arrays are subparallel to strong lateral changes in velocity structure.

Figure 2.1-4 shows the Rayleigh-wave phase dispersion for the northern receiver group in Figure 2.1-3 that is located northeast of seismic station ESTA 28 where many of the source-receiver paths cross southwest of a diabase exposure in Diablo Canyon (Figure 2.1-3). The waveforms from the shot gather in Figure 2.1-4 have short durations with the surface wave arrivals ending prior to 0.4 s consistent with the large minimum phase velocity of > 700 m/s in the slowness-frequency image in Figure 2.1-4. In contrast, the waveforms from paths south of the main DCPP and south of seismic station ESTA 27 (south green square in Figure 2.1-3) in an area with less excavation (Figure 1.3-1) have much longer surface wave arrival durations sometimes exceeding a second consistent with the lower minimum phase velocity of 500 m/s in the slowness frequency image as shown in Figure 2.1-5.

The areas spanned by the 93 receiver groups of Zland nodes and their Zland Vibroseis source-receiver paths are shown in Figure 2.1-6. The corresponding 93 Zland receiver-ground centroid positions are shown in Figure 2.1-7. The 93 additional Zland receiver constraints on Rayleigh-wave fundamental-mode dispersion are combined with seven Seistronix-Sigma receiver group dispersion estimates (Figure 2.1-7) to provide Vs-depth estimates at 100 distinct positions within the DCPP foundation area. There are no source-receiver paths within the areas of the DCPP foundation, where large structures with 6-10 m-deep foundation blocks that will generally scatter and/or completely block shallow high-frequency surface waves (Figure 2.1-6). Direct estimates of Vs-depth are available from downhole Vs traveltimes at borehole DDH-D, which is the northeastern magenta triangle east of the containment structures in Figure 2.1-7 (borehole locations are labeled in Figure 2.1-1, DDH-A-2 [SW], DDH-C [middle], and DDH-D [NE]). Borehole DDH-D is the one downhole site with Vs constraints, of the three downhole sites with shear-wave traveltimes shown in Figure 2.1-1, which fills in an area where no other Vs data are available.

2.2 SURFACE-WAVE DISPERSION VS-DEPTH ESTIMATION

Surface-wave phase dispersion was calculated for all 93 Zland receiver groups and assigned to the positions of the Zland receiver centroids denoted by the yellow circles in

Figure 2.1-7. Additional receiver data from a fixed cable and temporary nodes at seven positions were reprocessed to invert for Vs-depth and Vs-depth uncertainties at the green positions in Figure 2.1-7. The Vibroseis recordings are processed for phase-slowness constraints using the slowness-frequency phase-stacking approach of O'Connell and Turner (2011). The precise timing of the Vibroseis source and the precise (< 0.1 m position uncertainties) surveying of the source and receiver locations provided accurate differential source-receiver distances for slowness-frequency phase stacking analyses using irregular 2-D distributions of 15-21 nodes in addition to linear arrays of geophones. 2-D distributions of variably spaced nodes spanning over 100-200-m-wide areas provided comprehensive 3-D seismic dispersion and waveform sampling large portions of the DCPP foundation area (Figure 2.1-6).

Since the DCPP foundation area typically vibrates at ~1% g due to mechanical power-plant system, particularly the turbines and cooling systems, there is not sufficient signal-to-noise to calculate group-slowness constraints using the interferometric approach of O'Connell and Turner (2011). Instead, synthetic 3-D waveform modeling is used to obtain velocity uncertainty constraints using waveform group arrival times as discussed in Section 3.

As Kausel and Roesset (1981) showed phase-velocity (inverse of phase-slowness) constrains subsurface shear-stiffness structure as a function of depth and thus provides fundamental constraints on Vs-depth needed for site responses analyses. The Monte-Carlo Vs-depth inversion approach of O'Connell and Turner (2011) is used to estimate sets of Vs-depth models consistent with observed Rayleigh phase slowness-frequency. The approach of O'Connell and Turner (2011) is similar to approaches developed during the InterPacific non-invasive shear-wave velocity estimation project (Garofalo et al., 2015) particularly the approaches of Wathelet et al. (2004) and Wathelet (2008) to evaluate large varying classes of Vs-depth structure to estimate the widest range of Vs-depth structures consistent with dispersion constraints. O'Connell and Turner (2011) save up to 63 Vs-depth models investigated during Monte-Carlo simulated annealing to characterize all the classes of Vs-depth models that are consistent with observed dispersion data.

Examples of phase-slowness dispersion-Vs-depth analyses are illustrated in Figures 2.2-1 to 2.2-7 to provide an overview of the variability of dispersion and Vs-depth across the area containing the DCPP and explain the plot sets presented to document the dispersion-Vs-depth analyses for each receiver set and centroid position.

The left plot in Figure 2.2-1 contains the base map used for all dispersion analysis plots with gray-shaded topography (lowest elevations are darkest and highest elevations are lightest) with 10 m contour lines, black outlines of the larger buildings in the DCPP area, the two seismographic station locations that recorded earthquakes as blue squares (ESTA 28 is the north station and ESTA 27 is the south station), and locations of downhole shear-wave traveltime measurements are the magenta triangles (borehole locations are labeled in Figure 2.1-1). The left plot of each receiver group's dispersion-Vs-depth analysis contains all the receivers used in the dispersion analyses as red diamonds with yellow lines showing all the Vibroseis-source-receiver paths used to calculate phase dispersion using the differential source-receiver distances among the receivers. The receiver-centroid (thick black circle in the left plot of Figure 2.2-1) represents the ground position of the estimated phase-dispersion. The top center plot in Figure 2.2-1 shows the phase-slowness frequency image with dark purple

indicating areas of maximum relative amplitude and deep blue indicating the lowest areas of relative amplitude in the slowness-frequency phase stack. Magenta circles show the picked phase slownesses in the top center slowness-frequency image and the phase-velocity plot at the upper right. Phase slowness uncertainties are the black circles connected with black lines in the top center plot and are shown as uncertainty bars in the phase-velocity plot to the upper right. The calculated phase velocities for the number of models found that are consistent with the phase-velocity picks are shown as the group of thin black curves in the phase-velocity plot at the upper right. In Figure 2.2-1 there are 28 Vs-depth models identified in the Monte-Carlo simulated annealing search that produce the range of Vs-depth functions shown in the Vs-depth plot at the lower right with black lines (the magenta curve is the natural logarithm mean of the 28 Vs-depth models). The bottom center plot shown relative phase-velocity sensitivity as a function of depth for four frequencies in the range of picked phase-velocities along with the natural logarithm standard deviation magenta curve) of the Vs-depth models (shown in the Vs-depth plot at the lower right). The phase-sensitivity depth kernels show that the high-frequency portions of the phase dispersion strongly constrains Vs in the top 20 m with the variation of intermediate and lowest frequency dispersion constraining Vs to > 100 m depth (Figure 2.2-1).

Figure 2.2-1 illustrates typical Vs-depth located away from the coast in the DCPP excavated area that encompasses the DCPP turbine building and containment structures. Significantly lower shallow Vs on the order of 200-300 m/s is only found in unexcavated areas around DCPP near the sea cliffs (Figures 2.2-2 and 2.2-3), in fluvial deposits within Diablo Canyon, and in regions to the south near the coast (Figure 2.2-4). The low shallow Vs in unexcavated areas reduces the maximum depth of Vs resolution (Figures 2.2-2, 2.2-3, and 2.2-4) relative to (usually paved) excavated areas (Figures 2.2-1, 2.2-5, 2.2-6, and 2.2-7) because low shallow Vs reduces the maximum wavelength for the fixed lowest frequency of dispersion constraints of 8 Hz associated with the low-frequency end of the Vibroseis sweep.

The complete set of all 100 dispersion analyses are provided in Appendix A in the same format as Figure 2.2-1. These 100 Vs-depth constraints along with Vs traveltime data from the three DCPP boreholes provide the basis for the first update of the PR-16 3-D Vs model. Prior to describing the process and results of the first 3-D Vs model update Vs-depth uncertainties and spatial variability are discussed in the next section to provide a context for the approach used to update the 3-D Vs model.

2.3 SURFACE-WAVE DISPERSION VS-DEPTH UNCERTAINTIES AND VARIABILITY

Vs-depth uncertainties are essentially entirely epistemic since aleatory variability of Vs due to Vs changes with time are relatively small. Vs epistemic uncertainties are the result of finite Vs spatial resolution both laterally and vertically. Multiple surface-wave dispersion estimates of Vs-depth located close to each other with separation distances comparable to the horizontal grid spacing of the 3-D Vs model provide data to estimate Vs-depth epistemic uncertainties as a function of position in the 3-D model and as functions of other attributes, particularly excavation depth. Two approaches are used to evaluate Vs-depth epistemic uncertainties associated with the surface-wave dispersion Vs-depth estimates. The first approach assembles as many as available Vs-depth estimates within 25 m of each other to calculate *ln*-mean Vs-depth and Vs-depth *ln*(σ); there are 26 groups where the maximum separation distance between Vs-depth sites is less than 20 m and 7 sites where the maximum separation distance between Vs-depth sites is less than 25 m. The second approach uses

combinations of the three closest Vs-depth estimates to minimize site separation distances between Vs-depth estimates to calculate minimum bounds on at-site Vs-depth epistemic uncertainties.

Vs-depth uncertainties and spatial variability are evaluated by combining nearby groups of Vs-depth estimates. To evaluate variability on scales of 25 m or less, 33 groups of three or more Vs-depth estimates located within 25 m of each other (see Appendix B) are combined to calculate *ln*-mean Vs-depth and Vs-depth *ln*(σ) separated into groups of sites with at least 1 m of excavation and sites with less than 1 m of excavation (Figure 2.3-1) and sites located inland beneath the DCPP foundation relative to sites located closer to the coast (Figure 2.3-2). While there is some reduction of Vs variability at sites with 1 m of excavation (Figure 2.3-1), there is nearly a factor of two reduction of Vs variability below 10 m depth at inland sites relative to coastal sites (Figure 2.3-2). This indicates that the primary factors influencing Vs variability at depth below the DCPP foundation are distance from the diabase intrusives to the east of the DCPP foundation since the influence of weathering is limited to the first 10-20 m of depth. Vs at 100 m depth of 1300 m/s is 47% larger at inland sites than coastal sites, while mean reduction of Vs *ln*(σ) in the 10-60 m depth range is 1.71 times lower than at coastal sites (Figure 2.3-2). Mean Vs *ln*(σ) of the inland sites in the 10-50 m depth range is 0.10 which is comparable to the mean Vs *ln*(σ) of 0.11 observed between the two ISFSI borehole suspension log Vs estimates in the 5-46 m depth range (Figure 1.2-1 and associated text); the ISFSI boreholes are separated by 60 m. Variability is highest in the weathering zone in the shallowest 10 m but is lower both inland and in excavated areas (Figures 2.3-1 and 2.3-2).

Groups of three Zland Vs-depth estimates located closest to each other are used to evaluate Vs variability for smaller site separations (see Appendix C) than used in Figures 2.3-1 and 2.3-2. Most of the 71 groups of three Vs-depth estimates are within 1.5 3-D grid cell dimensions (22.86 m) of one another (Figure 2.3-3). Consequently, *ln*-mean and *ln*(σ) estimated from these groups of three Vs-depth estimates characterize Vs variability on the scale of horizontal resolution of the 3-D Vs model. While there is some reduction of Vs variability at sites with 1 m of excavation (Figure 2.3-4), there is a factor of 1.80 reduction of Vs *ln*(σ) between 10 m and 60 m depth at inland sites relative to coastal sites (Figure 2.3-5).

The sets of *ln*-mean Vs-depth of the closest 3 Zland estimates of Vs-depth are used to update the 3-D Vs model as presented in the next section. Consequently, the most appropriate estimates of the lower bounds on Vs-depth epistemic uncertainties for the DCPP foundation are obtained from Figure 2.3-5. Figure 2.3-5 shows that minimum at-site epistemic Vs-depth uncertainties within the DCPP foundation are in terms of *ln*(σ) are 0.15 for depths less than 10 m, 0.11 for 10-100 m depths, and increasing from 0.11 at 100 m to 0.16 at 120 m.

2.4 3-D VS UPDATES

The 3-D velocity model is updated in two steps. First the additional Vs-depth profiles estimated in Section 2.3 and Vs-depth profiles that are consistent with the Vs traveltime data from the three boreholes within traveltime data picking uncertainties are used to calculate adjustments to the PR-16 3-D Vs model. A second set of 3-D velocity adjustments is calculated in a small area of the model where many azimuths of intersecting wave paths make it feasible to invert waveform group traveltime delays calculated with waveform cross-correlation analyses using linear 2-D tomographic backprojection of group slowness delays. This second 3-D model adjustment presented in Section 3.3.5 is used to verify that group delays calculated from

waveform cross correlation analyses provide robust quantitative estimates of Vs uncertainties over the depth range of 0-50 m as discussed in Section 3.3.4.

2.4.1 3-D Vs Model Update Using Dispersion and Borehole Constraints on Vs-Depth

Many of the 93 Zland estimates of Vs-depth are located relatively close to one another (Figure 2.1-7) with 26 sets of three to nine Zland centroids located within 20 m of each other and seven sets of three to four Zland centroids located with 25 m of each other. The horizontal cell size of the original 3-D grid is 15.24 m (50 ft) and this 15.24 m horizontal cell size is used to update the 3-D Vs model. 71 sets of the three Zland centroids are located within a 3-36 m maximum distance from their three-group centroid with a median maximum distance of 14 m and 93% of the maximum distances less than 1.5 grid cell dimensions (22.86 m) as shown in Figure 2.3-3. From the 71 sets of Zland centroids with Vs-depth profiles derived from three *ln*-averages of Vs-depth and seven sets of Seistronix-Sigma centroids with Vs-depth profiles, there are 78 Vs-depth centroid sites. These 78 Vs-depth centroid positions are located in 62 unique 3-D 15.24 m cell locations; there are 13 cells with two or three Vs-depth profiles within the extent of the horizontal cell. Consequently, to ensure a single Vs-depth profile is assigned to each of the 62 3-D Vs cells with Zland and/or Seistronix-Sigma dispersion constraints on Vs-depth, 10 cells have *ln*-average Vs-depth calculated using two sets of Vs-depth profiles and three cells have *ln*-average Vs-depth calculated using three sets of Vs-depth profiles. Single sets of Vs-depth profiles are used for the remaining 49 3-D grid cells. There are also three borehole Vs-depth profiles derived from Vs-downhole traveltime data at three additional unique 3-D Vs cells yielding a total of 65 separate 3-D Vs cells with Vs-depth constraints (interior yellow and red boxes in Figure 2.4-1). The red boxes in Figure 2.4-1 show Vs-depth constraint cells where the depth of excavation is greater than 3 m.

The 62 dispersion-based Vs-depth profiles are converted to ratios of the updated Vs-depth profile to the Vs-depth profile from the PR-16 (Fugro, 2014a) 3-D Vs model to assemble scale factors to adjust the previous 3-D Vs model to be consistent with the updated Vs-depth profiles. The variability of scale-factors and Vs as a function of depth are shown at the top of Figure 2.4-2. In this figure, the right plots show the Vs-depth profiles of all positions at the top and the 9 profiles located at sites with 3+m of excavation typical of the DCPP foundation at the bottom. The left plots show corresponding Vs-depth scale factors to convert the original Vs model to be consistent with the Vs-depth constraints. There are nine Vs-depth profiles located in areas of 3 or more meters of excavation prior to construction that are generally located toward the east side of the DCPP facilities (red squares in Figure 2.4-1). These nine Vs-depth profiles at excavated positions exhibit less variability of scale factors and Vs-depth in the 0-50 meter depth range and generally smoother Vs variations with depth as shown in the bottom set of plots in Figure 2.4-2.

A perimeter of cells are assigned scale factors of 1.0 to ensure that interpolated Vs scale factors smoothly taper to 1.0 away from the region with Vs-depth profile constraints; these perimeter constraints surround the 65 Vs-depth profiles in Figure 2.4-1 (perimeter constraints to the west and just west of the west margin of Figure 2.4-1). Vs varies more systematically with depth than elevation. Consequently, inverse-distance gridding is used at a 0.52 m depth interval to interpolate Vs scale factors such that the 65 Vs-depth profiles are enforced in cells as knots in the interpolation. The inverse-distance interpolation approach ensures that Vs adjustments vary smoothly between knots.

All updated 3-D Vs model plots are provided in Section 3.0 after a second set of Vs adjustments based on waveform analyses. Consequently, the 3-D Vs model updated based solely on dispersion and borehole Vs-depth constraints is not plotted here because it is simply an intermediate model iteration, not the final updated 3-D Vs model.

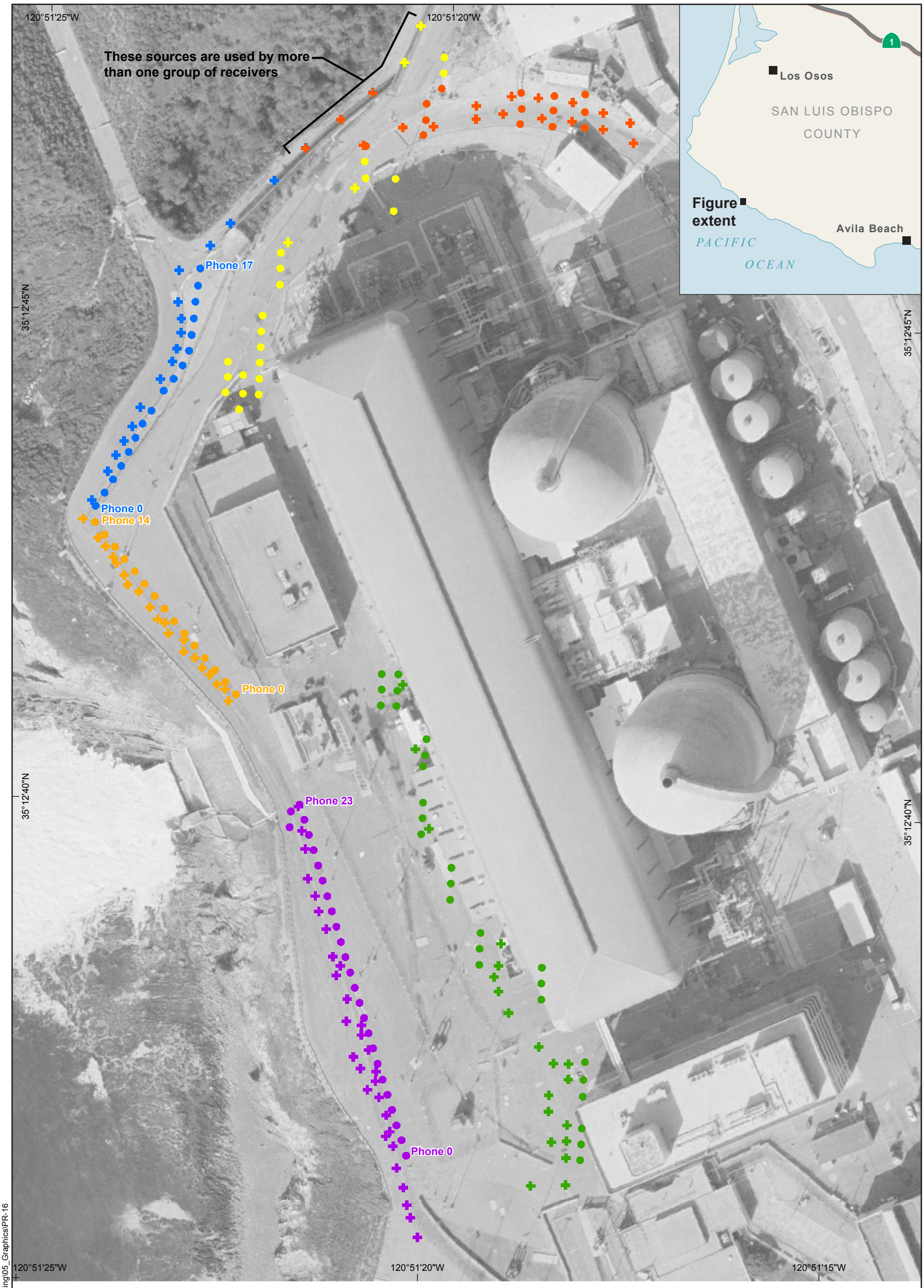

Imagery from TetraTech (2010).

EXPLANATION

- Sigma northeast PA
- Sigma northwest PA
- Sigma southwest PA
- Seistronix cable 3 central east
- Seistronix cable 3 northeast
- Seistronix cable 3 southeast
- Source
- Receiver

N

0 50 100 ft.

0 20 40 m

Map projection and scale: NAD 83 State Plane CA Zone V, 1:1,200

DCPP PR-16 Source-Receiver Pairs

3D DCPP VS UPDATE REPORT

Pacific Gas and Electric Company

Figure **2.0-1**

Revision 0

K:\Projects\79_225400_PGE_WE2_Onshore_2011_Ph1_Processing\05_Graphics\PR-16

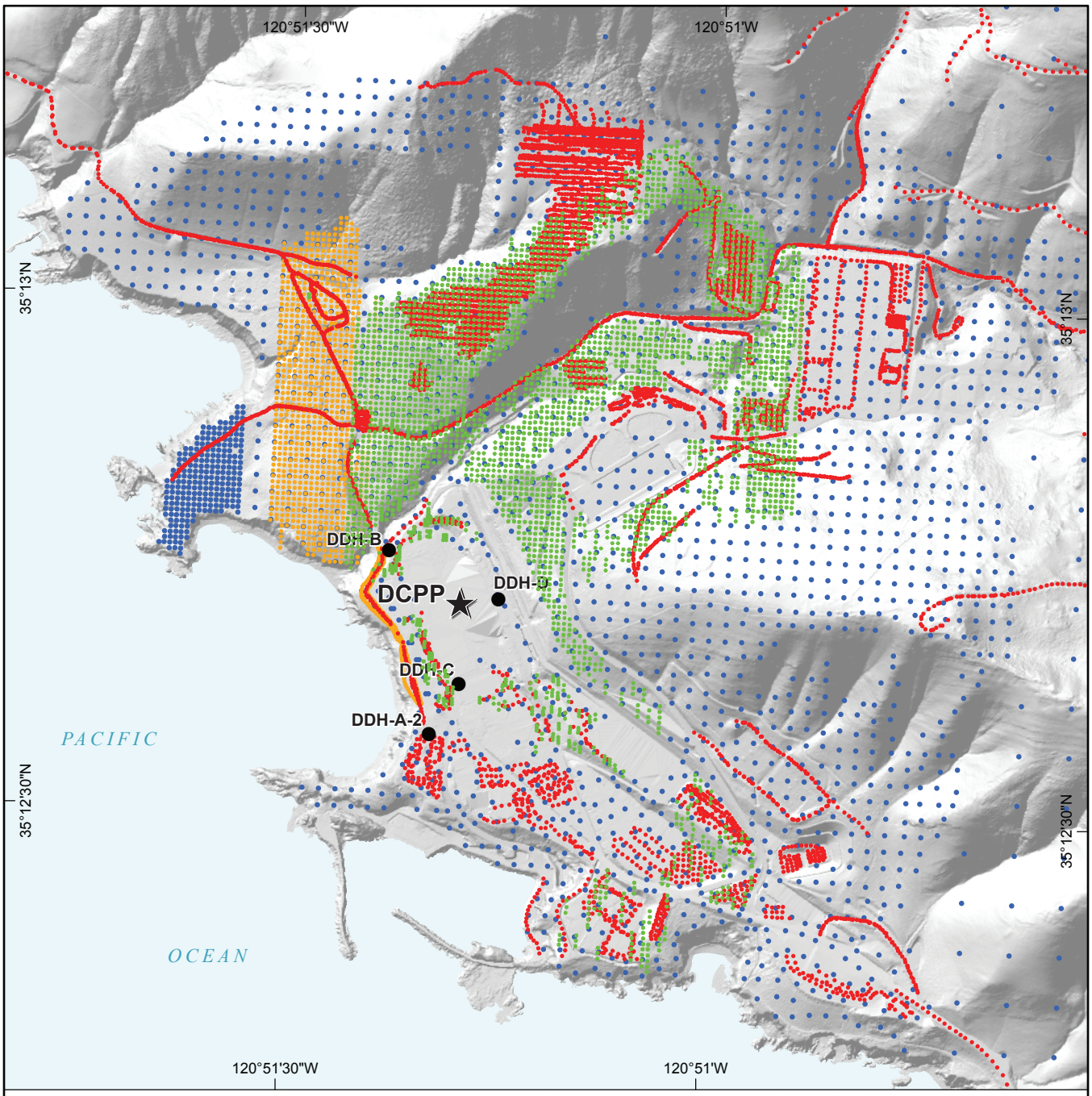

EXPLANATION

2012 Phase 1 Data

- Zland receiver locations
- Sigma receiver locations
- Seistronix receiver locations
- Vibroseis source locations
- **DDH-C** ● Borehole location of the 1978 investigations

N

0 0.25 0.5 mi

0 0.25 0.5 km

Map projection and scale: NAD 83 State Plane CA Zone V, 1:11,000

2012 Phase 1 DCPP 3D Survey Source and Receiver Locations Detail

DCPP FOUNDATION VELOCITY REPORT

Pacific Gas and Electric Company

Figure **2.1-1**

K:\Projects\79_225400_PGE_WE2_Onshore_2011_Ph1_Processing\05_Graphics\PR-16

DCPP FOUNDATION AREA ZLAND NODES (BLUE CIRCLES) AND NODE GROUP CENTROIDS (ORANGE CIRCLES) (ZLAND NODES WERE USED INSIDE THE RED POLYGON AND VIBROSEIS SOURCES WHERE USED WITH THE YELLOW POLYGON)

Update of the 3−D Velocity Model for the DCPP Foundation Area
San Luis Obispo, California

FIGURE 2.1−2

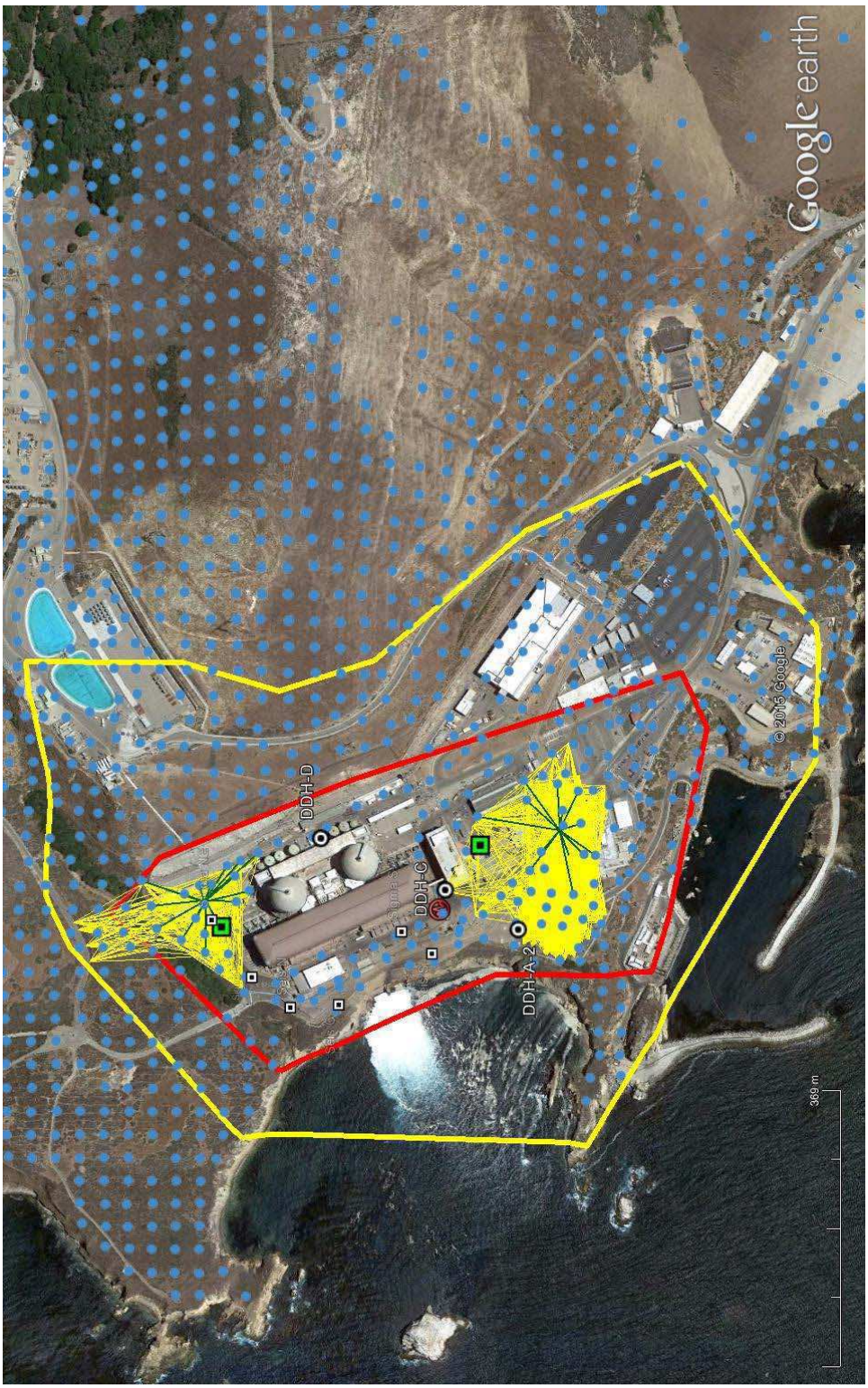

SOURCE−RECEIVER PATHS (YELLOW LINES) FOR TWO ZLAND NODE GROUPS NEAR SEISMIC STATIONS (GREEN CIRCLES) (BLUE LINES EXTEND FROM THE ZLAND NODE GROUP CENTROIDS TO THE NODES IN THE GROUP)

Update of the 3−D Velocity Model for the DCPP Foundation Area
San Luis Obispo, California

FIGURE 2.1−3

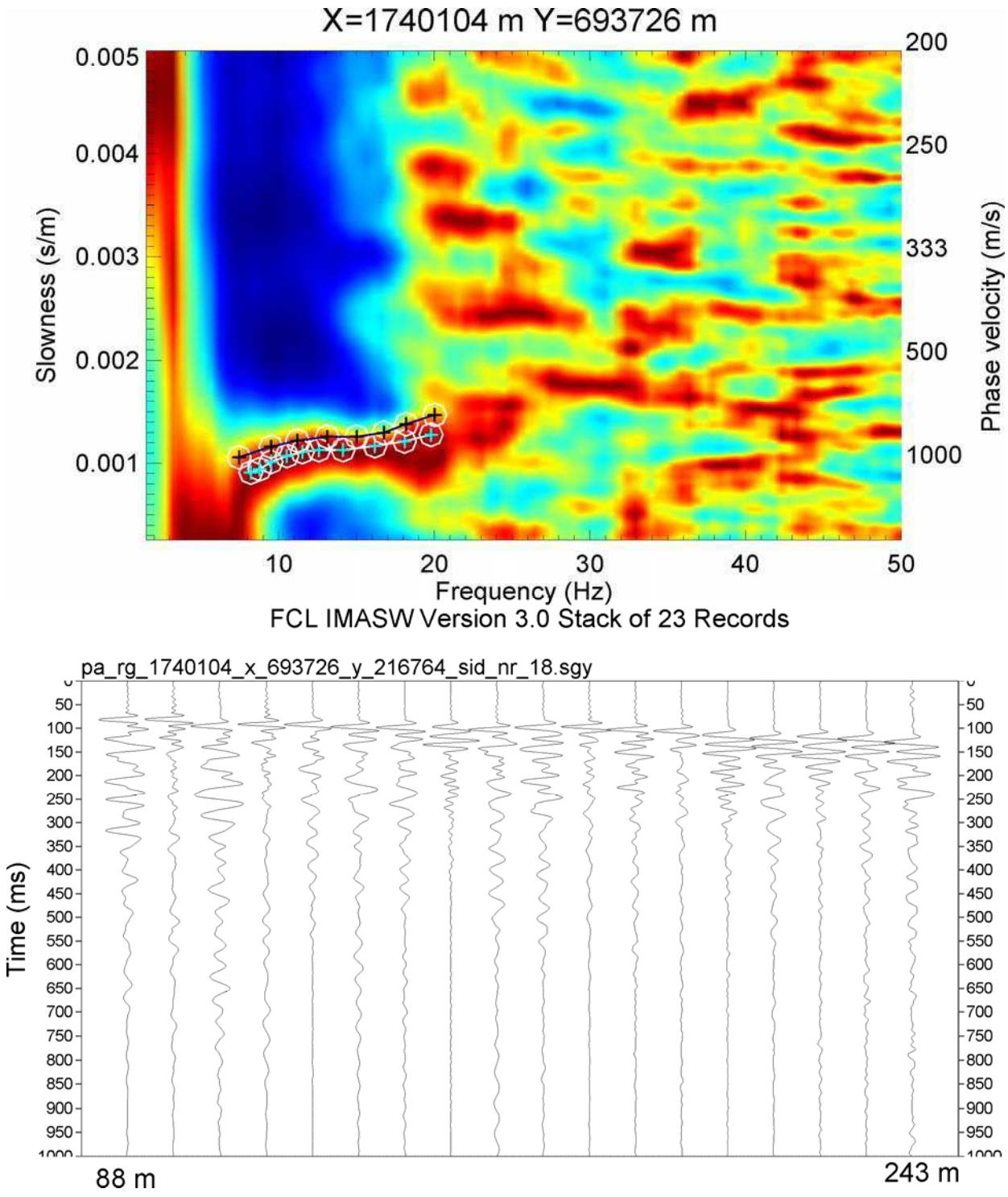

DISPERSION AND WAVEFORMS FROM THE NORTH RECEIVER GROUP IN FIGURE 2.1−3 (DISPERSION PICKS ARE BLUE PLUSES WITH PICKING UNCERTAINTIES AS BLACK PLUSES)

Update of the 3−D Velocity Model for the DCPP Foundation Area
San Luis Obispo, California

FIGURE 2.1−4

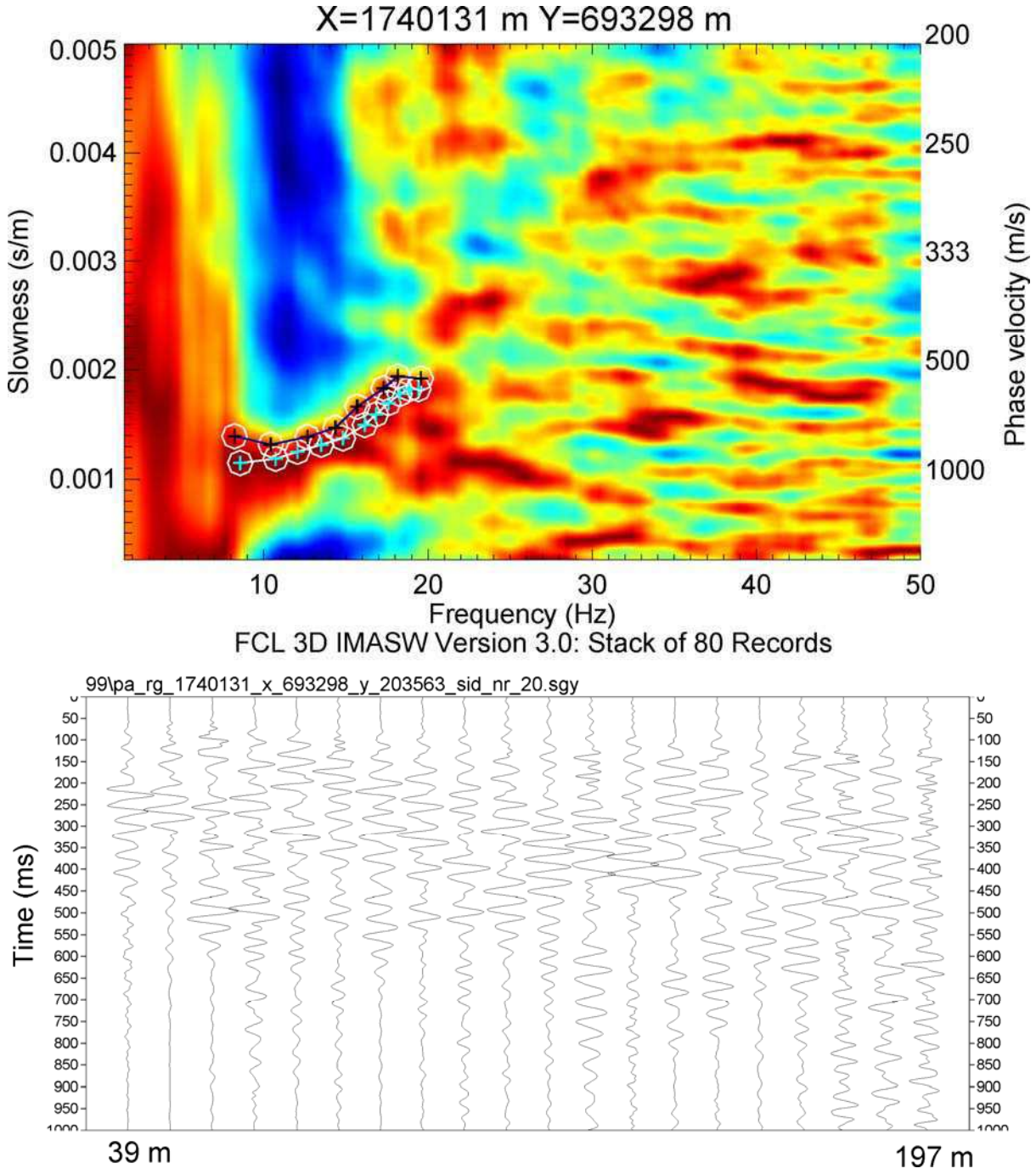

DISPERSION AND WAVEFORMS FROM THE SOUTH RECEIVER GROUP IN FIGURE 2.1−3 (DISPERSION PICKS ARE BLUE PLUSES WITH PICKING UNCERTAINTIES AS BLACK PLUSES)

Update of the 3−D Velocity Model for the DCPP Foundation Area
San Luis Obispo, California

FIGURE 2.1−5

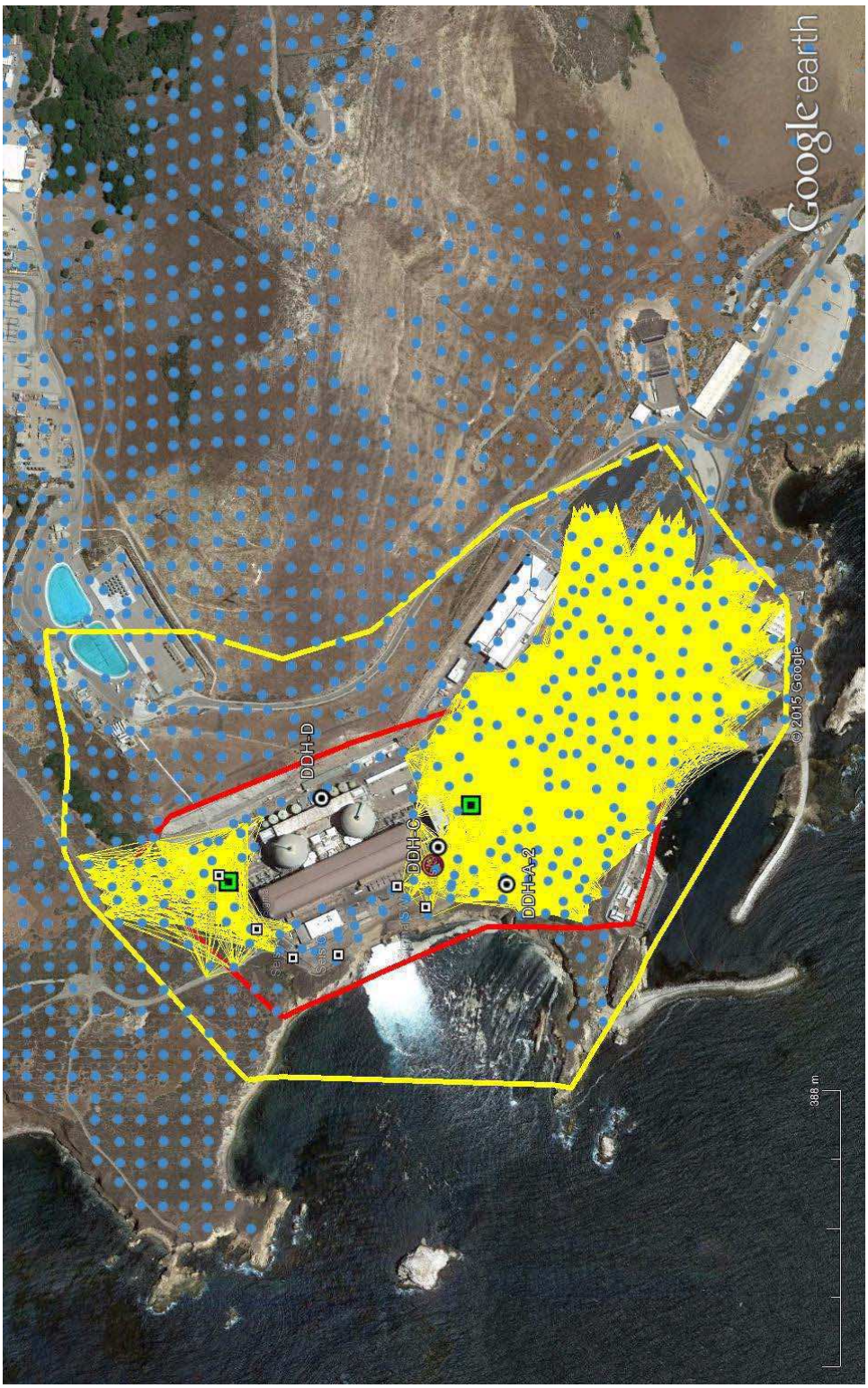

ALL 93 ZLAND RECEIVER GROUP SOURCE−RECEIVER PATHS (YELLOW LINES)
(BLUE CIRCLES SHOW LOCATIONS OF INDIVIDUAL ZLAND NODES)
Update of the 3−D Velocity Model for the DCPP Foundation Area
San Luis Obispo, California

FIGURE 2.1−6

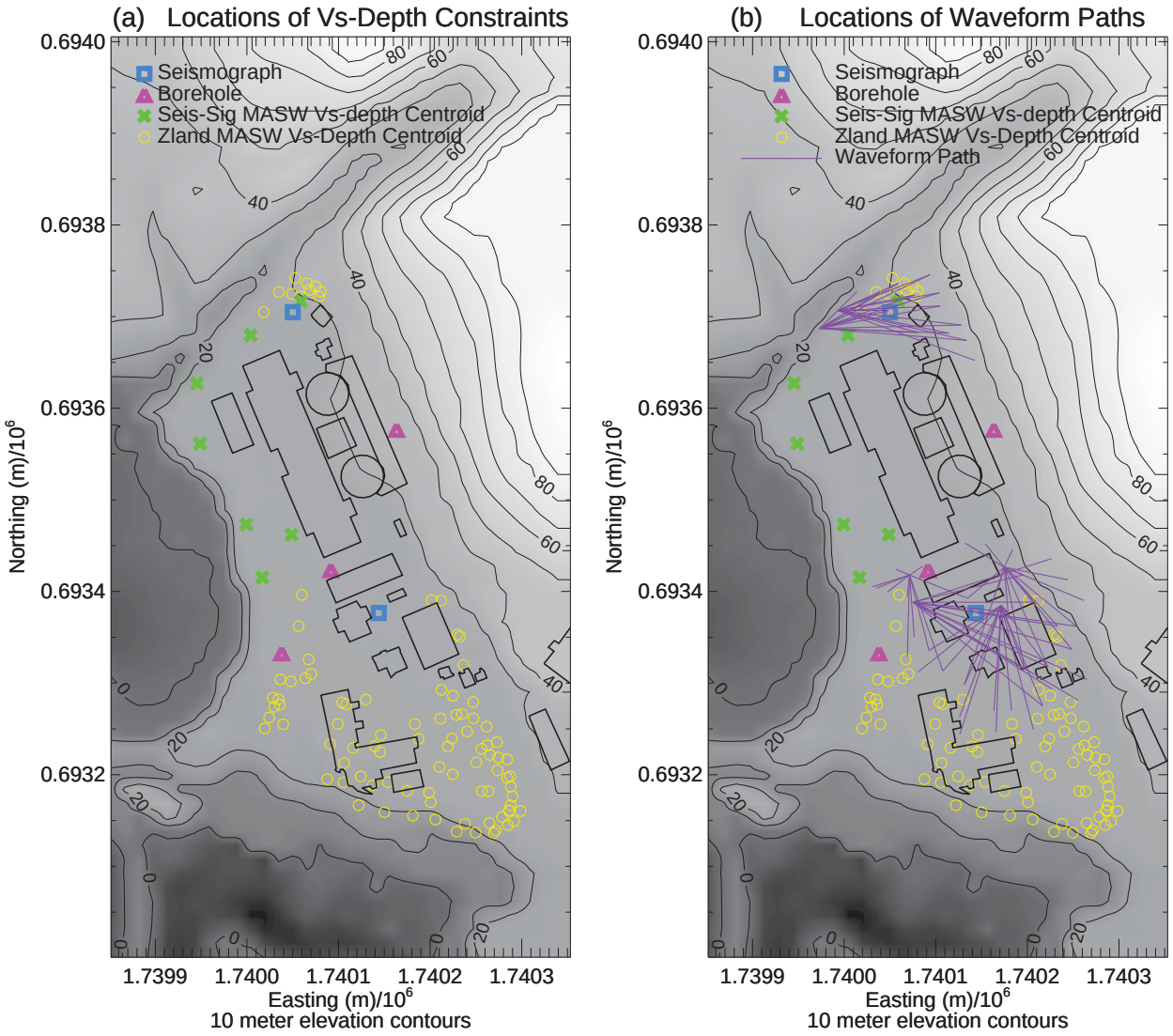

DISPERSION AND WAVEFORM PATH ZLAND−RECEIVER−GROUP VS CONSTRAINT POSITIONS (CENTROIDS: ZLAND−YELLOW CIRCLES, SEISTRONIX−SIGMA−GREEN CROSSES. PURPLE LINES ARE WAVEFORM SOURCE−RECEIVER PATHS USED FOR WAVEFORM MODELING)

Update of the 3−D Velocity Model for the DCPP Foundation Area
San Luis Obispo, California

FIGURE 2.1−7

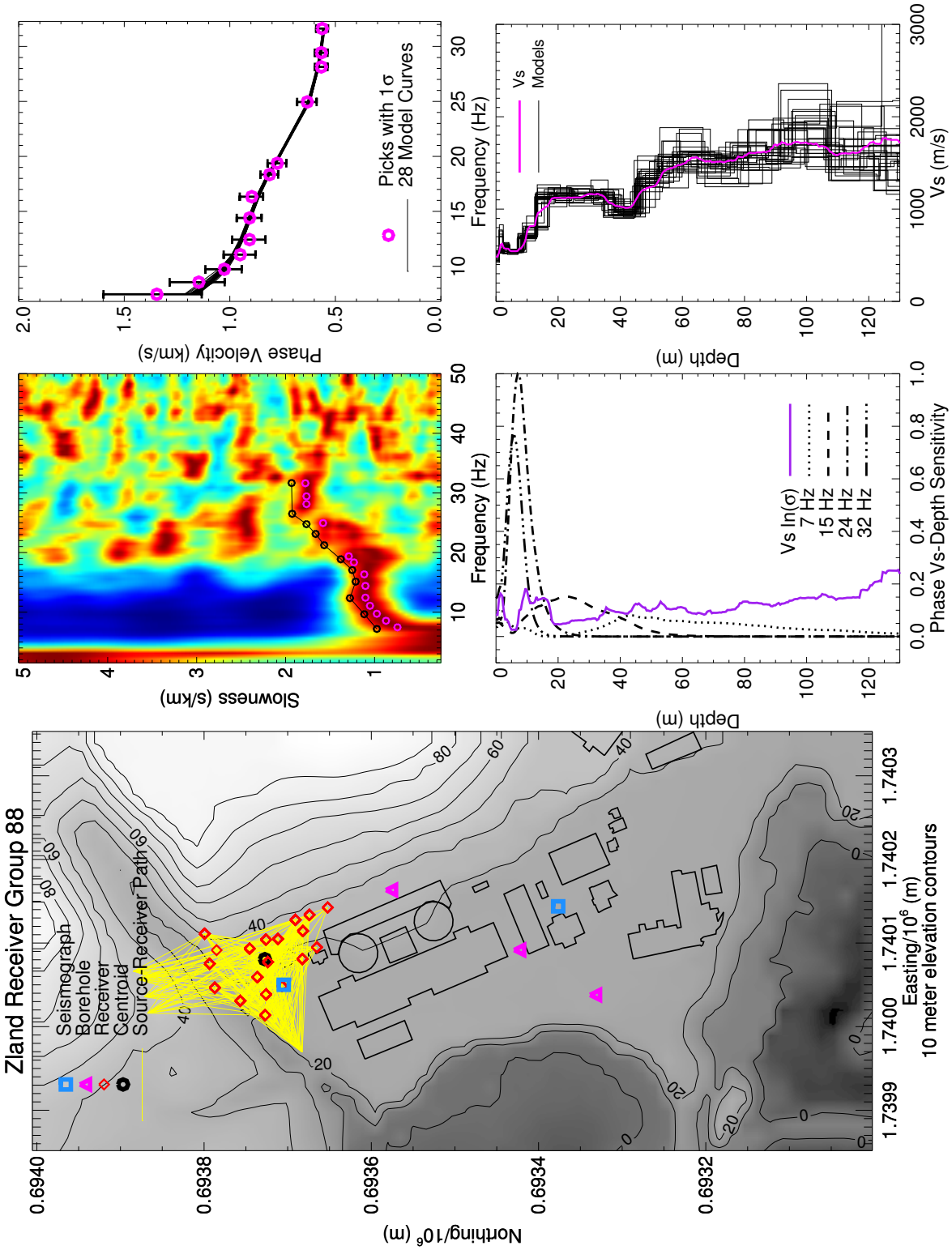

ZLAND RECEIVER GROUP 88 DISPERSION AND VS−DEPTH ANALYSIS
Update of the 3−D Velocity Model for the DCPP Foundation Area
San Luis Obispo, California

FIGURE 2.2−1

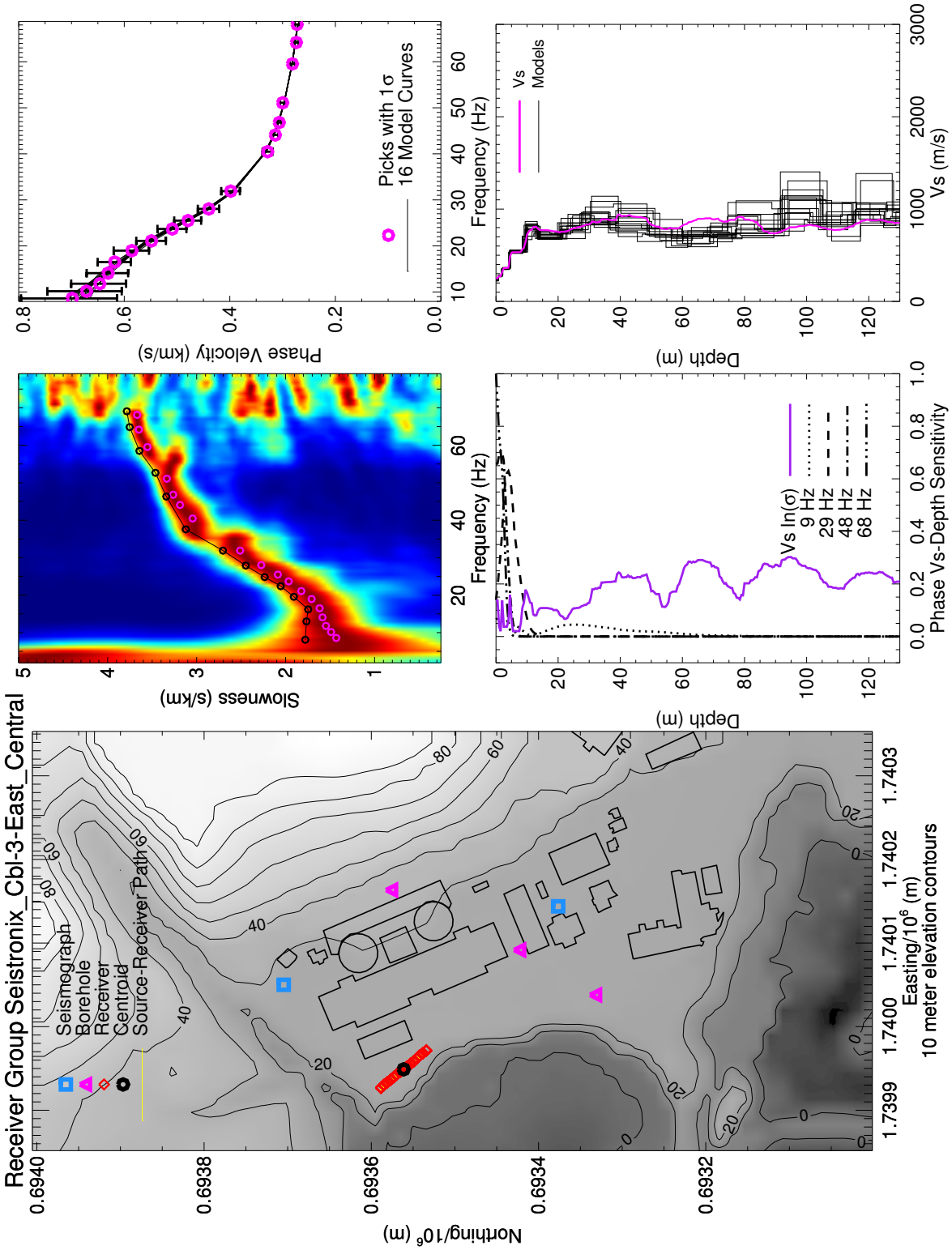

RECEIVER GROUP SEISTORNIX−CBL−3−EAST DISPERSION AND VS−DEPTH ANALYSIS
Update of the 3−D Velocity Model for the DCPP Foundation Area
San Luis Obispo, California

FIGURE 2.2−2

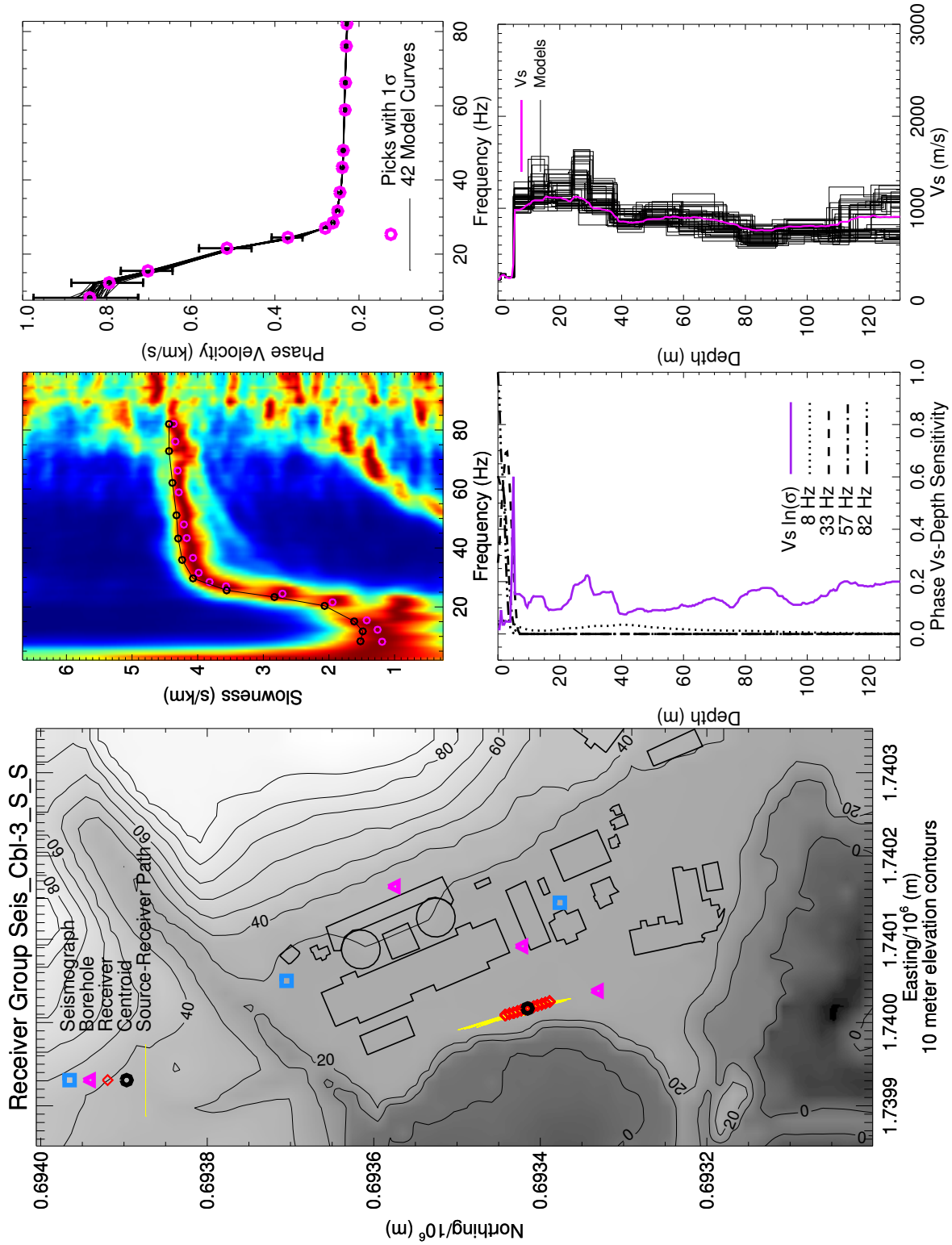

RECEIVER GROUP SEIS−CBL−3−S−S DISPERSION AND VS−DEPTH ANALYSIS
Update of the 3−D Velocity Model for the DCPP Foundation Area
San Luis Obispo, California

FIGURE 2.2−3

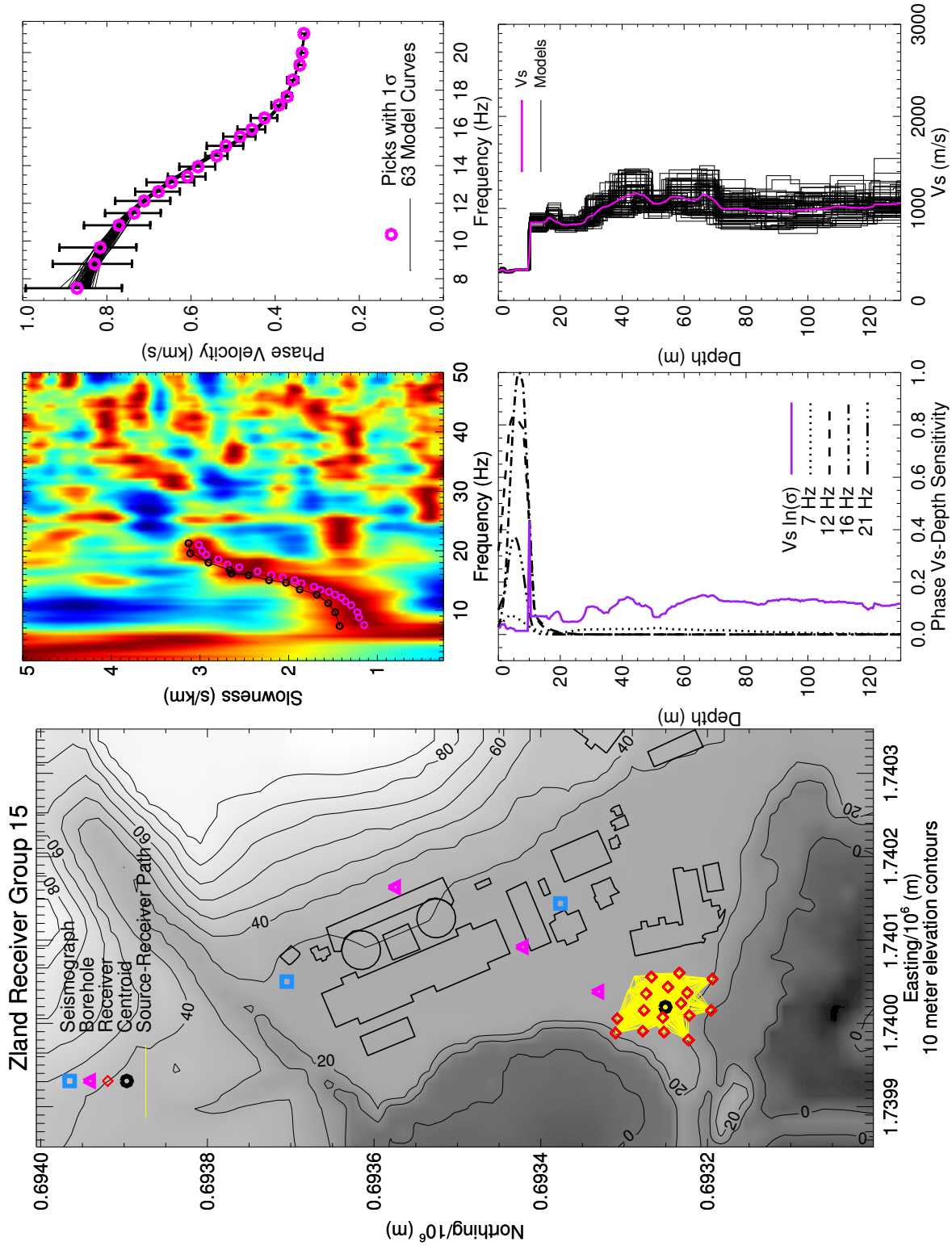

ZLAND RECEIVER GROUP 15 DISPERSION AND VS−DEPTH ANALYSIS
Update of the 3−D Velocity Model for the DCPP Foundation Area
San Luis Obispo, California

FIGURE 2.2−4

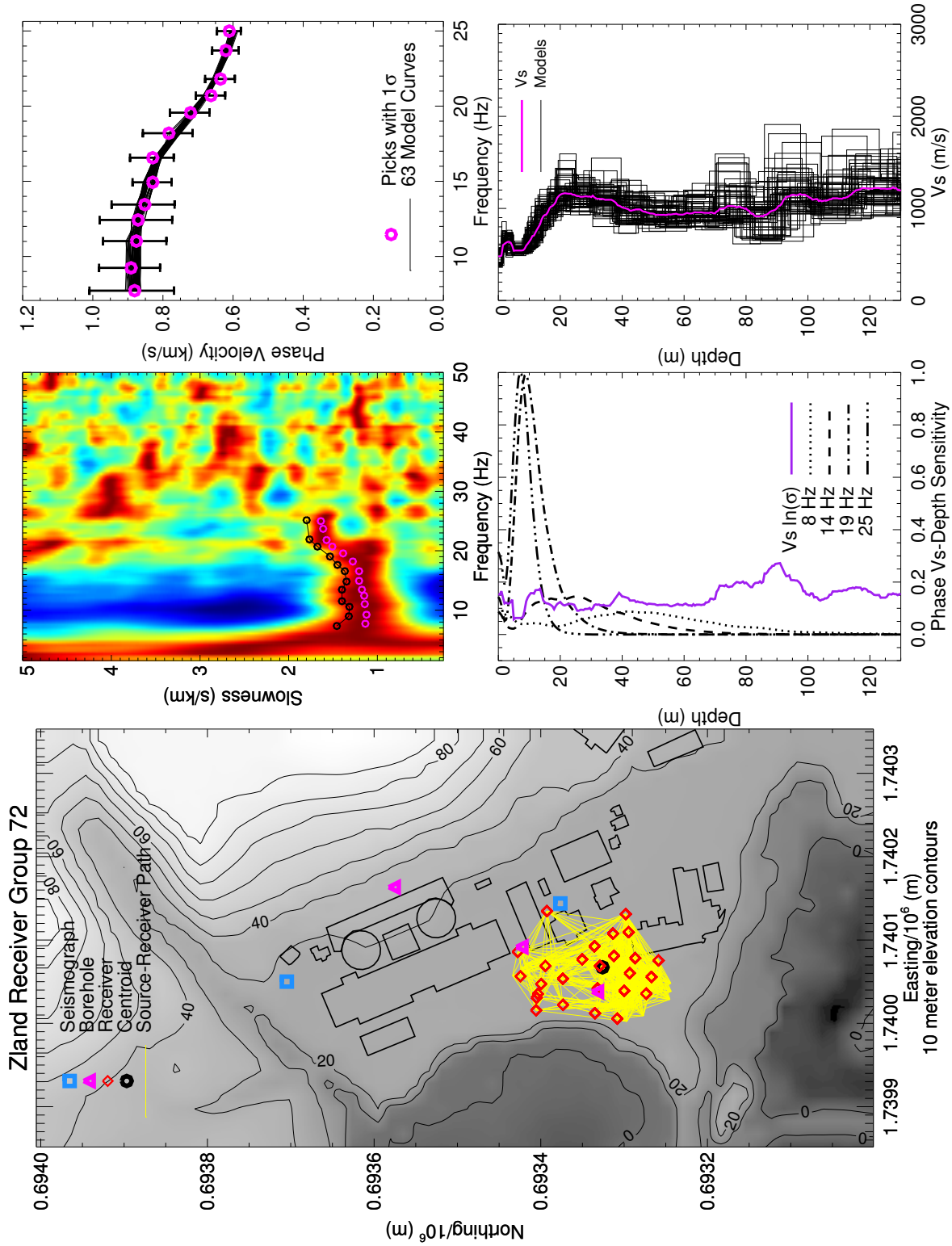

ZLAND RECEIVER GROUP 72 DISPERSION AND VS−DEPTH ANALYSIS
Update of the 3−D Velocity Model for the DCPP Foundation Area
San Luis Obispo, California

FIGURE 2.2−5

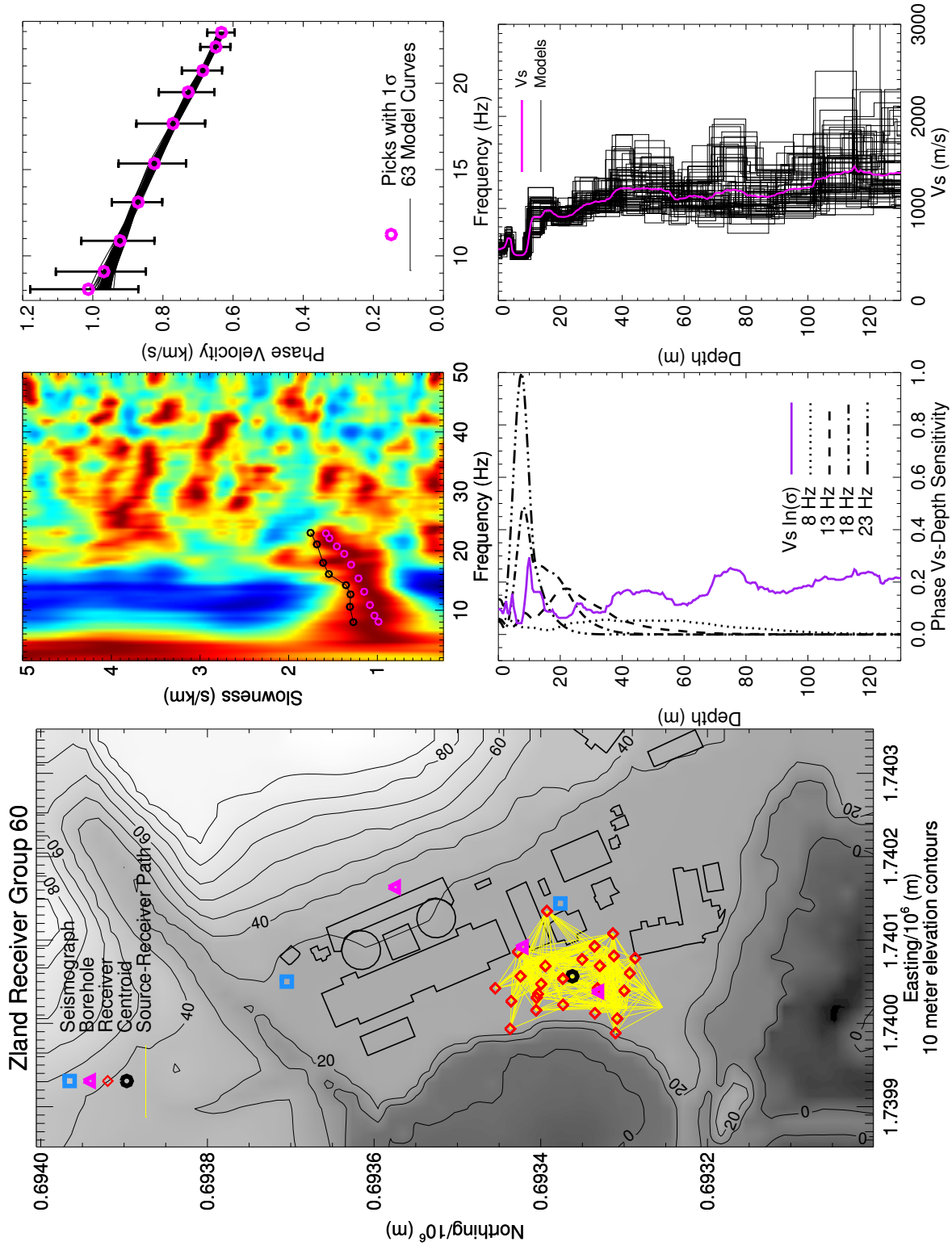

ZLAND RECEIVER GROUP 60 DISPERSION AND VS−DEPTH ANALYSIS
Update of the 3−D Velocity Model for the DCPP Foundation Area
San Luis Obispo, California

FIGURE 2.2−6

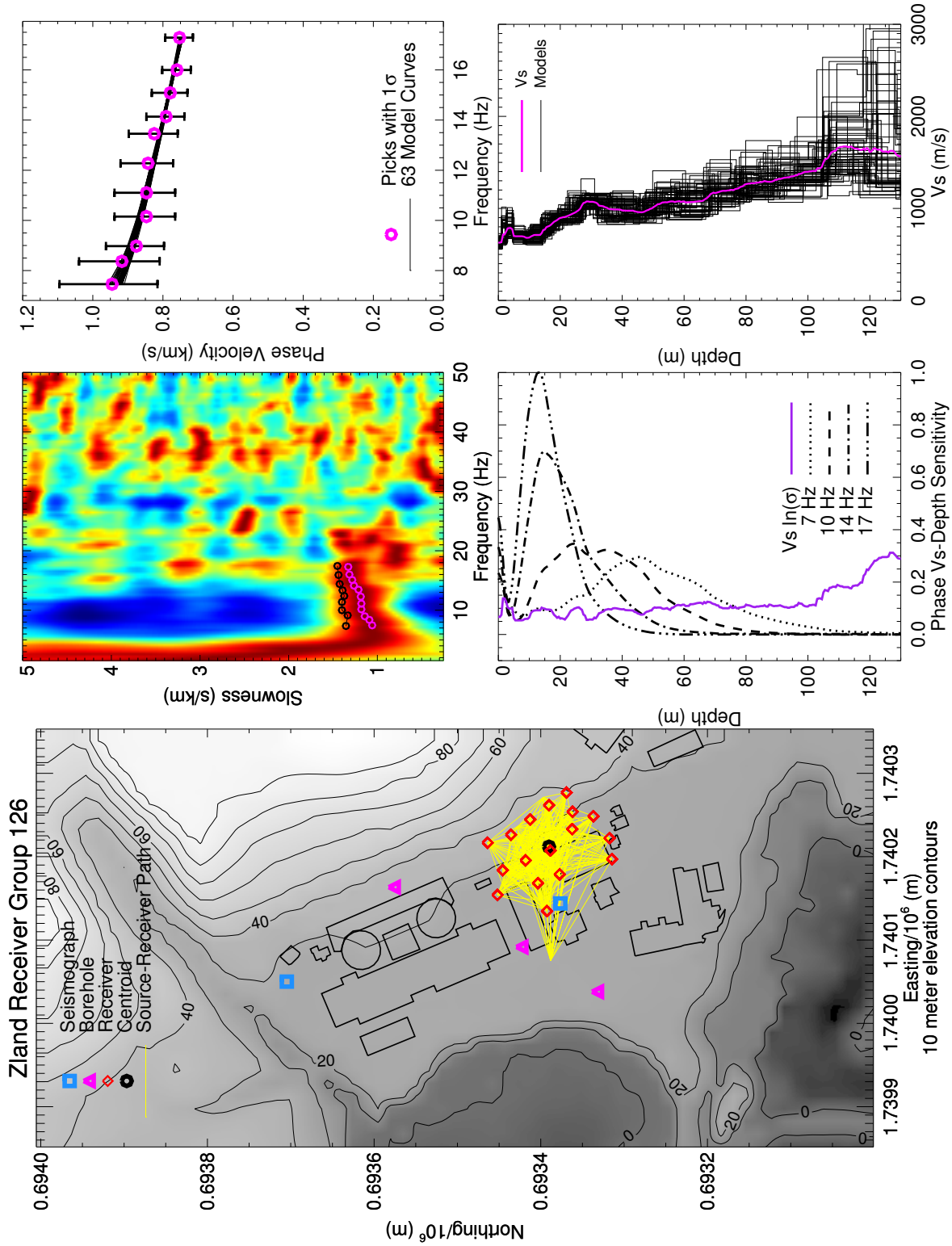

ZLAND RECEIVER GROUP 126 DISPERSION AND VS−DEPTH ANALYSIS
Update of the 3−D Velocity Model for the DCPP Foundation Area
San Luis Obispo, California

FIGURE 2.2−7

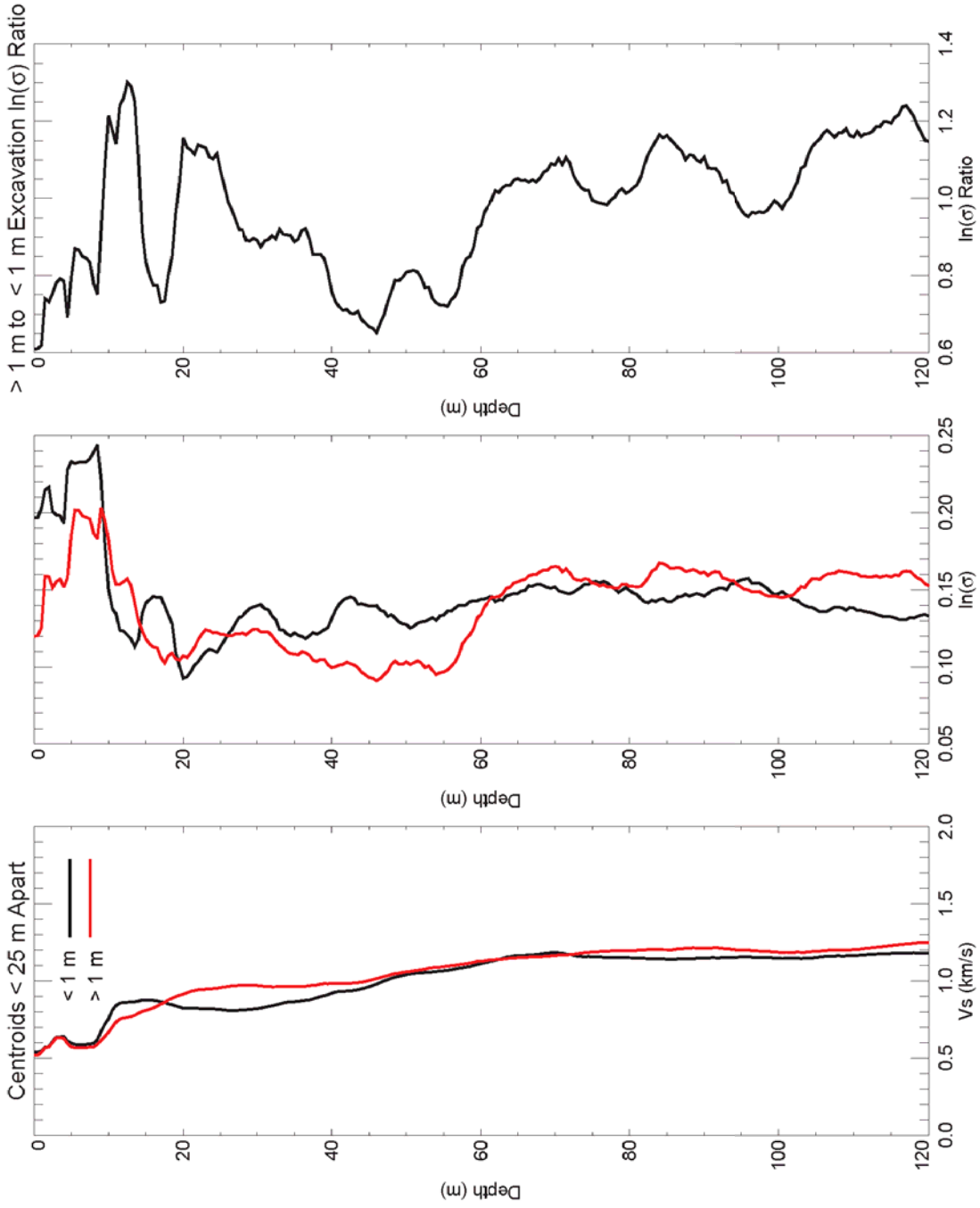

COMBINED ZLAND GROUPS < 25 M SEPARATION AS A FUNCTION OF EXCAVATION (LN−MEAN VS, LN(S), AND RATIO OF LN(S) OF EXCAVATED TO NON−EXCAVATED SITES)

Update of the 3−D Velocity Model for the DCPP Foundation Area
San Luis Obispo, California

FIGURE 2.3−1

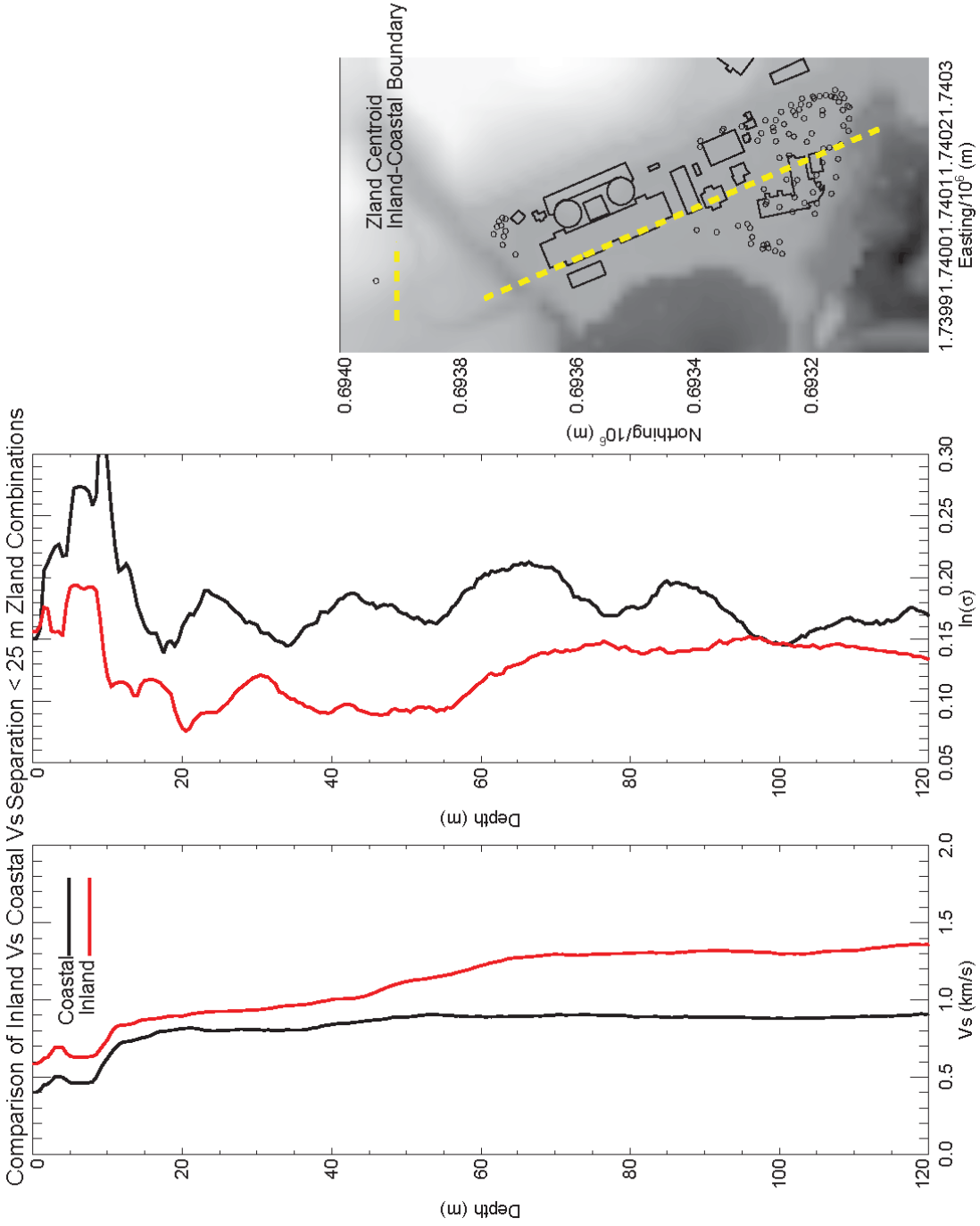

COMBINED ZLAND GROUPS < 25 M SEPARATION SORTED INTO INLAND AND COAST SITES (LN−MEAN VS AND LN(S) WITH THE MAP SHOWING THE POSITION OF THE BOUNDARY BETWEEN INLAND AND COASTAL SITES)

Update of the 3−D Velocity Model for the DCPP Foundation Area
San Luis Obispo, California

FIGURE 2.3−2

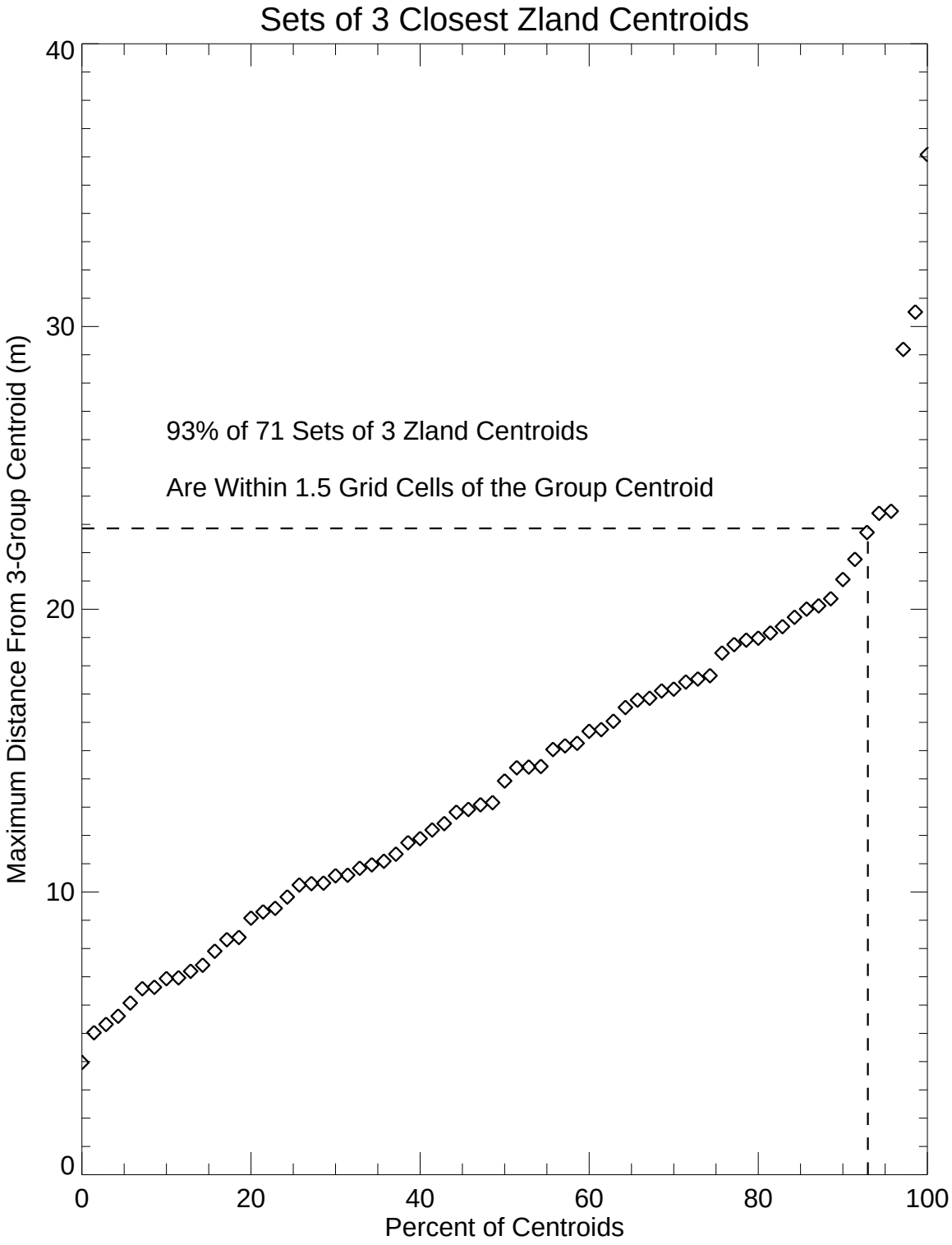

MAXIMUM SEPARATION DISTANCES FOR SETS OF THREE CLOSEST ZLAND VS−DEPTH SITES
Update of the 3−D Velocity Model for the DCPP Foundation Area
San Luis Obispo, California

FIGURE 2.3−3

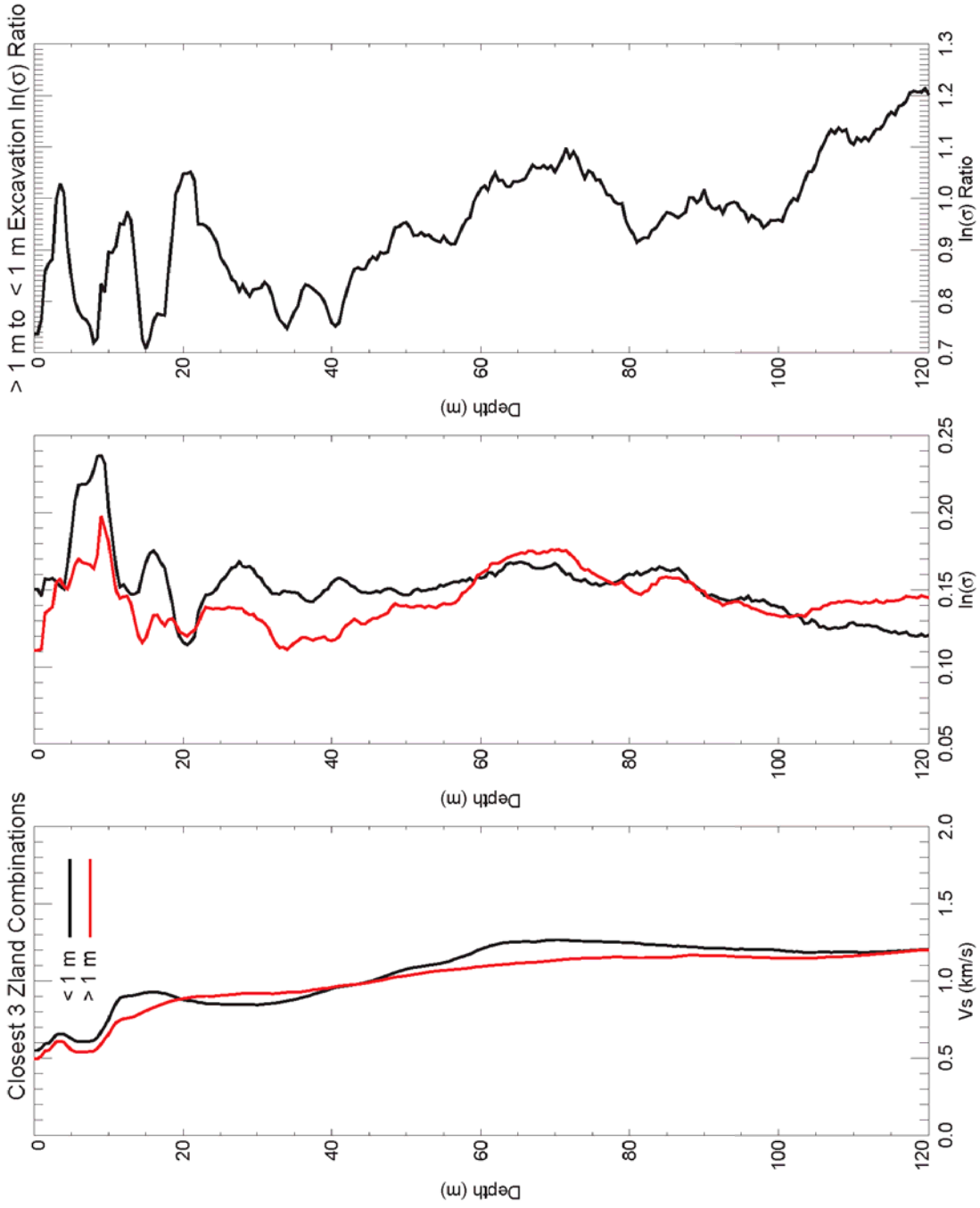

CLOSEST 3 ZLAND COMBINATIONS AS A FUNCTION OF EXCAVATION (LN−MEAN VS, LN(S), AND RATIO OF LN(S) OF EXCAVATED TO NON−EXCAVATED SITES)

Update of the 3−D Velocity Model for the DCPP Foundation Area
San Luis Obispo, California

FIGURE 2.3−4

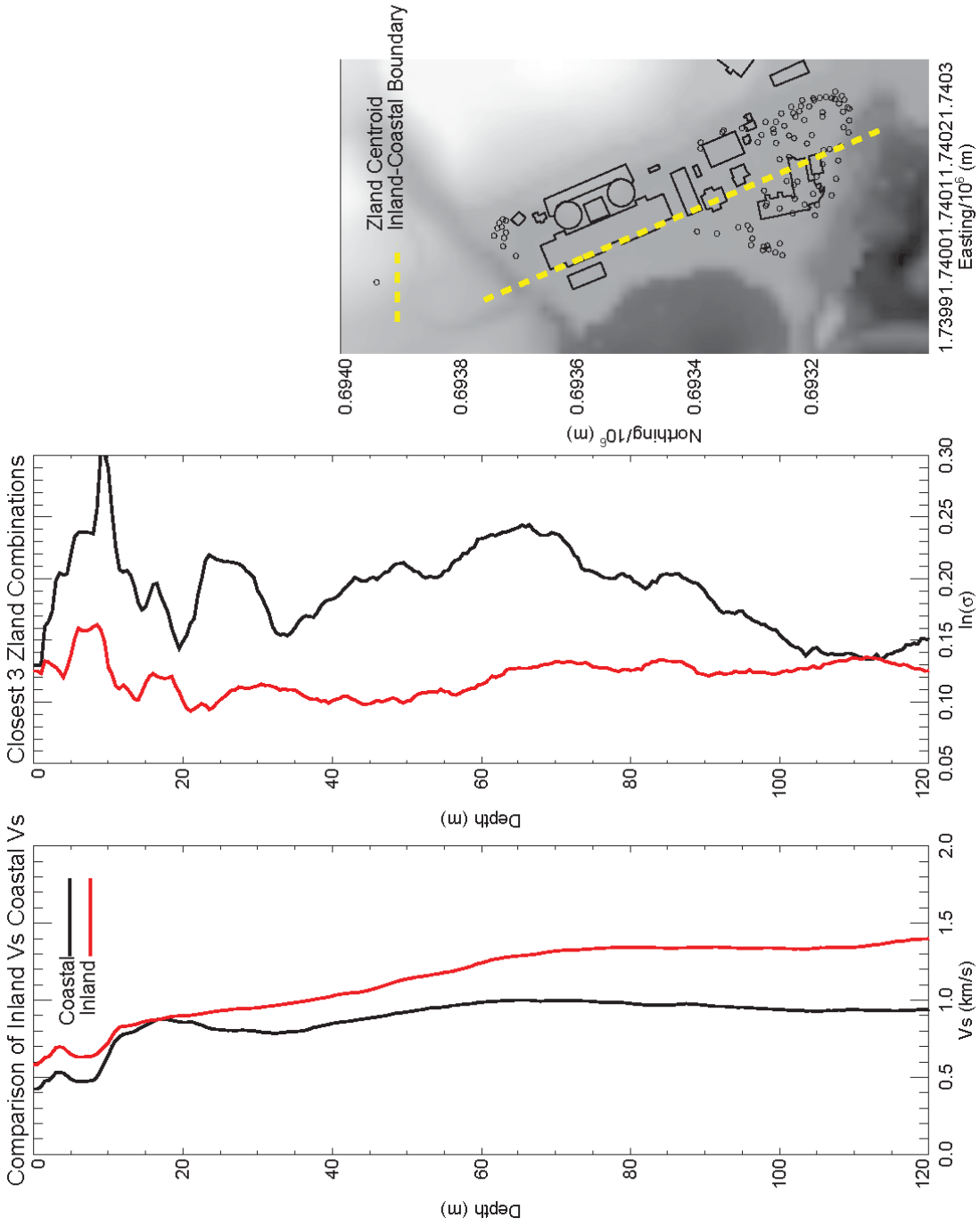

CLOSEST 3 ZLAND COMBINATIONS SORTED INTO INLAND AND COAST SITES (LN−MEAN VS AND LN(S) WITH THE MAP SHOWING THE POSITION OF THE BOUNDARY BETWEEN INLAND AND COASTAL SITES)

Update of the 3−D Velocity Model for the DCPP Foundation Area
San Luis Obispo, California

FIGURE 2.3−5

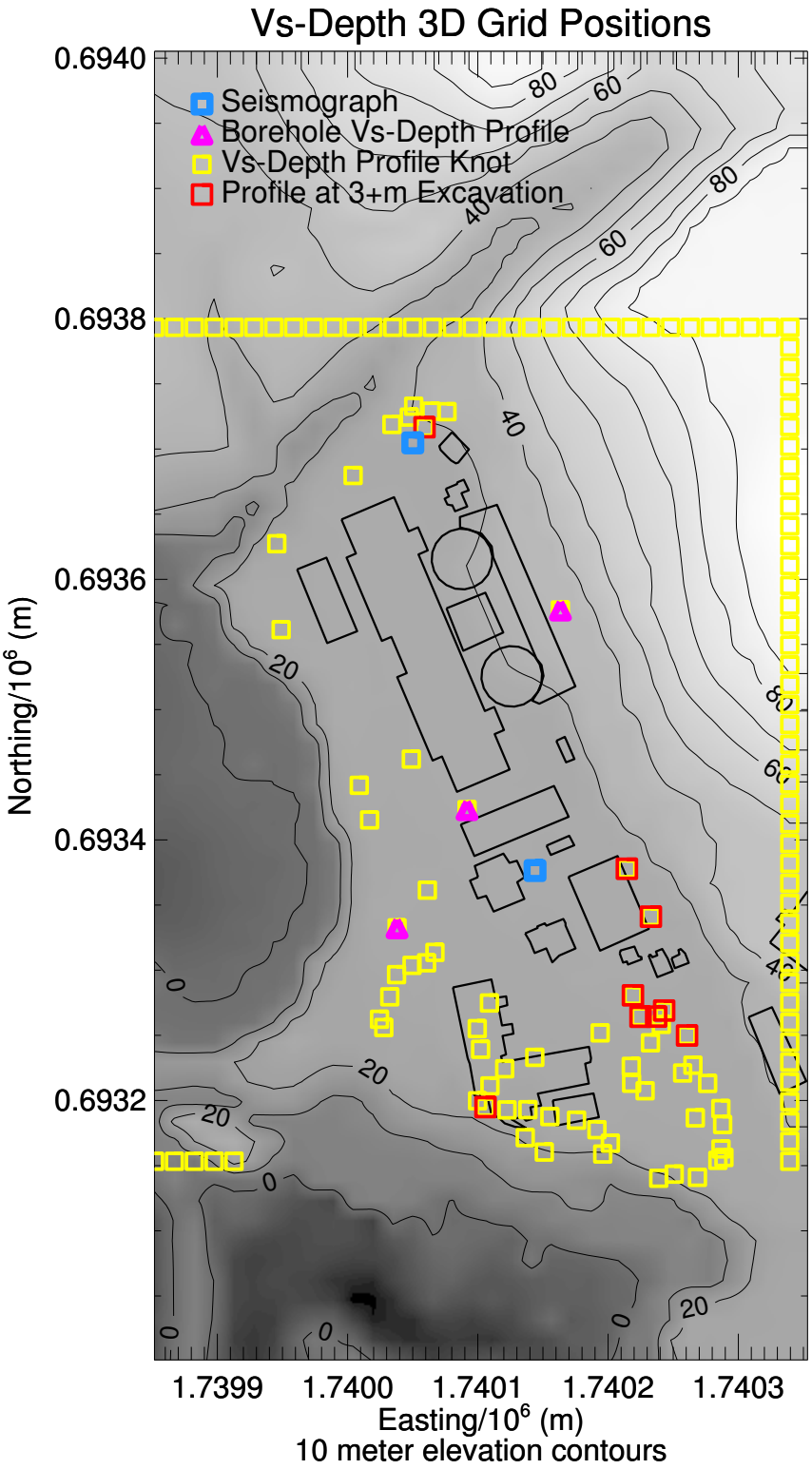

UNIQUE 3D VS GRID CELL POSITIONS WITH VS−DEPTH CONSTRAINTS
Update of the 3−D Velocity Model for the DCPP Foundation Area
San Luis Obispo, California

FIGURE 2.4−1

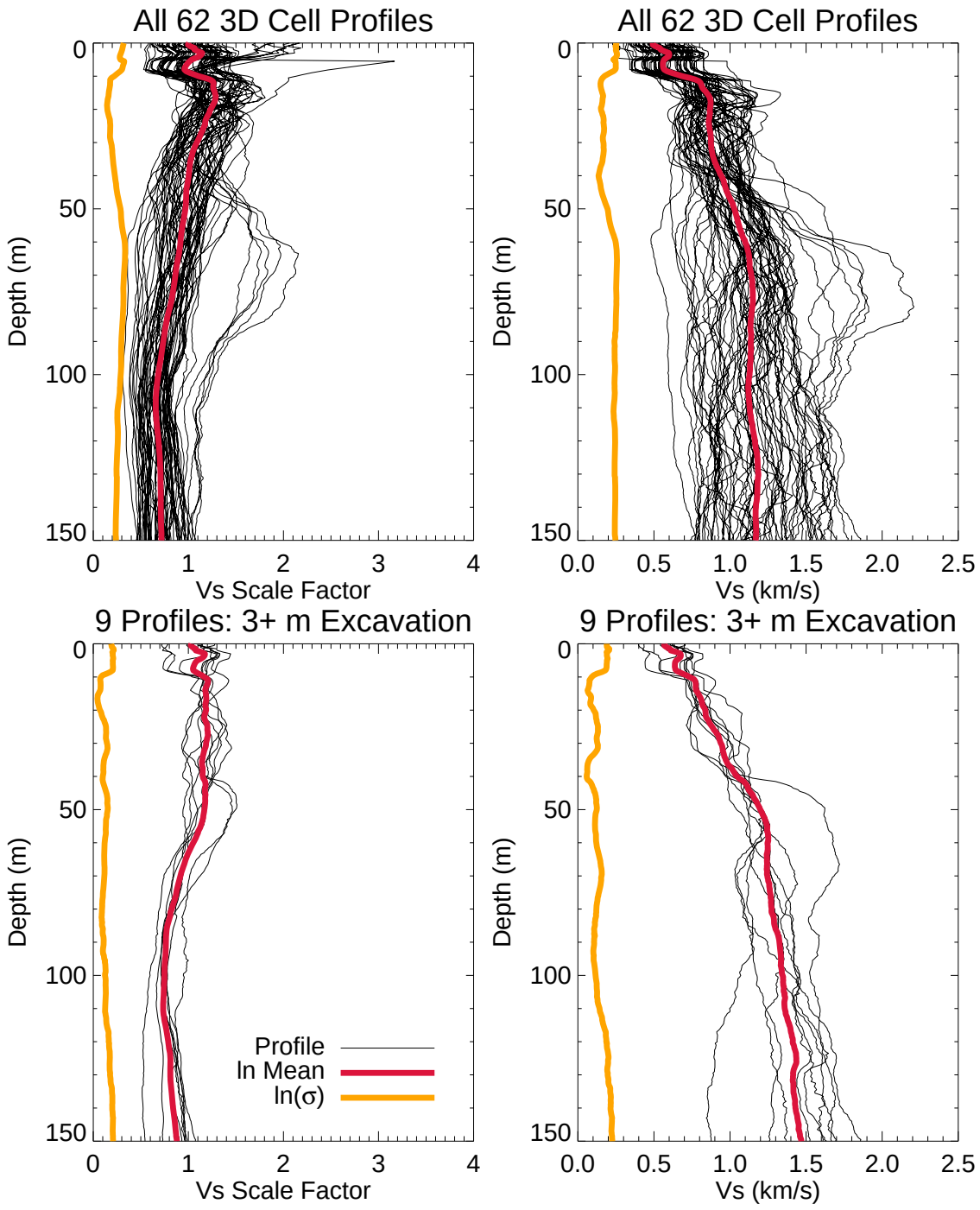

VS−DEPTH VS SCALE FACTORS FROM THE 62 UNIQUE GRID CELL VS−DEPTH PROFILE
Update of the 3−D Velocity Model for the DCPP Foundation Area
San Luis Obispo, California

FIGURE 2.4−2

3.0 UPDATE, VERIFICATION, AND VALIDATION OF THE 3-D VELOCITY MODEL

In order to validate the 3-D velocity model presented in Section 2.0, vertical velocity time histories at the ground surface were generated using a 3-D numerical model and were compared to the observed time histories from the Vibroseis data. The numerical simulations were generated using FLAC^{3D} (Itasca, 2014b).

Six selected subsets of Vibroseis data were selected for the validation of the 3-D velocity model. Two and four subsets are located north and south, respectively, of the Turbine building. These subsets are presented in Section 3.3.3.

3.1 NUMERICAL MODEL VERIFICATION

Before conducting the validation of the velocity model, a verification of the numerical model was conducted to evaluate if FLAC can adequately propagate Rayleigh waves. The numerical model in FLAC was verified by simulating the Lamb's problem (Lamb, 1904), where a transient normal vertical load (source) is applied at the ground surface of an elastic half-space and vertical and horizontal surface displacements are calculated at different horizontal distances from the source.

The numerical model consists of a two-dimensional axisymmetric mesh of size 20.0 by 20.0 m, with a uniform grid size in the horizontal and vertical direction of 0.05 m. The material properties of the numerical model are listed in Table 3.1-1. No material damping was used.

Table 3.1-1. Material Properties of Numerical Model Verification

Property	Value
Unit Weight, γ	20 kN/m^3
Poisson's Ratio	0.25
Shear Wave Velocity, Vs	300.0 m/s
Compression Wave Velocity, Vp	519.6 m/s
Rayleigh Wave Velocity, Vr	275.3 m/s

Figure 3.1-1 shows the FLAC model used for verification. The right and bottom boundaries of the model were modeled with quiet (absorbing) boundaries (Itasca, 2014a) to avoid reflection of outward propagating waves back into the model. The horizontal displacements of the left boundary were fixed to a value of zero to model the axisymmetric conditions.

The applied vertical force is defined by Equation 3.1-1 (Lamb, 1904):

$$F(t) = \frac{F_o}{\pi}\frac{\tau}{t^2 + \tau^2} \tag{3.1-1}$$

where τ is a constant. For a small τ, an impulse loading function is defined. For the analyses presented in this report, the values used for F_o and τ are 1000 and 0.00075, respectively. These values were taken from Nasseri-Moghaddam (2006) and Nasseri-

Moghaddam et al. (2007). Figure 3.1-2 presents graphical representation of the vertical force used herein.

The force shown on Figure 3.1-2 was applied at the ground surface on the left boundary of the mesh. Horizontal and vertical displacement time histories were recorded at the ground surface in a uniform spacing of 0.10 m at horizontal distances from 4.0 to 8.0 m from the source.

The theoretical horizontal and vertical surface displacements far from the source due to a vertical load of the form of Equation 3.1-1 are given in Lamb (1904) and Nasseri-Moghaddam (2006). These theoretical surface displacements consider only the effect of Rayleigh waves.

Figure 3.1-3 presents the comparison of the horizontal (left) and vertical (right) surface displacement time histories generated by FLAC (blue lines) and theoretical solutions (red lines) at horizontal distances of 4.0, 5.0, 6.0, 7.0, and 8.0 m from the source. This figure shows a good agreement between the two sets of displacement time histories. Figure 3.1-3 also shows that the displacements time histories generated by FLAC capture the arrival of P waves, which are more apparent in the horizontal displacement time histories.

Figure 3.1-4 shows the surface particle motion at a horizontal distance of 8.0 m. The particle motion is shown only from 0.0 to 0.066 sec to facilitate the identification of the direction of motion. Figure 3.1-4 shows first the arrival of the P wave, which is more apparent in the horizontal direction. Then this figure shows that the particle motion is in the form of a retrograde ellipse, which is typical of Rayleigh wave motion near the surface.

Figure 3.1-5 show a stack of horizontal and vertical displacement time histories recorded in FLAC at different horizontal distances from the source. The Vp and Vr were calculated from these time histories by tracking the arrival of P and Rayleigh waves with traveled distance. The calculated Vp and Vr are 508.8 and 275.8 m/s, respectively, which agree well with the values listed in Table 3.1-1 (within 2% difference).

The results presented in this section show that FLAC can adequately model the propagation of Rayleigh waves. Additional studies that show a good agreement between simulation of surface waves in FLAC and theoretical solutions can be found in the literature (e.g. Nasseri-Moghaddam, A., 2006; Yang, 2009).

3.2 3-D NUMERICAL MODEL FOR 3-D VELOCITY MODEL VALIDATION

FLAC^{3D} is a 3-D explicit finite-difference program for engineering mechanics computation. Materials (e.g., soil and rock) are represented by polyhedral elements that behave according to a prescribed linear or nonlinear stress/strain law in response to applied forces and boundary restraints.

3.2.1 Material Properties

The subsurface materials were modeled using a linear elastic constitutive model. Strain-dependent modulus degradation due to cyclic loading was not considered. The material properties were defined by the shear-wave velocity, Vs, the Poisson's ratio, ν, and density, ρ. Estimates of these properties were assigned to individual elements of the numerical model.

The shear-wave velocity correspond to the model presented in Section 2.0. The Poisson's ratio was calculated according to the following equation (Santamarina et al, 2001):

$$\nu = \frac{\frac{1}{2}\left(\frac{V_p}{V_s}\right)^2 - 1}{\left(\frac{V_p}{V_s}\right)^2 - 1} \quad (3.2\text{-}1)$$

where Vs and Vp are the shear-wave and compression-wave velocities, respectively, in m/s as presented in Section 2.0. The material density was calculated based on Vs according to the following equation (Fugro, 2015):

$$\rho = 2 + \frac{0.8(V_s - 200)}{3300} \quad (3.2\text{-}2)$$

where ρ is the density in g/cm^3 and Vs is the shear wave velocity in m/s.

Sensitivity analyses were conducted to evaluate the effect of material damping. The Vs-dependent Rayleigh damping formulation used in Fugro (2015) was also used herein. The sensitivity analyses showed that the material damping has an insignificant effect on the results, and therefore, no material damping was used in the results presented in this report.

3.2.2 Input Force

Figure 3.2-1 illustrates the vertical surface force used in the 3-D velocity model validation. This force is described in Section 3.3.1.

3.2.3 Mesh Discretization

Sensitivity analyses were conducted in FLAC to determine the horizontal discretization of the model. The size of the model for these sensitivity analyses is 100 by 30 m in the horizontal and vertical directions, respectively. The material properties of this model are Vs, ν, and unit weight of 200 m/s, 0.3, and 20 kN/m^3, respectively. Similar to the model presented in Section 3.1, the right and bottom boundaries of the model were modeled with quiet (absorbing) boundaries. The horizontal displacements of the left boundary were fixed to a value of zero to model axisymmetric conditions. The vertical force shown on Figure 3.2-1 was applied at the ground surface on the left boundary of the mesh. A uniform vertical discretization of 0.5 m was used.

Figure 3.2-2 presents a comparison of vertical displacement surface time histories recorded at a horizontal distance of 40.0 m from the source for uniform horizontal discretization, Δx, values of 0.5, 1.0, 2.0, 4.0, 5.0, and 8.0 m. For Δx of 0.5, 1.0, and 2.0 m the results are very similar. For larger Δx, the waveform of the time histories changes. Based on the results presented on Figure 3.2-2, a horizontal discretization of 2.0 m was selected.

In order to facilitate the interpolation of the velocity model to a finer grid spacing, the final values of the mesh discretization were selected to be factors of the original grid spacing (i.e. 15.24 and 1.524 m in the horizontal and vertical directions, respectively). The final uniform horizontal and vertical mesh discretization used in the 3-D numerical model are 1.905 and 0.508 m, respectively.

3.2.4 Boundary Conditions

Similar to the numerical model used for verification presented in Section 3.1, the four sides and bottom boundaries of the 3-D numerical model were modeled with quiet (absorbing)

boundaries (Itasca, 2014b) to avoid reflection of outward propagating waves back into the model.

The surface of the 3-D numerical model was modeled using a smooth surface that followed the actual topography by using elements parallel to the ground surface. This avoids the potential wave scattering due to the abrupt change in surface topography when using horizontal elements. Figure 3.2-3 shows an example of the 3-D numerical model used to evaluate the South 2 source-receivers set (see Section 3.3.3). The red and black dots represent the location of the source and receivers, respectively.

3.2.5 Model Extent

In an effort to reduce the number of elements and decrease the computational time, analyses were conducted to evaluate the sensitivity of the results to the horizontal and vertical extents of the numerical model. These sensitivity analyses were conducted using the South 2 source-receivers set (see Section 3.3.3).

To assess the sensitivity to the vertical extent of the model, two numerical models with the same horizontal extent, but with vertical extents to depths of 50 and 100 m were evaluated. Figure 3.2-4 show vertical velocity ground surface time histories for numerical models with vertical extents to depths of 50 and 100 m. These time histories have been cross-correlated with the vertical force shown on Figure 3.2-1. Figure 3.2-4 shows that the difference of the results between the two models is negligible. Therefore, a vertical extent to a depth of 50 m was selected. This is consistent with e.g. Figure 2.2-1, which shows that for the frequencies of interest, most of the Rayleigh wave energy travels in the upper 50 m.

Similarly, to assess the sensitivity to the horizontal extent of the model, two numerical models were evaluated with the same vertical extent, but with horizontal extents so that the minimum distances between the source or any receiver and the model boundary is 25 and 75 m. Figure 3.2-5 show vertical velocity ground surface time histories for these two numerical models. These time histories have been cross-correlated with the vertical force shown on Figure 3.2-1. Figure 3.2-5 shows that the difference of the results between the two models is very small. Therefore, a horizontal extent so that the minimum distance between the source or any receiver and the boundary is 25 m was selected.

3.3 3-D VELOCITY MODEL EVALUATION USING VIBROSEIS GROUND MOTIONS

3.3.1 Filter Response of the Vibroseis Force-Time Function

The observed Zland ground motions are convolved with the filter response corresponding to the frequency response of the Hanning-time taper of the Vibroseis force-time function (Figure 3.3-1). The middle plots in Figure 3.3-1 overplots the low-pass filter applied to the entire Vibroseis sweep with the time-tapered Vibroseis sweep to demonstrate that the low-pass filter produces frequency-time responses consistent with the time-tapered Vibroseis sweep.

3.3.2 Zland Instrument Response

The synthetic ground motions are convolved with the Zland instrument response shown in Figure 3.3-2 to ensure that all instrument response group delays and amplitude variations are accounted for prior to comparing the synthetic ground motions to the low-pass filtered observed ground motions.

3.3.3 Selection of Source-Receivers Sets for Model Validation

Zland ground motions were selected that had sufficient signal-to-noise to model surface-wave arrivals in the Vibroseis sweep frequency band of 8 Hz to < 30 Hz to avoid the 1% g 30 Hz vibrations from the turbines. Ground motions with sufficient signal-to-noise were selected to obtain ground motion source-receivers paths closest to the DCPP foundation and the two seismographic stations that have recorded earthquake ground motions (ESTA 27 and 28) as indicated in Figure 2.1-7b. Waveforms from seven source positions where selected for initial waveform analyses as shown in Figures 3.3-3 to 3.3-9. Since each FLAC synthetic time history calculation requires a significant amount for each source position a moderate number of source-position sets were analyzed to focus on regions closest to the DCPP foundation. After the 3-D Vs model update, synthetic waveforms were recalculated for six source positions, omitting the South Set 1 set (Figure 3.3-5) since these source-receiver paths were not located close to the primary DCPP foundation area.

3.3.4 Comparison of Synthetic and Observed Velocity Time Histories

To extract the relative Vs slowness inconsistency between synthetic and observed waveform in the form of group-arrival-time deviations of the synthetic waveforms relative to the observed waveforms, we use the stretching method (Hadziioannou et al., 2009). A grid search is used with fractional stretching increments of 0.001 to find the minimum synthetic waveform stretching required to maximize the cross correlation of the synthetic and observed waveforms. A positive stretch indicates that the synthetic arrival times are early and velocities along the source-receiver path are too high on average. Conversely, a negative stretch indicates that the synthetic waveform arrival times are late and the velocities along the source-receiver path need to be increased on average.

Since the shallow ground conditions are highly variable across the source and receiver sites in terms of buried infrastructure ranging from open conduit channels, subsurface fuel drums, cooling system pipes, and various other irregular buried shapes, absolute amplitude comparisons of synthetic and observed time histories will not be a realistic approach. The distribution of energy (proportional to ground velocity recorded by the Zland receivers) through time is a function of group velocity. Thus it is not necessary to compare absolute synthetic and observed velocity time history amplitudes but simply the distribution of amplitude (energy) through time. Consequently, the synthetic and observed velocity time histories are scaled by their respective maximum absolute amplitudes prior to cross-correlation analyses.

The waveform cross-correlation analyses for all Vibroseis ground motion time histories are provided in Appendix D. Corresponding waveform Vs-depth sensitivity plots are provided in Appendix E. A subset of pairs of Appendix D and E analyses are presented here to explain the plots and analyses. The first sets of analyses are presented in the southern portion of the DCPP foundation where the waveform analyses were used to update the 3-D Vs model as discussed in Section 3.3.5. Explanation of the cross-correlation and Vs-depth sensitivity analyses provide the foundation for the 3-D Vs model tomographic update in Section 3.3.5.

Figures 3.3-10 and 3.3-11 show the cross-correlation and Vs-depth sensitivity analyses, respectively, for a source-receiver path crossing just south of seismic station ESTA 27 (southern blue square in the maps). This particular source-receiver path does not extend beneath a building. The updated 3-D Vs model explains the observed waveform very well with a cross-correlation of 0.88 (upper right plot in Figure 3.3-10). The overall duration of shaking is also very

well reproduced in the time window of primary surface-wave arrivals delineated by the region between the vertical dashed lines in the plots on the right of Figure 3.3-10. The cross-correlation of the observed and synthetic trace envelopes is 0.92 in the time window between the vertical-dashed lines, indicating the updated 3-D Vs model is very consistent with the observed ground motion responses along this path. Stretching the synthetic waveform by -0.9% increasing the waveform cross-correlation to 0.92 (bottom right plot in Figure 3-3-10) indicated that the shallow velocities along this source-receiver path would need to be increased about ~1% to best match the observed ground motion. Figure 3.3-11 shows the observed waveform frequency response in the middle right figure and the group-velocity-depth sensitivity functions for the three frequencies denoted by the colored dashed lines in the frequency plot. The low (blue) and high (red) frequencies correspond to cumulative energies of 10% and 90% and the green frequency is the frequency with the maximum amplitude response. The highest frequency portion of the ground motion is primarily sensitive to velocities in the 0-15 m depth range (red curve in the lower right plot of Figure 3.3-11) while the lower frequencies have significant velocity sensitivity to about 30 m (blue curve in the lower right plot of Figure 3.3-11). Thus, the combination of the waveform cross-correlation and sensitivity analyses plots show how well the velocity model is performing, how much the velocity model should be adjusted to better fit the observed ground motion, and what depth range of the velocity model is best resolved by the ground motion time history.

The source-receiver path in Figures 3.3-12 and 3.3-13 extends further southwest. The cross-correlation analysis indicated that the 3D velocity model is about 5% fast along this path; a 5% stretching of the synthetic waveform increased the waveform cross-correlation from 0.16 to 0.96 (Figure 3.3-12). The waveform sensitivity analyses shows that the high-frequency portion of the ground motion constrains Vs from 0-15 m depth while the low-frequency waveform constrains Vs to depths of 35 m (Figure 3.3-13). A nearby source-receiver path indicates that the updated 3-D Vs model is 0.3% slow (Figures 3.3-14 and 3.3-15).

The source-receiver path in Figures 3.3-16 and 3.3-17 extends through seismic station ESTA 27 and beneath a building. The cross-correlation analyses shows that the Vs model is about 2% fast along this path with the cross-correlation increasing from 0.72 to 0.83 by stretching the synthetic waveform 2% (Figure 3.3-16). The lower cross correlation relative to the previous three source-receiver paths presented in Figures 3.3-10 to 3.3-15 is characteristic of source-receiver paths that extend below buildings. However, the waveform sensitivity analysis in Figure 3.3-17 shows that Vs is well constrained to about 30 m depth by the waveform data indicated that the shallow Vs structure below seismic station ESTA 27 is well constrained.

The source-receiver path in Figures 3.3-18 and 3.3-19 extends beneath several buildings. The cross-correlation analyses shows that the Vs model is about 11% slow along this path with the cross-correlation increasing from 0.08 to 0.89 by compressing the synthetic waveform 11% (Figure 3.3-18). The waveform sensitivity analyses shows that the high-frequency portion of the ground motion constrains Vs from 0-20 m depth while the low-frequency waveform constrains Vs to depths of 35 m (Figure 3.3-19).

The source-receiver path in Figures 3.3-20 and 3.3-21 extends east of the southern portion of the DCPP foundation. The cross-correlation analyses shows that the Vs model is about 5% fast along this path with the cross-correlation increasing from 0.58 to 0.95 by stretching the synthetic waveform 5% (Figure 3.3-20). The waveform sensitivity analyses shows

that the high-frequency portion of the ground motion constrains Vs from 0-15 m depth while the low-frequency waveform constrains Vs to depths of 35 m (Figure 3.3-21).

The source-receiver path in Figures 3.3-22 and 3.3-23 extends from near borehole DDH-C at the north end to just east of borehole DDH-A-2 to the south. The cross-correlation analyses shows that the Vs model is about 5% slow along this path with the cross-correlation increasing from 0.19 to 0.80 by compressing the synthetic waveform 5% (Figure 3.3-22). The waveform sensitivity analyses shows that the high-frequency portion of the ground motion constrains Vs from 0-15 m depth while the low-frequency waveform constrains Vs to depths of 35 m (Figure 3.3-23).

The source-receiver path in Figures 3.3-24 and 3.3-25 extends 17 m west from near borehole DDH-C. The cross-correlation analyses shows that the Vs model is about 5% slow along this path with the cross-correlation increasing from 0.79 to 0.91 by compressing the synthetic waveform 5% (Figure 3.3-24). The waveform sensitivity analyses shows that the high-frequency portion of the ground motion constrains Vs from 0-20 m depth while the low-frequency waveform constrains Vs to depths of 50 m (Figure 3.3-25). The ground motions along this source-receiver path provide more valuable and relevant constraints on Vs-depth than the downhole data in borehole DDH-C because the waveform constraints extend deeper than the borehole DDH-C shear-wave traveltimes, which become highly uncertain at 40-m depth, and the waveform analysis represents validation of 3-D Vs structure over a 17-m path corresponding to seismic wavelengths of interest for site response analyses.

The source-receiver path in Figures 3.3-26 and 3.3-27 extends along the south side of Diablo Canyon and north of seismic station ESTA 28 (north blue square on the maps). The cross-correlation analyses shows that the Vs model is about 11% slow along this path with the cross-correlation increasing from -0.77 to 0.85 by compressing the synthetic waveform 11% (Figure 3.3-26). The waveform sensitivity analyses shows that the high-frequency portion of the ground motion constrains Vs from 0-15 m depth while the low-frequency waveform constrains Vs to depths of 35 m (Figure 3.3-27). The Vs low-velocity zone at depths between 15 m and 45 m reduces the group Vs-depth sensitivity below the low-velocity zone lid as indicated the relatively low amplitude low-frequency Vs-depth sensitivity kernels in Figure 3.3-27.

The source-receiver path in Figures 3.3-28 and 3.3-29 extends from the south side of Diablo Canyon ESE to the northeast side of the DCPP foundation passing just south of seismic station ESTA 28 (north blue square on the maps). The cross-correlation analyses shows that the Vs model is about 2% slow along this path with the cross-correlation increasing from 0.67 to 0.80 by compressing the synthetic waveform 2% (Figure 3.3-28). The waveform sensitivity analyses shows that the high-frequency portion of the ground motion constrains Vs from 0-15 m depth while the low-frequency waveform constrains Vs to depths of 40 m (Figure 3.3-29). The Vs low-velocity zone at depths between 15 m and 45 m is less pronounced than the Vs-depth structure to the north in Figures 3.3-26 and 3.3-27, so group Vs-depth sensitivity below the low-velocity zone lid is not as relatively low amplitude for low-frequency Vs-depth sensitivity kernels in Figure 3.3-29.

The source-receiver path in Figures 3.3-30 and 3.3-31 extends from the south side of Diablo Canyon ESE to the northeast side of the DCPP foundation passing just north of seismic station ESTA 28 (north blue square on the maps) and extends east up the slope away from the DCPP foundation area. The cross-correlation analyses shows that the Vs model is about 2%

slow along this path with the cross-correlation increasing from 0.45 to 0.58 by compressing the synthetic waveform 2% (Figure 3.3-30). The waveform sensitivity analyses shows that the high-frequency portion of the ground motion constrains Vs from 0-15 m depth while the low-frequency waveform constrains Vs to depths of 40 m (Figure 3.3-31). This source-receiver path's east end extends beyond the northeast surface-wave constraints on Vs-depth. However, the termination of the surface wave energy at 0.45 s in the synthetic data shows the 3-D Vs model performs well to depths of 40 m northeast of the main DCPP foundation. The Vs low-velocity zone at depths between 15 m and 45 m is less pronounced than the Vs-depth structure to the north in Figures 3.3-26 and 3.3-27, so group Vs-depth sensitivity below the low-velocity zone lid is not as relatively low amplitude for low-frequency Vs-depth sensitivity kernels in Figure 3.3-31.

The source-receiver path in Figures 3.3-32 and 3.3-33 extends from the south side of Diablo Canyon ESE to the northeast side of the DCPP foundation passing directly beneath seismic station ESTA 28 (north blue square on the maps). The cross-correlation analyses shows that the Vs model is about 1% slow along this path with the cross-correlation increasing from 0.63 to 0.65 by compressing the synthetic waveform 1% (Figure 3.3-32). The waveform sensitivity analyses shows that the high-frequency portion of the ground motion constrains Vs from 0-20 m depth while the low-frequency waveform constrains Vs to depths of 40 m (Figure 3.3-33). The waveform analysis along this source-receiver path show that the Vs-depth structure beneath seismic station ESTA 28 is well constrained to 40 m.

The source-receiver path in Figures 3.3-34 and 3.3-35 extends from the south side of Diablo Canyon southeast to the northeast side of the DCPP foundation passing just south of seismic station ESTA 28 (north blue square on the maps) and extends east up the slope away east from the DCPP foundation area. The cross-correlation analyses shows that the Vs model is about 5% fast along this path with the cross-correlation increasing from 0.21 to 0.81 by stretching the synthetic waveform 5% (Figure 3.3-34). The waveform sensitivity analyses shows that the high-frequency portion of the ground motion constrains Vs from 0-25 m depth while the low-frequency waveform constrains Vs to depths of 50 m (Figure 3.3-35). This source-receiver path's east end extends beyond the northeast surface-wave constraints on Vs-depth. However, the termination of the surface wave energy at 0.45 s in the synthetic data shows the 3-D Vs model performs well to depths of 50 m through the northeast portion of the main DCPP foundation.

Since there was no waveform-based tomographic update of the northern portion of the 3-D Vs model, waveform cross-correlations are generally lower than the south waveforms. However, the waveform provide strong constraints on northern DCPP foundation 3-D Vs to depths of 35-50 m as shown in Figures 3.3-26 to 3.3-35.

3.3.5 Tomographic Update of the 3-D Vs Model to Estimate Vs Biases and Uncertainties

Assembled group-arrival-time deviations from all source-receiver paths (Appendix D) can provide sufficient information to update 3-D velocities in the region at the south end of the DCPP foundation with many intersecting source-receiver paths that have a wide range of azimuths (Figure 3.3-36). In Figure 3.3-36, red-dashed lines show slow source-receiver paths and yellow-dashed lines show fast source-receiver paths. This portion of the southern DCPP foundation area had sufficient source-receiver waveform path coverage to invert group-arrival-

time delays for Vs perturbation using a 2-D distribution of 25-m wide square cells spanning the region of wave path intersections (Figure 3.3-36).

A first-order Taylor-series expansion results in the matrix relationship between slowness perturbations, Δs_j, and group delays, Δt_i, and path distances through the 2D cells, Δh_{ij}

$$\Delta t_i = \sum_{j=1}^{nc} \Delta s_j \Delta h_{ij} \qquad (3.3\text{-}1)$$

for $i=1,n_d$ group-delay observations and $j=1,n_c$ 2-D cells. This linear matrix equation is solved to estimate Δs_j using singular-value-decomposition damped least squares with the damping set to minimize Δs_j while maximizing variance reduction. The spatial distribution of estimated Δs_j converted to Vs adjustments for display (Figure 3.3-37) produced the final updated 3-D Vs model that substantially reduced group-delays variability for the South Set 2 source-receiver waveform paths that are located within the central portion of the 2-D tomography grid (Figure 3.3-6). In particular the group-delay variability (*ln*(s)) for the South Set 2 waveform set (bold value in Table 3.3-1) was reduced by a factor of 1.83 relative to all the waveform groups (italic value in Table 3.3-1). This corresponds to a variance reduction of 3.34 for the South Set 2 waveform set relative to the group-delay variance of all six waveform sets.

The 2-D tomographic update of the 3-D Vs model produced variance reduction in Vs bias, increases in waveform cross-correlations, and reductions of waveform cross correlation variance for the South Set 2 waveform group that quantitatively demonstrate that the 2-D tomographic approach resolves lateral Vs variations very well (Table 3.3-1) and that measured group-delays are directly proportional to model Vs uncertainties. Thus, the statistics of observed group-delays provide accurate first-order estimates of Vs biases and uncertainties associated with velocities in the top 40-50 m of the final 3-D velocity model. Since waveform paths are not available that cross all portions of the DCPP foundation with a wide range of azimuths, the largest Vs *ln*(σ) observed Table 3.3-1 in the northern waveform sets outside the area of 2-D tomographic velocity update provides a sound estimate of Vs uncertainties in the top 40-50 m, the depth range throughout the portions of the 3-D Vs DCPP foundation model outside the area of 2-D tomographic 3-D Vs updates.

Table 3.3-1. Final 3-D Vs Model Biases, Uncertainties, and Waveform Fit Statistics

Waveform Set	*Ln*-Mean Vs Bias (%)	Vs *ln*(σ)	Median Waveform Cross-Correlation	Waveform Cross-Correlation σ
All 6 Groups	0.7	*0.081*	0.71	0.17
2 North Groups	3.7	0.090	0.58	0.17
4 South Group	-0.7	0.074	0.78	0.14
South Set 2 Group	-1.8	**0.044**	0.87	0.10

The waveform analysis estimates of Vs *ln*(σ) of 0.09 in the top 50 m of the 3D Vs model in the DCPP foundation area are consistent and slightly lower than the Vs-depth uncertainties estimate that only using surface-wave phase slowness constraints of Vs *ln*(σ)=0.1-0.15 in the DCPP foundation area (Figures 2.3-2 and 2.3-5). Thus a slightly conservative approach to assigned Vs-depth uncertainties in the DCPP foundation area is to assign Vs *ln*(σ)=0.15 for the top 10 m of heterogeneous material (weathering rind, backfill, shallow facility buried structures, etc.), Vs *ln*(σ)=0.1 from 10 m depth to 50 m depth, Vs *ln*(σ) increasing from 0.1 at 50 m depth to 0.16 at 60 m depth, and increasing to 0.18 at 120 m depth consistent with surface-wave estimates of deeper Vs uncertainties (Figures 2.3-2 and 2.3-5).

Comparisons of the PR-16 and revised 3-D Vs models are presented in Appendices F and G in the E-W and N-S directions, respectively. These appendices show 2-D Vs contours of the two 3-D Vs models, and contours of the Vs ratio of the revised to the PR-16 model.

3.4 ALTERNATIVE 3-D VS MODELS TO ACCOUNT FOR EPISTEMIC UNCERTAINTIES

The surface-wave dispersion Vs-depth uncertainty analyses (Figures 2.3-2 and 2.3-5) show that velocity variability and uncertainty are a function of position with substantially lower Vs-depth variability beneath the DCPP foundation area relative to the areas close to the coast. Waveform group-delay analyses of the subsets of source-receiver paths located near the coast in South Set 5 and North Set 3 (Appendix D) are consistent with higher Vs variability near the coast. Table 3.4-1 provides l*n*(σ) uncertainties appropriate to create two bounding 3-D velocity models to evaluate site response. The minimum and maximum amplification scenarios to first order can be constructed by systematically decreasing and increasing Vs, respectively, in the 50-120 m depth ranges using the Vs *ln*(σ) values in Table 3.4-1.

Table 3.4-1. Final 3-D Vs Vs-Depth Uncertainties to Account for Epistemic Uncertainties

Depth Range (m)	DCPP Foundation Vs *ln*(σ)	West of DCPP Foundation Vs *ln*(σ)
0-10	0.15	0.20
10-50	0.1	0.15
50-60	0.1-0.15	0.15-0.20
60-120	0.15-0.18	0.20

Since the final 3-D Vs model provides very good fits to the observed Vibroseis ground motions, the weights in Table 3.4-2 provide appropriate accounting for 3-D velocity model epistemic uncertainties.

Table 3.4-2. Final 3-D Vs Model Scenario Weights

Final 3-D Vs model	Deep Slower Vs Model	Deep Faster Vs Model
0.68	0.16	0.16

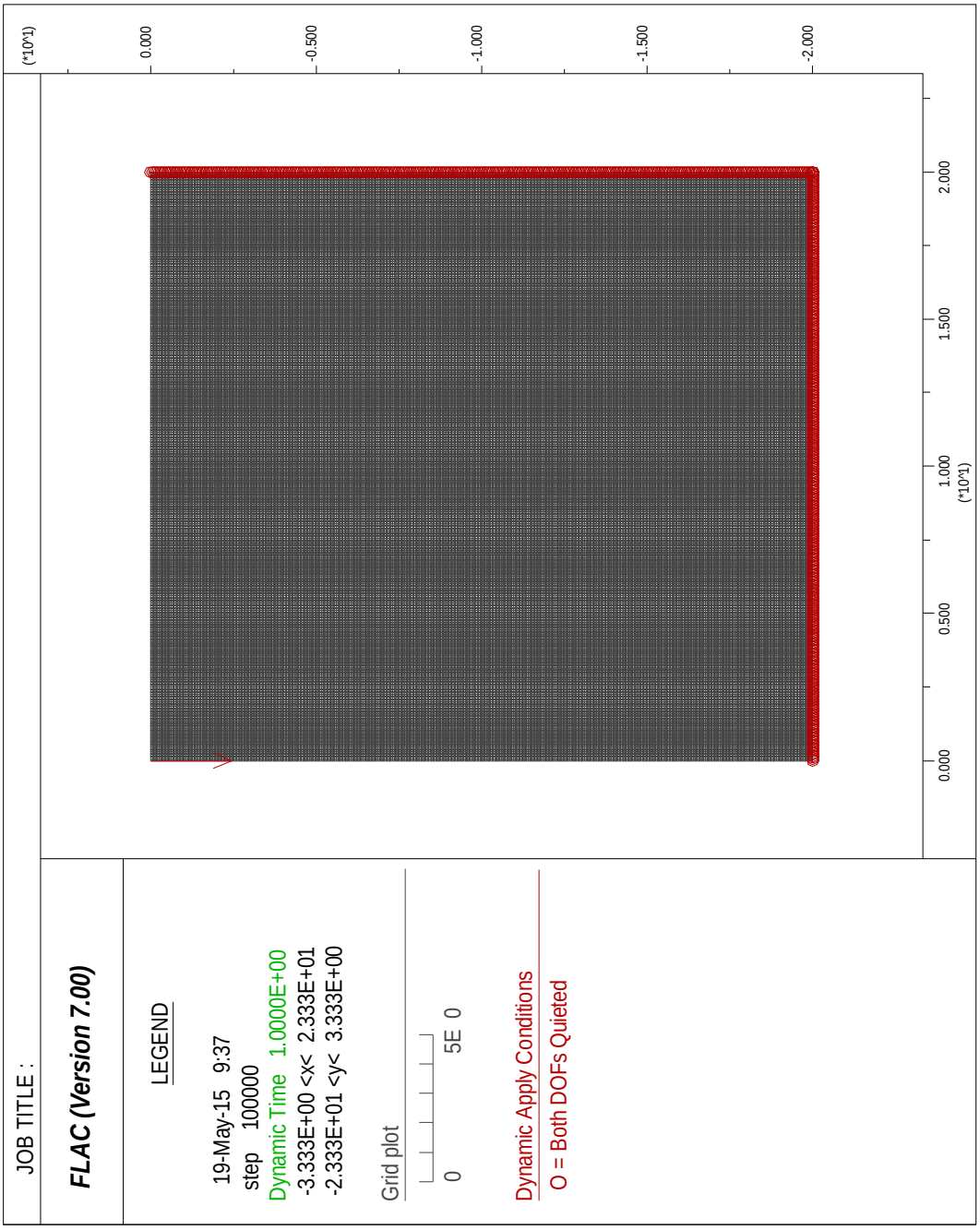

FLAC NUMERICAL MODEL USED FOR VERIFICATION
Update of the 3−D Velocity Model for the DCPP Foundation Area
San Luis Obispo, California

FIGURE 3.1−1

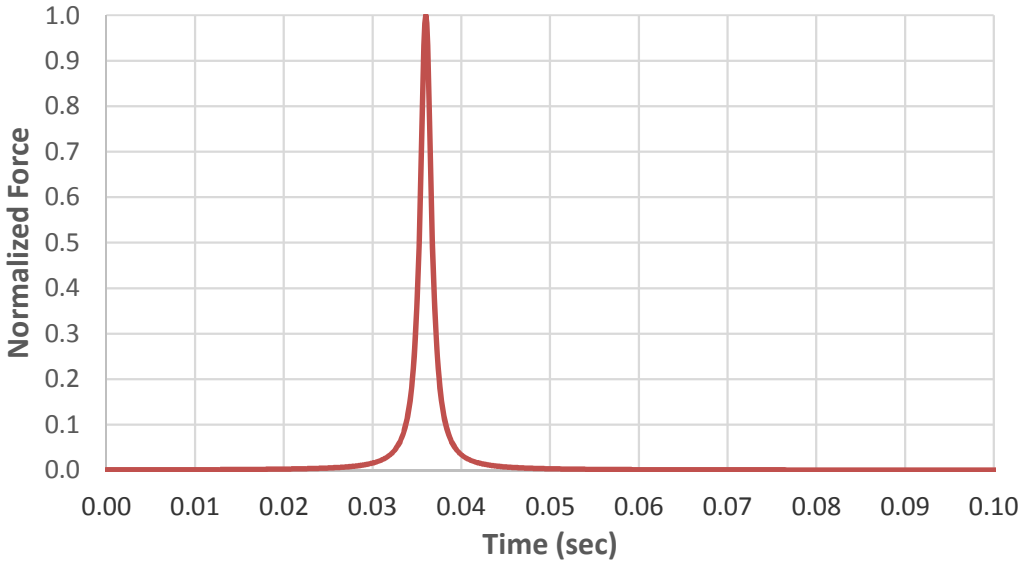

VERTICAL FORCE USED FOR VERIFICATION
Update of the 3−D Velocity Model for the DCPP Foundation Area
San Luis Obispo, California

FIGURE 3.1−2

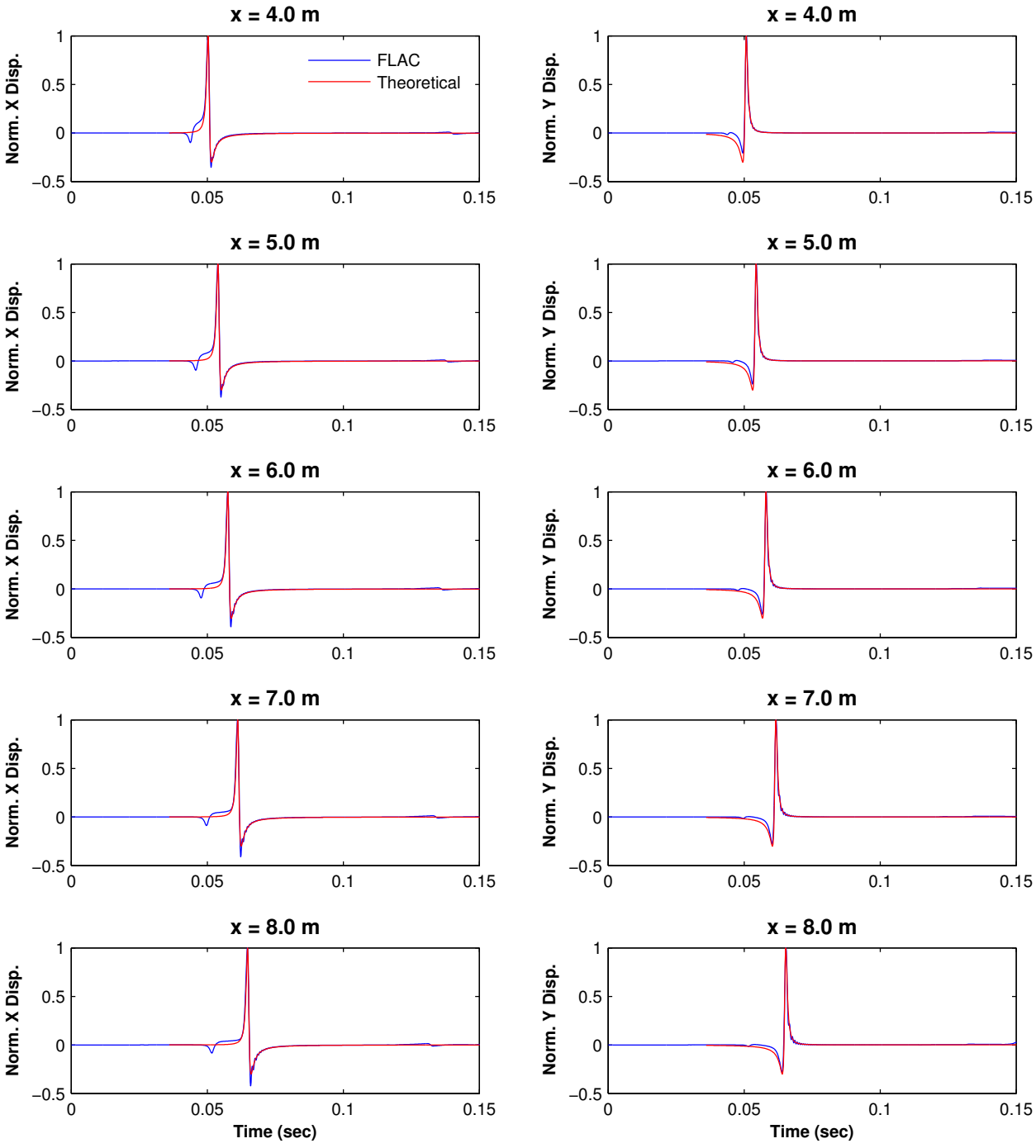

COMPARISON OF FLAC AND THEORETICAL
HORIZONTAL AND VERTICAL SURFACE DISPLACEMENT TIME HISTORIES
Update of the 3−D Velocity Model for the DCPP Foundation Area
San Luis Obispo, California

FIGURE 3.1−3

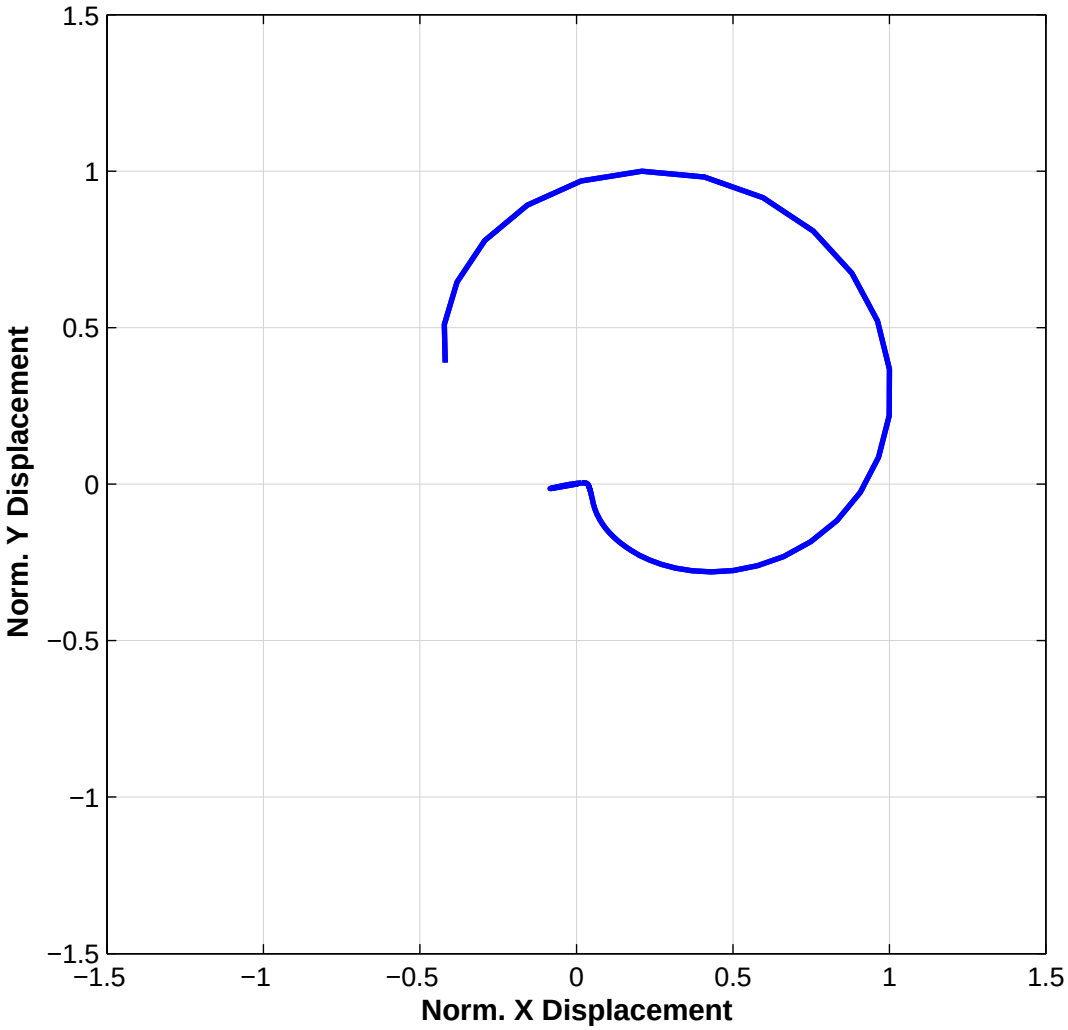

SURFACE PARTICLE MOTION AT X = 8 M FROM 0.0 TO 0.066 SEC
Update of the 3−D Velocity Model for the DCPP Foundation Area
San Luis Obispo, California

FIGURE 3.1−4

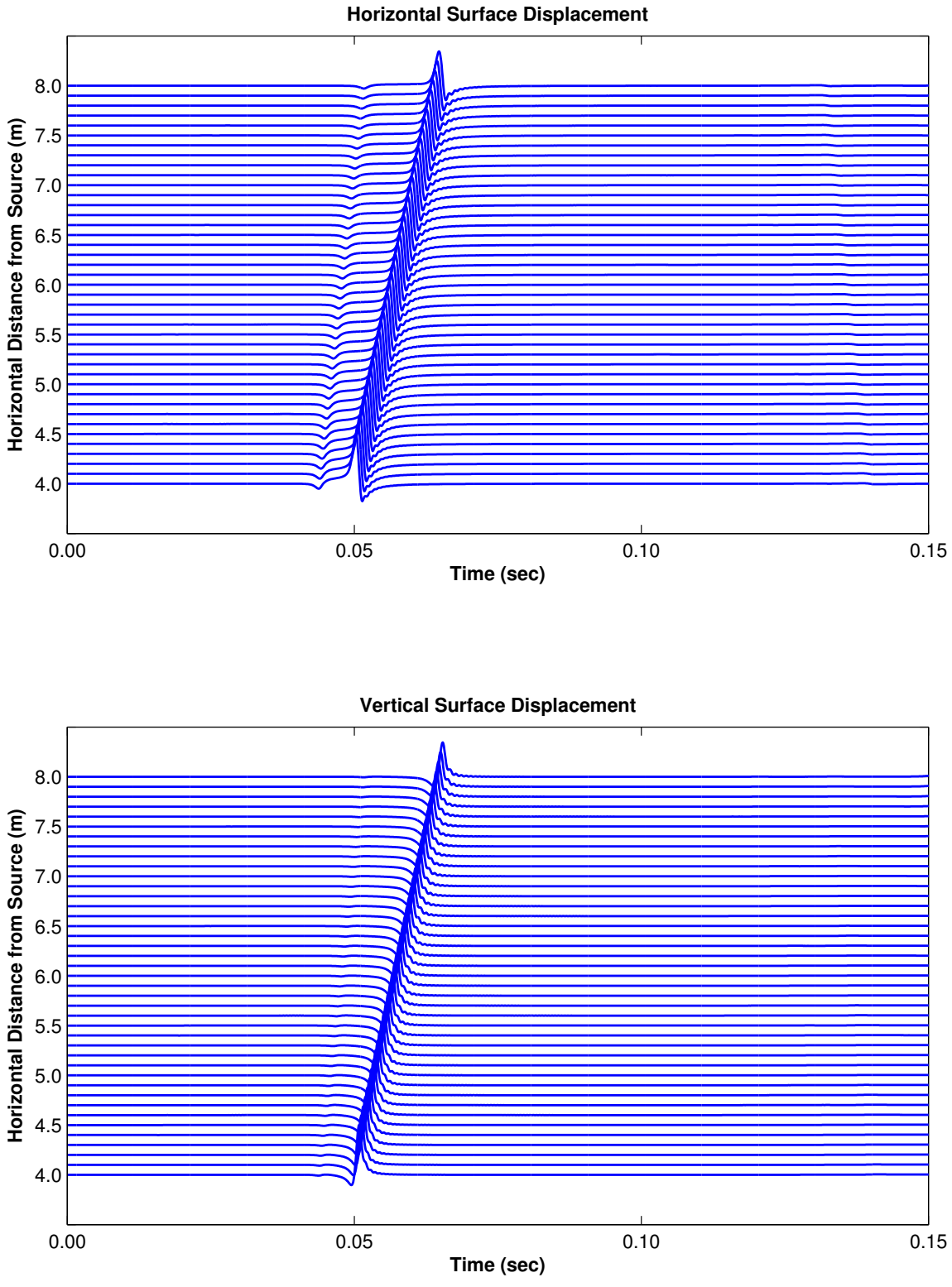

HORIZONTAL AND VERTICAL SURFACE DISPLACEMENT TIME HISTORIES RECORDED IN FLAC AT DIFFERENT HORIZONTAL DISTANCES FROM THE SOURCE

Update of the 3−D Velocity Model for the DCPP Foundation Area
San Luis Obispo, California

FIGURE 3.1−5

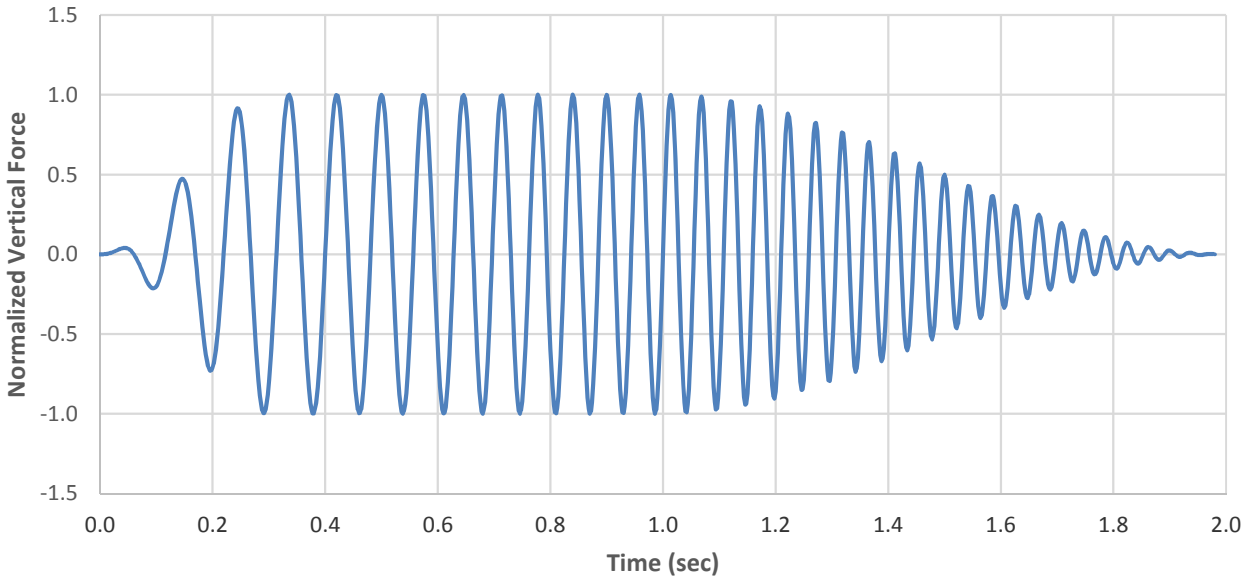

VERTICAL SURFACE FORCE USED IN THE 3−D VELOCITY MODEL VALIDATION
Update of the 3−D Velocity Model for the DCPP Foundation Area
San Luis Obispo, California

FIGURE 3.2−1

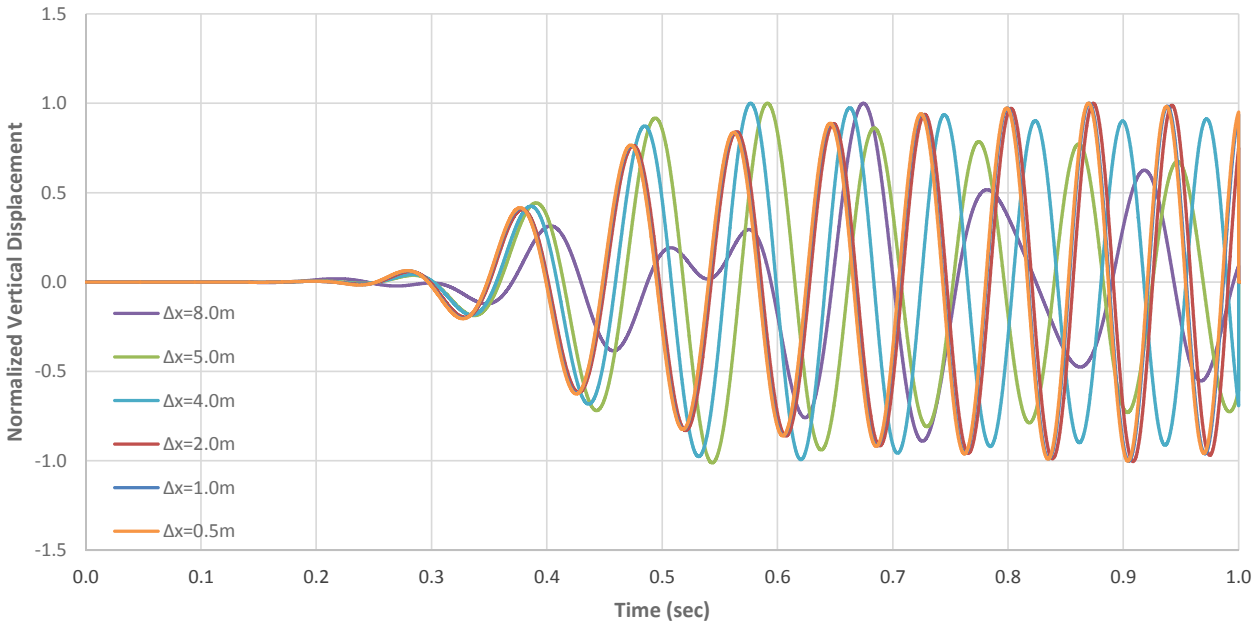

COMPARISON OF VERTICAL DISPLACEMENT SURFACE TIME HISTORIES FOR DIFFERENT HORIZONTAL DISCRETIZATIONS

Update of the 3−D Velocity Model for the DCPP Foundation Area
San Luis Obispo, California

FIGURE 3.2−2

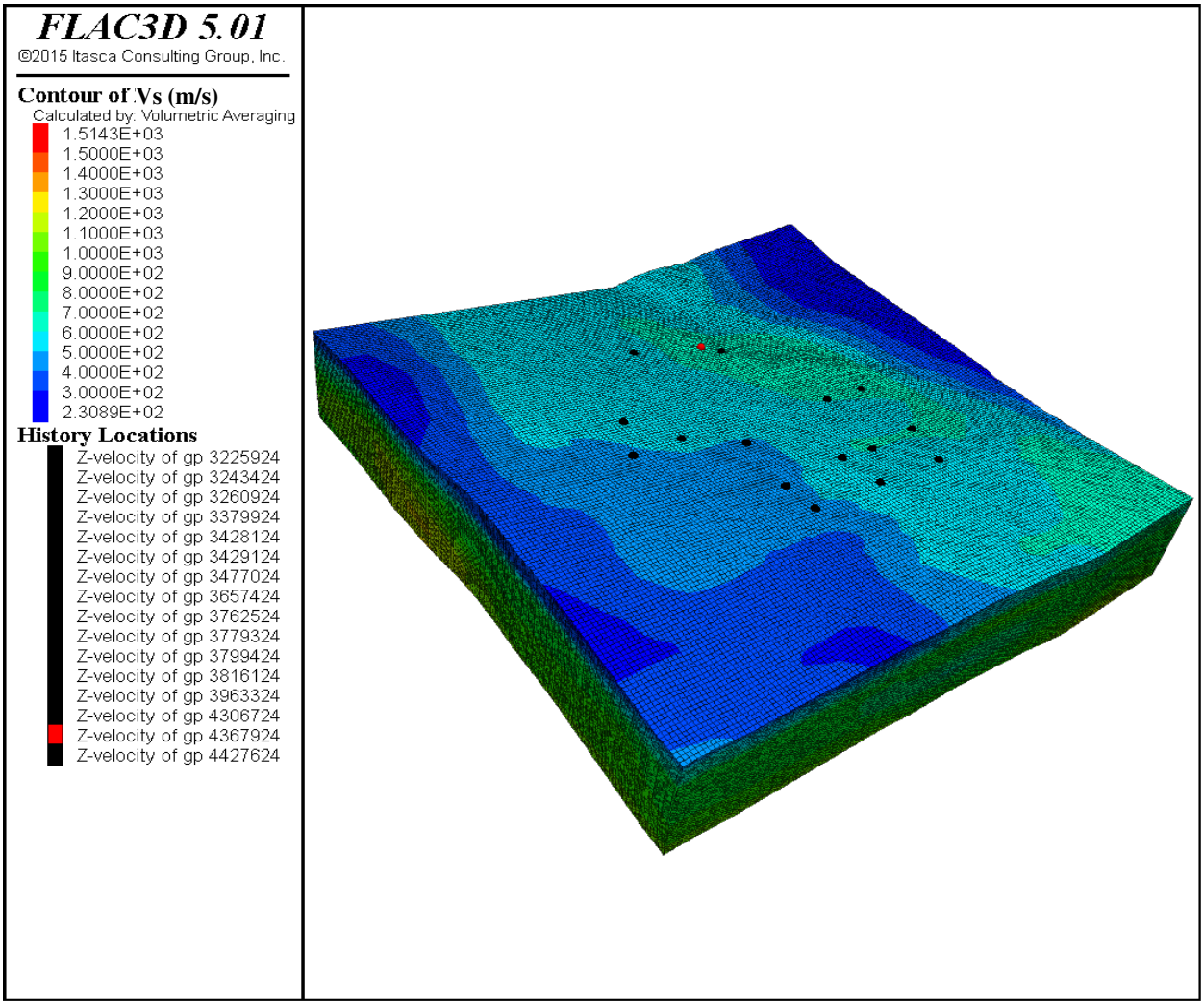

EXAMPLE OF THE 3−D NUMERICAL MODEL USED TO EVALUATE THE SOUTH 2 SOURCE−RECEIVERS SET

Update of the 3−D Velocity Model for the DCPP Foundation Area
San Luis Obispo, California

FIGURE 3.2−3

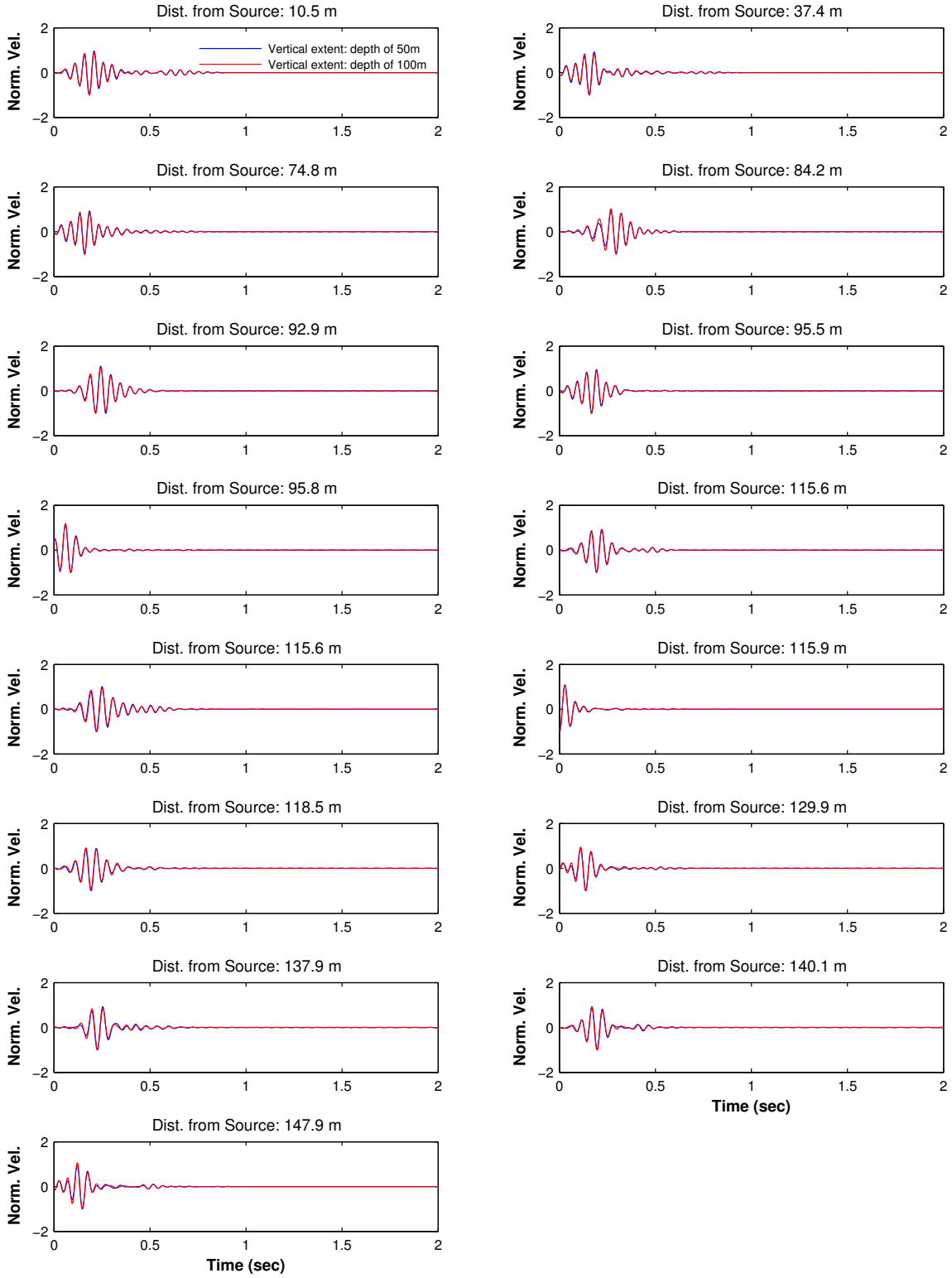

COMPARISON OF VERTICAL VELOCITY GROUND SURFACE TIME HISTORIES FOR NUMERICAL MODELS WITH DIFFERENT VERTICAL EXTENTS

Update of the 3−D Velocity Model for the DCPP Foundation Area
San Luis Obispo, California

FIGURE 3.2−4

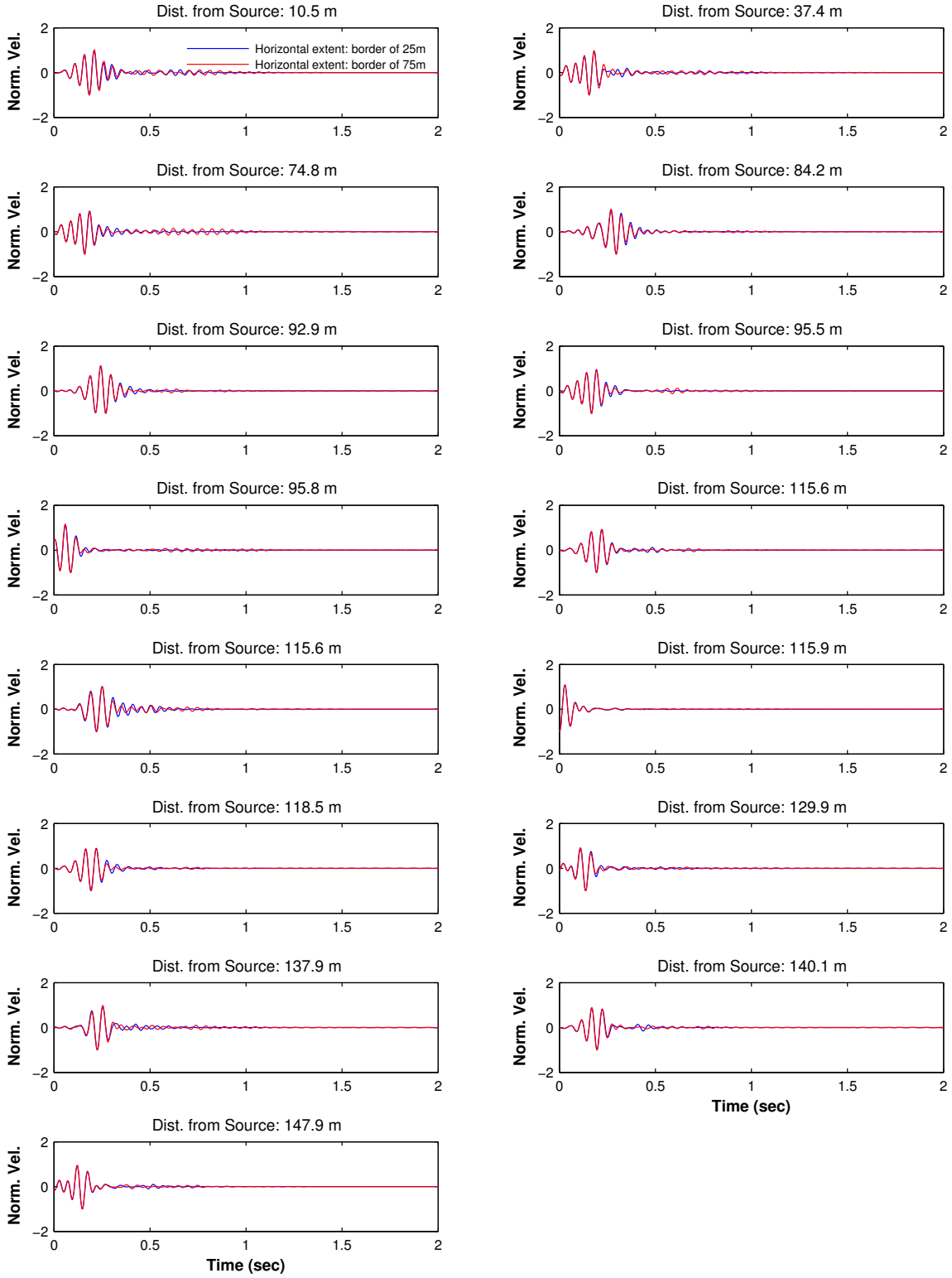

COMPARISON OF VERTICAL VELOCITY GROUND SURFACE TIME HISTORIES FOR NUMERICAL MODELS WITH DIFFERENT HORIZONTAL EXTENTS

Update of the 3−D Velocity Model for the DCPP Foundation Area
San Luis Obispo, California

FIGURE 3.2−5

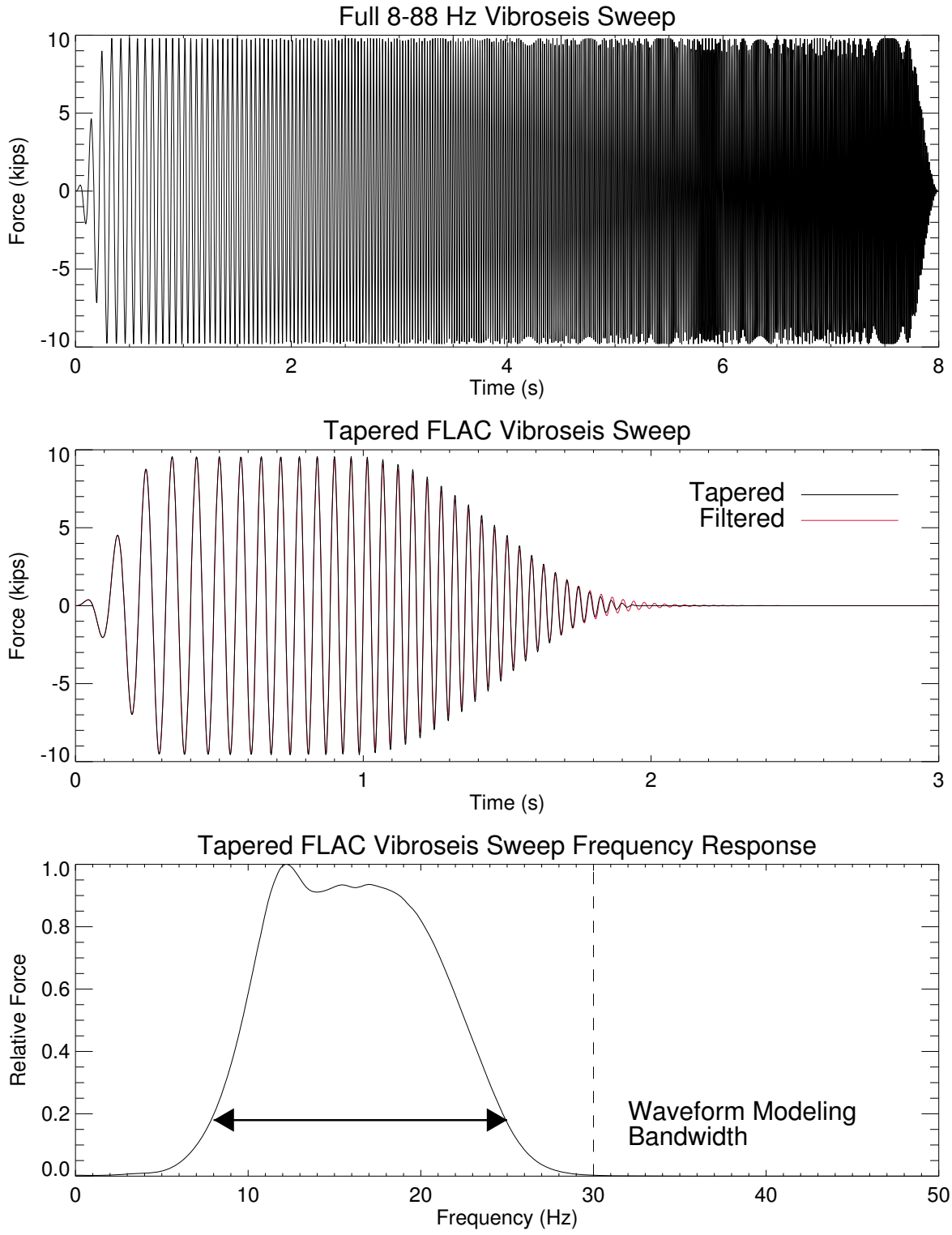

VIBROSEIS SWEEP, TAPERED SWEEP, AND TAPERED SWEEP FREQUENCY RESPONSE
Update of the 3−D Velocity Model for the DCPP Foundation Area
San Luis Obispo, California

FIGURE 3.3−1

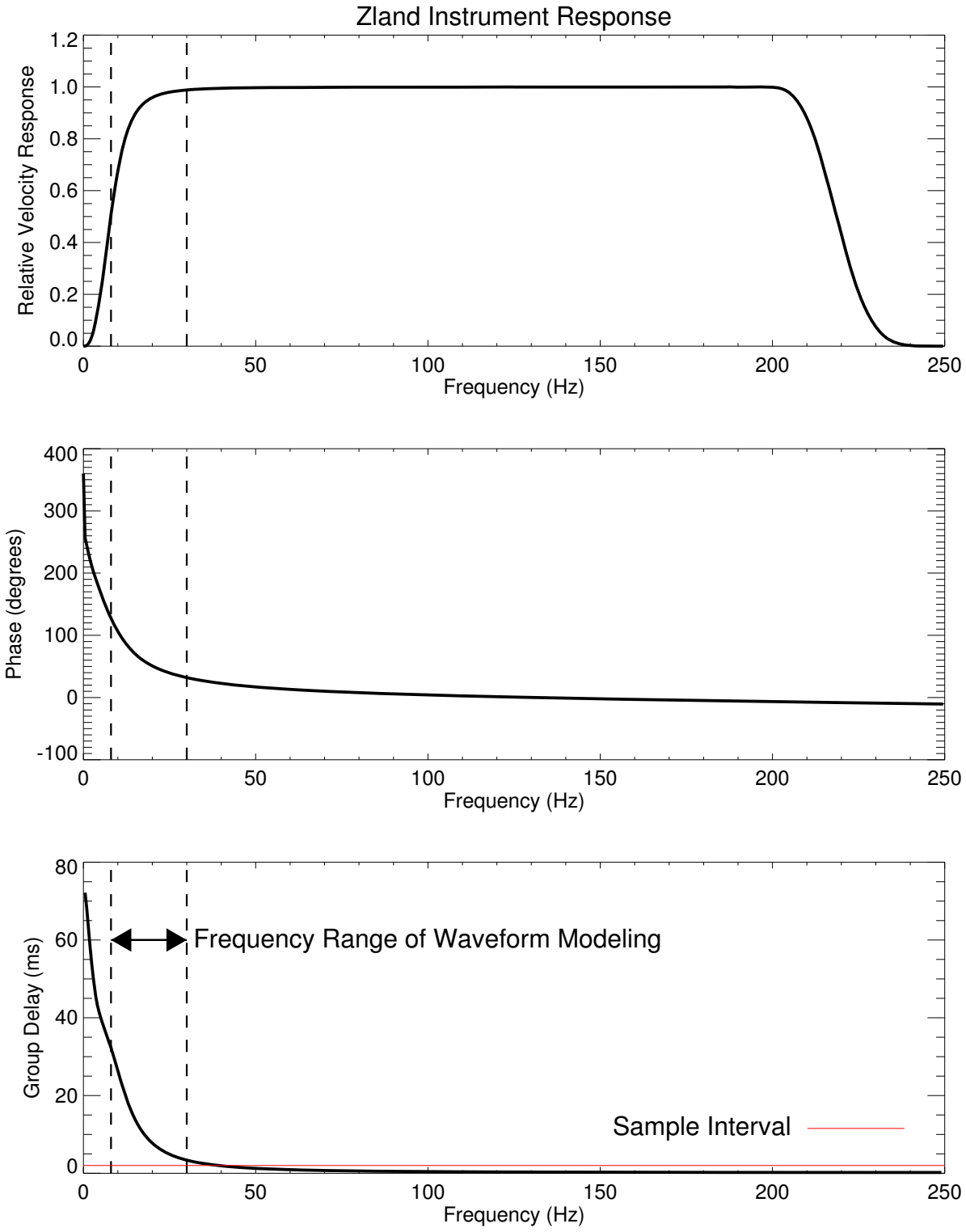

ZLAND AMPLITUDE, PHASE, AND GROUP DELAY RESPONSES
Update of the 3−D Velocity Model for the DCPP Foundation Area
San Luis Obispo, California

FIGURE 3.3−2

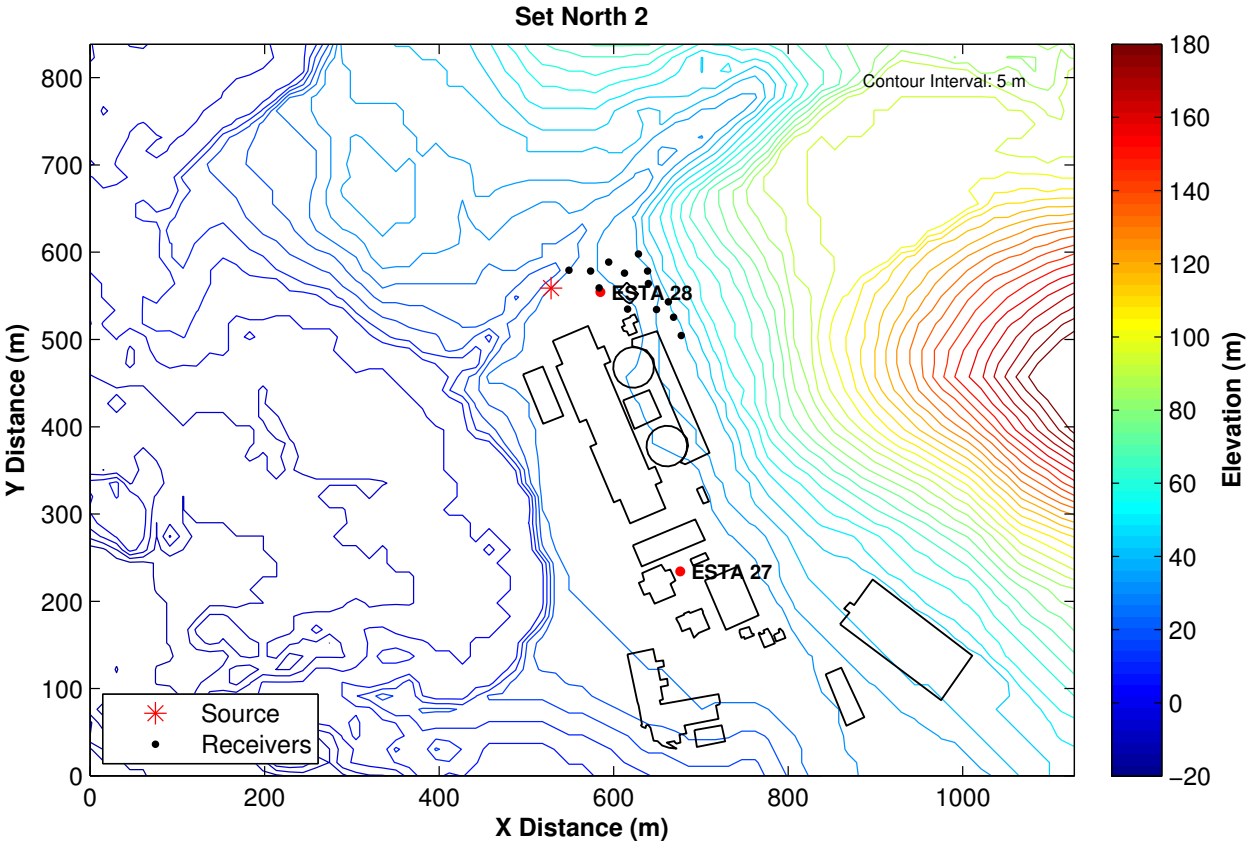

SET NORTH 2, SOURCE AT EASTING: 1739993.30, NORTHING: 693706.54
Update of the 3−D Velocity Model for the DCPP Foundation Area
San Luis Obispo, California

FIGURE 3.3−3

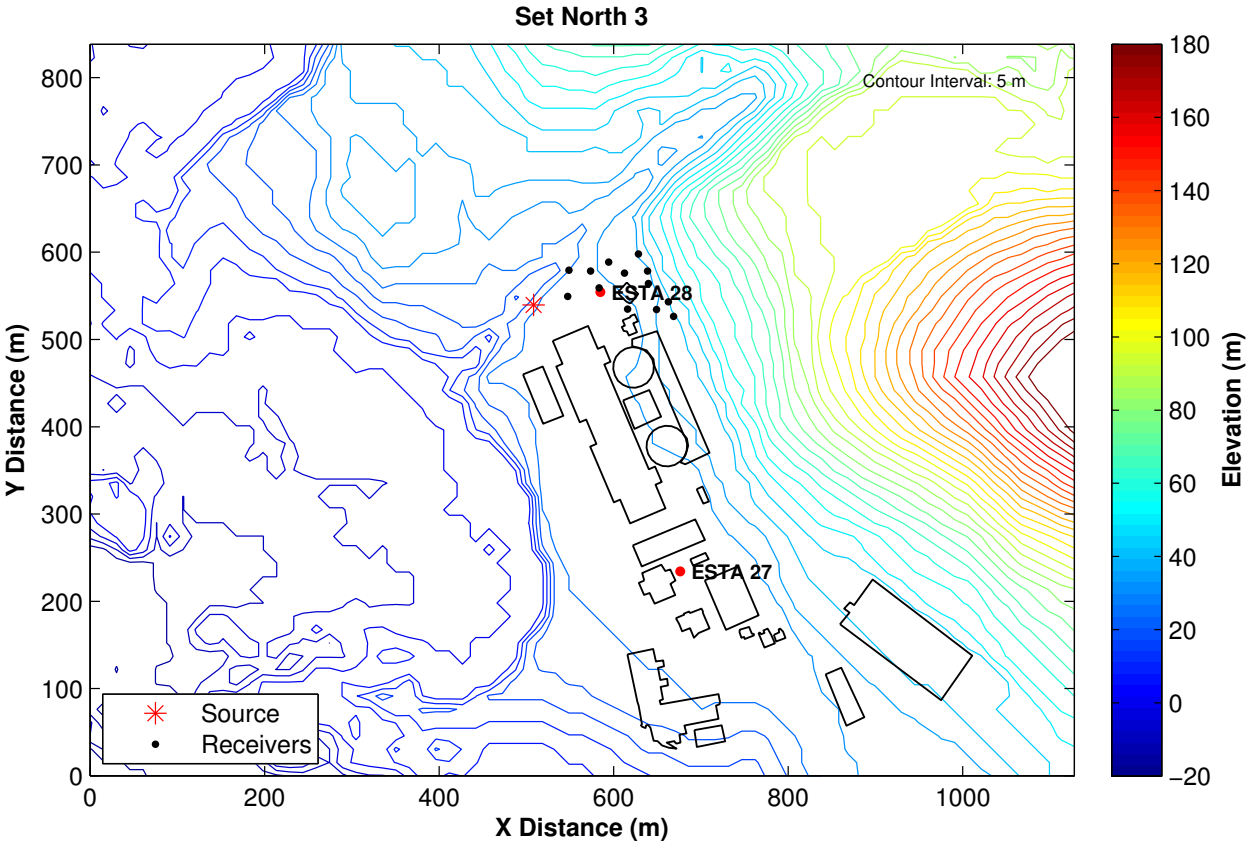

SET NORTH 3, SOURCE AT EASTING: 1739973.30, NORTHING: 693687.11
Update of the 3−D Velocity Model for the DCPP Foundation Area
San Luis Obispo, California

FIGURE 3.3−4

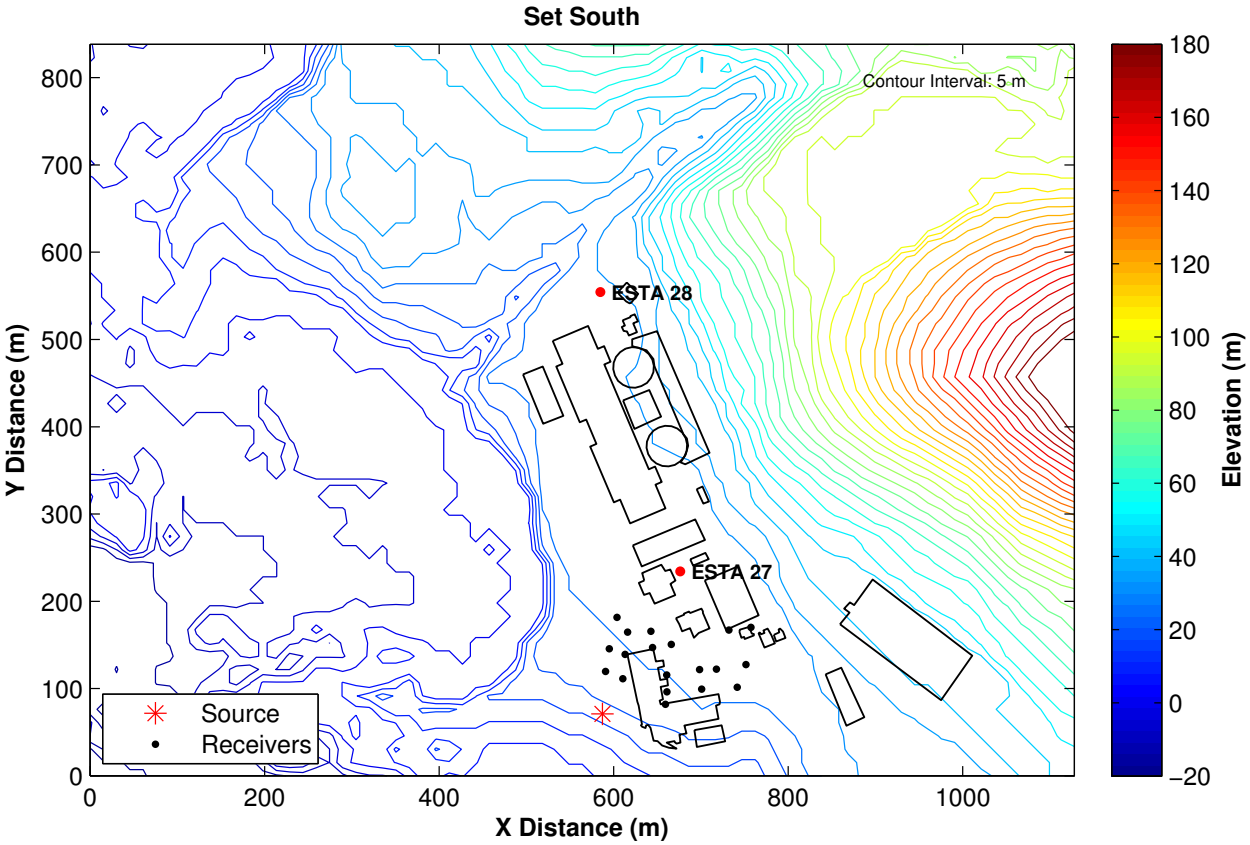

SET SOUTH 1, SOURCE AT EASTING: 1740052.30, NORTHING: 693218.73
Update of the 3−D Velocity Model for the DCPP Foundation Area
San Luis Obispo, California

FIGURE 3.3−5

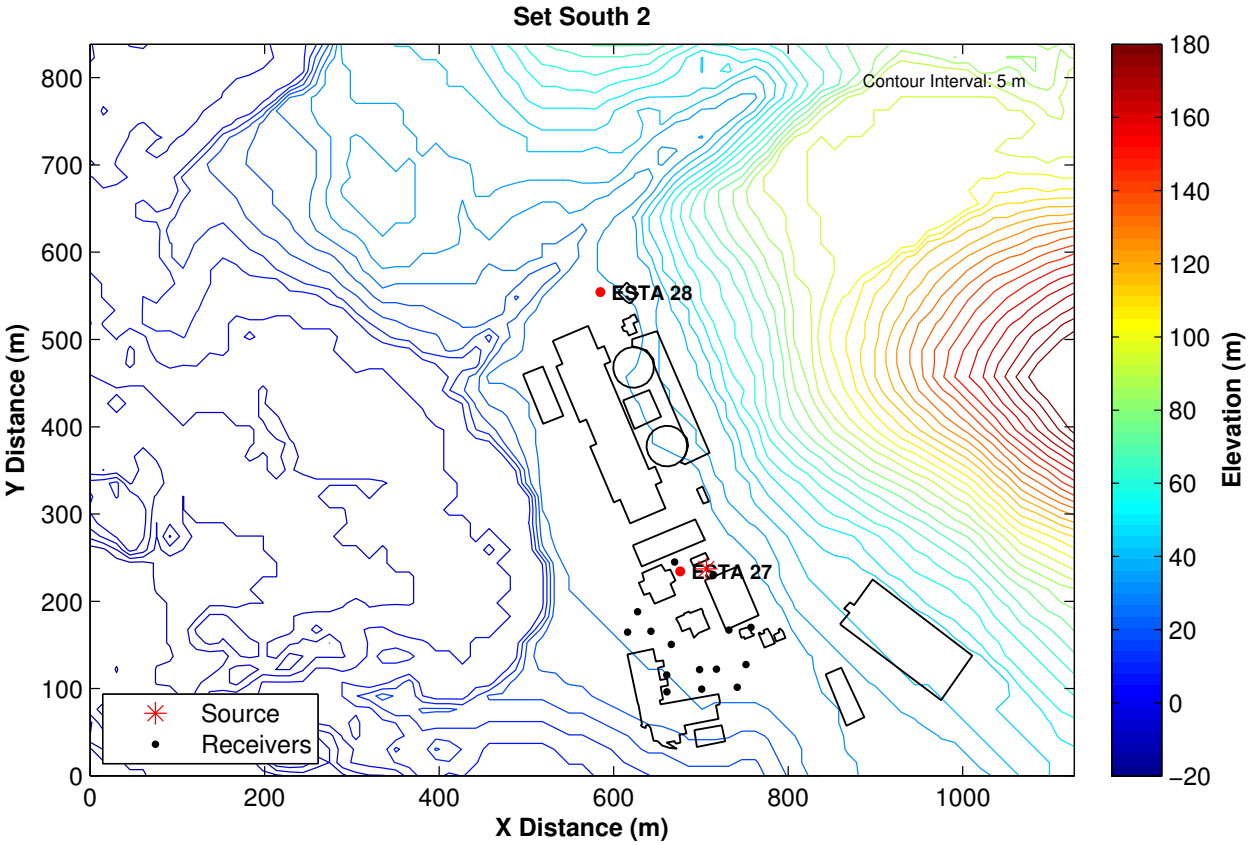

SET SOUTH 2, SOURCE AT EASTING: 1740171.40, NORTHING: 693384.77
Update of the 3−D Velocity Model for the DCPP Foundation Area
San Luis Obispo, California

FIGURE 3.3−6

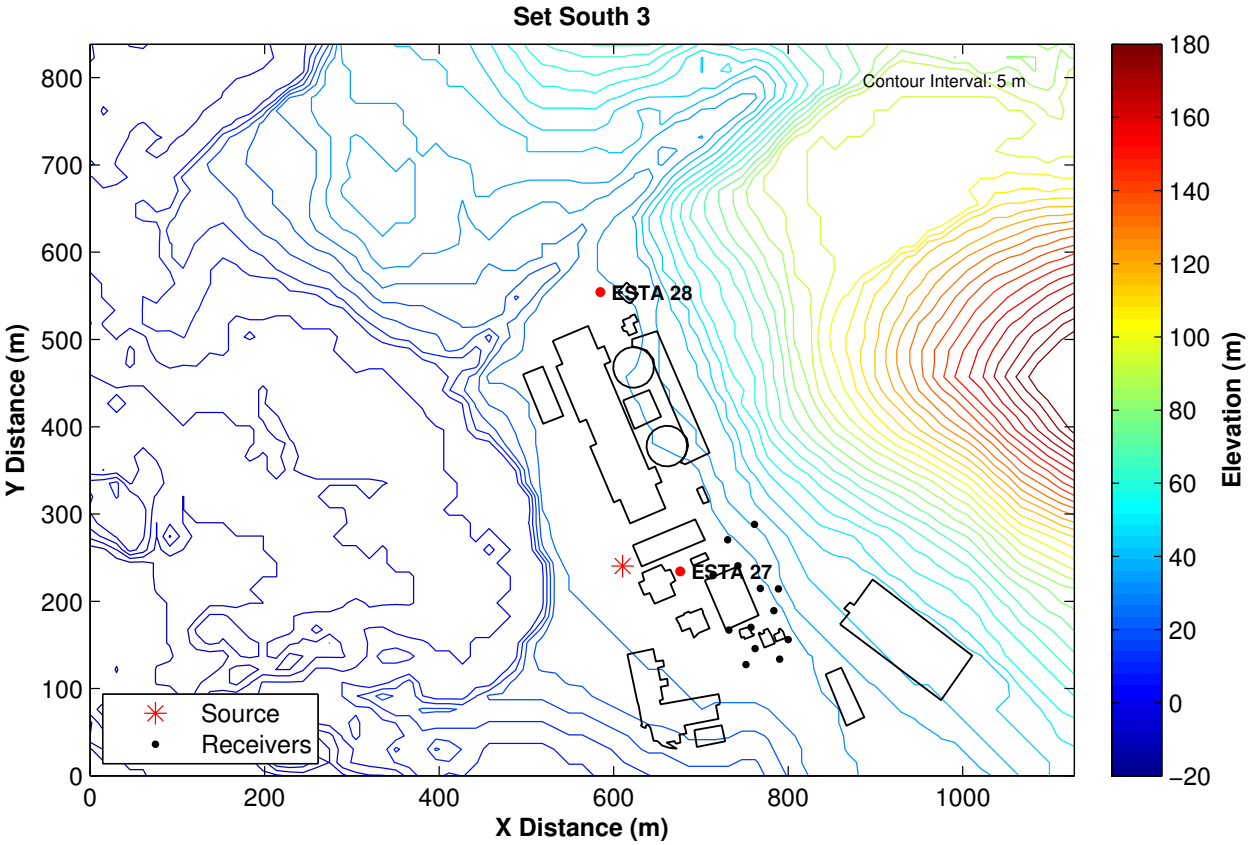

SET SOUTH 3, SOURCE AT EASTING: 1740075.30, NORTHING: 693388.18
Update of the 3−D Velocity Model for the DCPP Foundation Area
San Luis Obispo, California

FIGURE 3.3−7

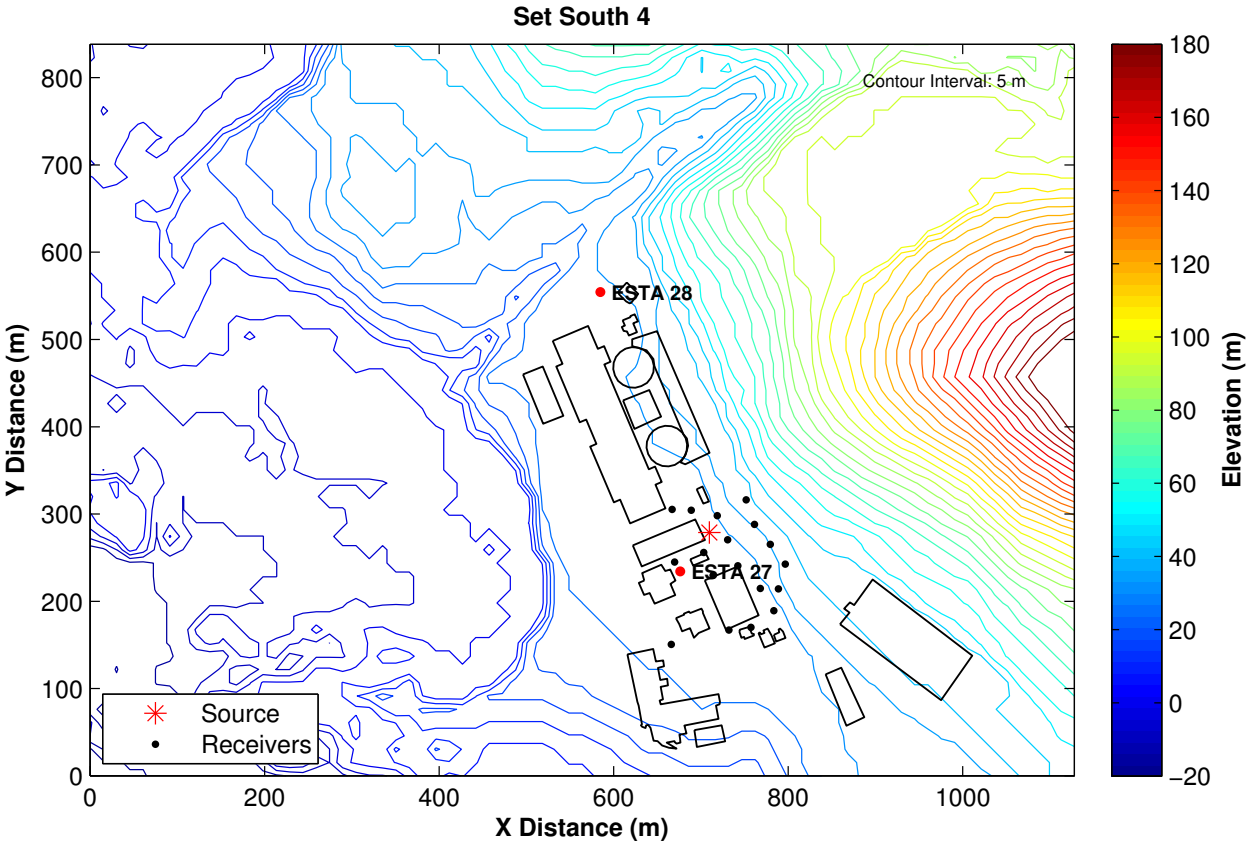

SET SOUTH 4, SOURCE AT EASTING: 1740174.80, NORTHING: 693426.45
Update of the 3−D Velocity Model for the DCPP Foundation Area
San Luis Obispo, California

FIGURE 3.3−8

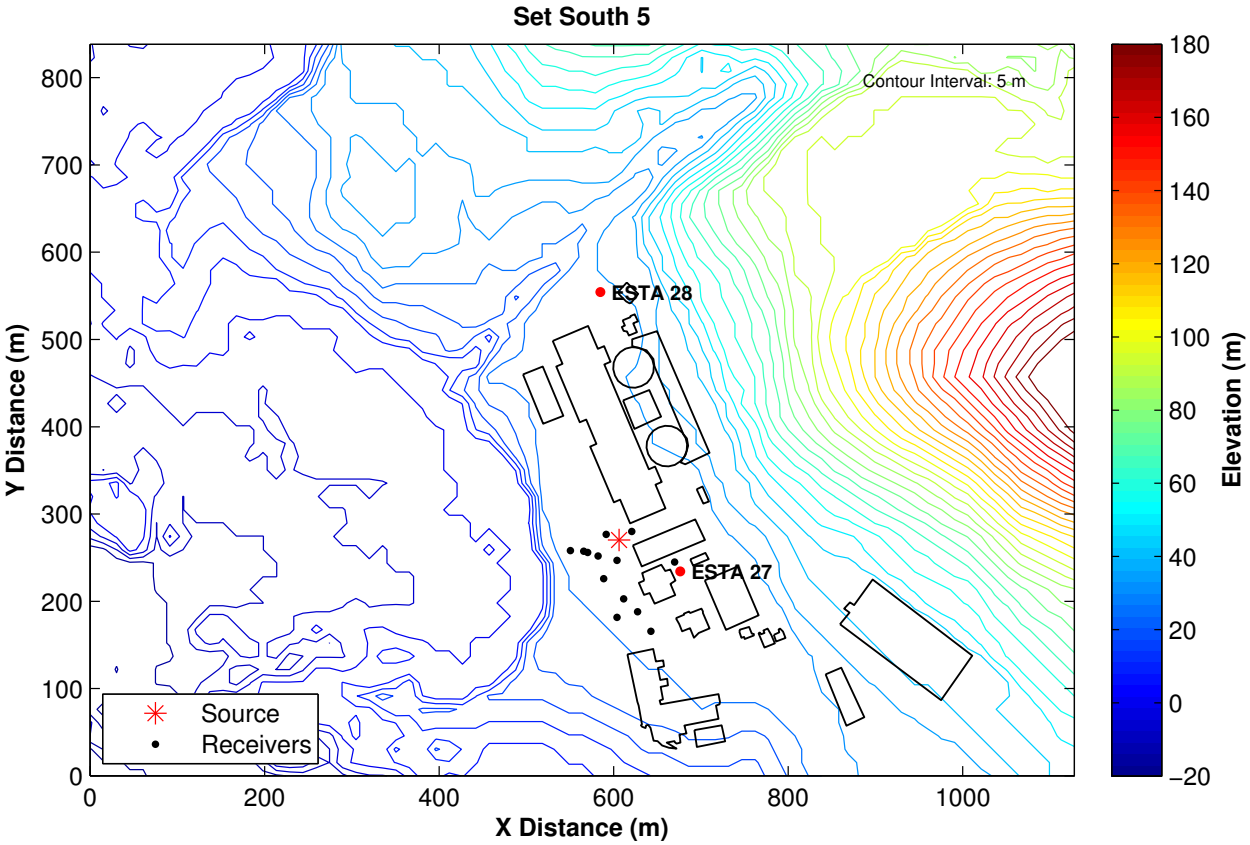

SET SOUTH 5, SOURCE AT EASTING: 1740071.40, NORTHING: 693417.91
Update of the 3−D Velocity Model for the DCPP Foundation Area
San Luis Obispo, California

FIGURE 3.3−9

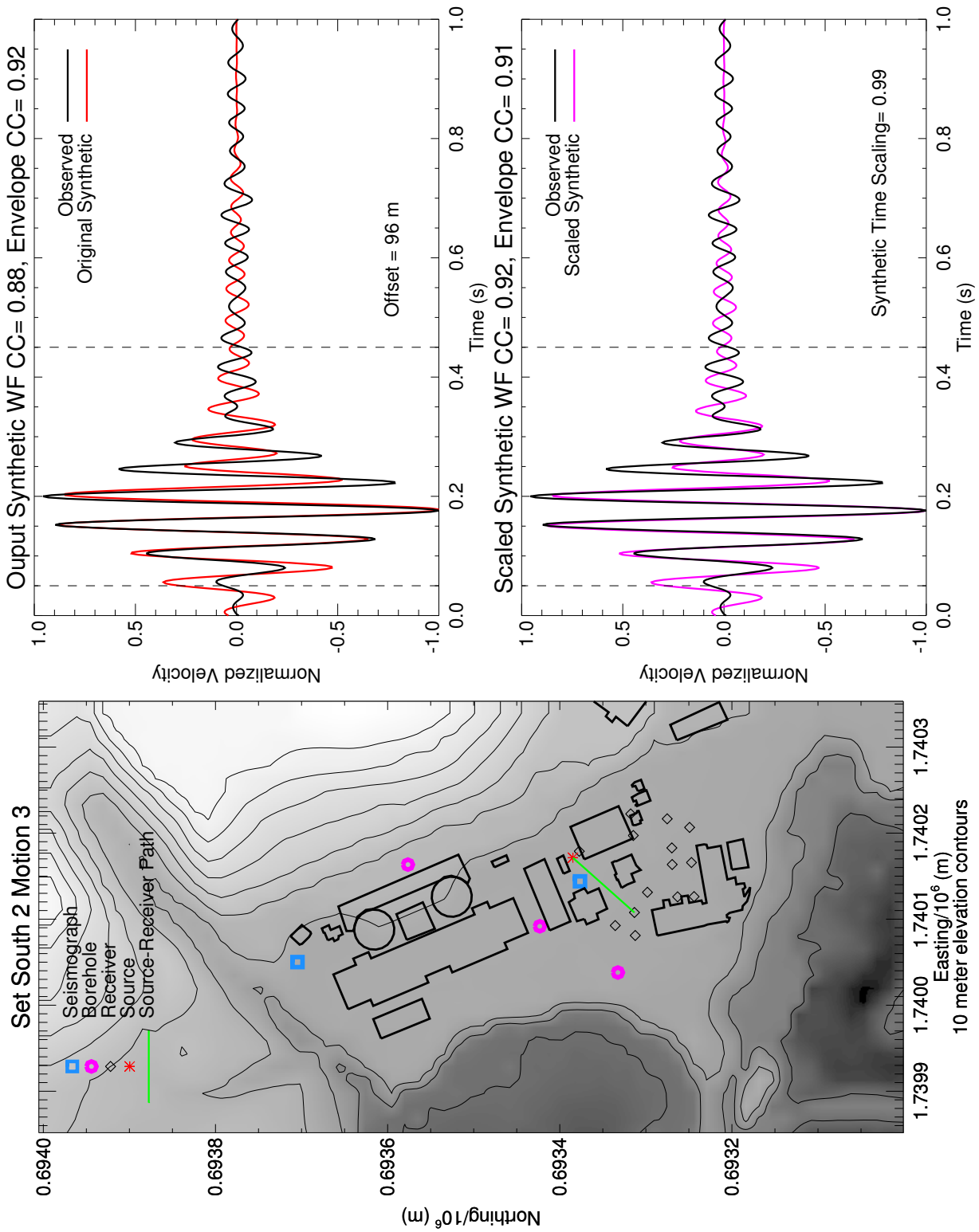

SET SOUTH 2 MOTION 3 CROSS−CORRELATION ANALYSIS
Update of the 3−D Velocity Model for the DCPP Foundation Area
San Luis Obispo, California

FIGURE 3.3−10

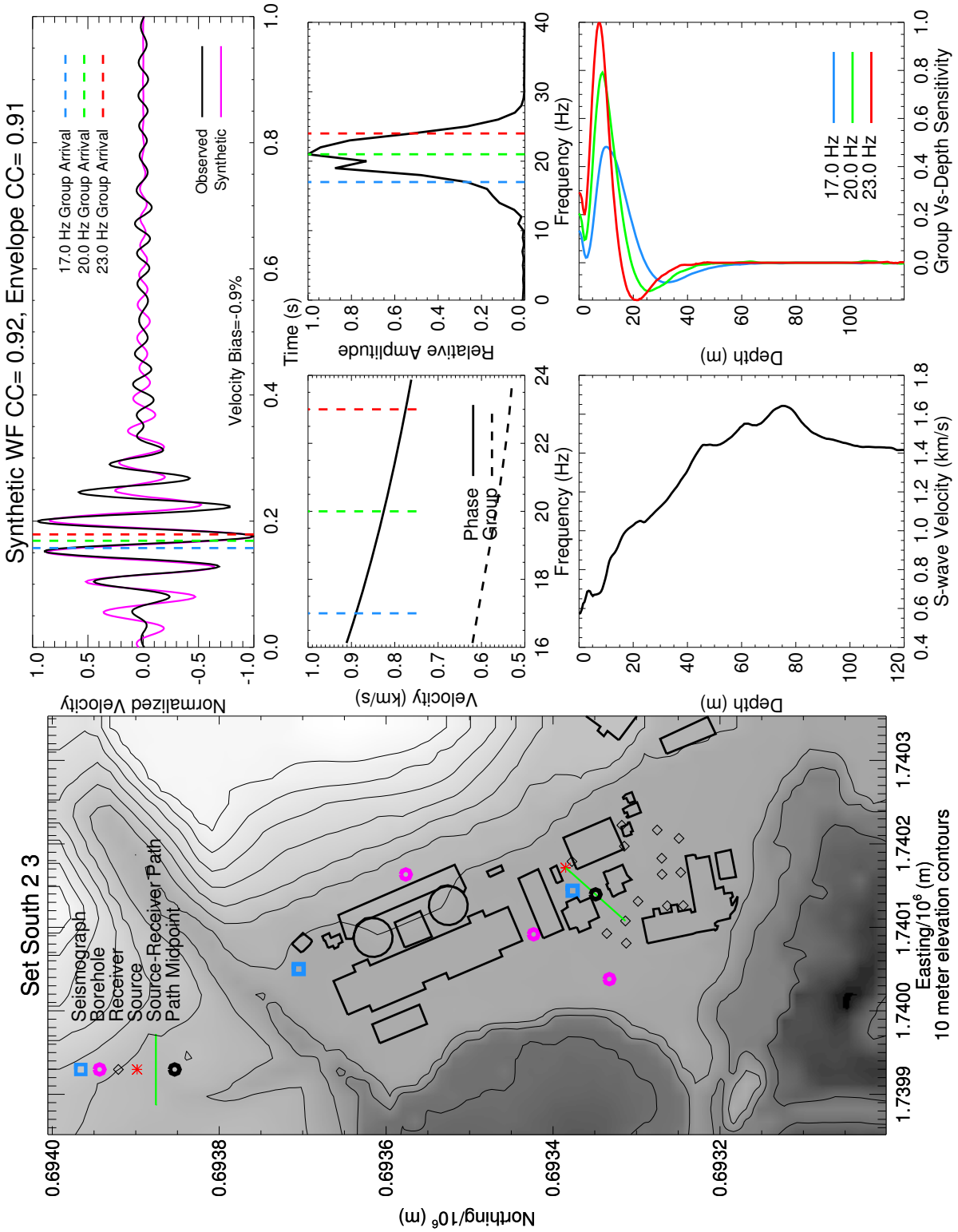

SET SOUTH 2 MOTION 3 SENSITIVITY ANALYSIS
Update of the 3−D Velocity Model for the DCPP Foundation Area
San Luis Obispo, California

FIGURE 3.3−11

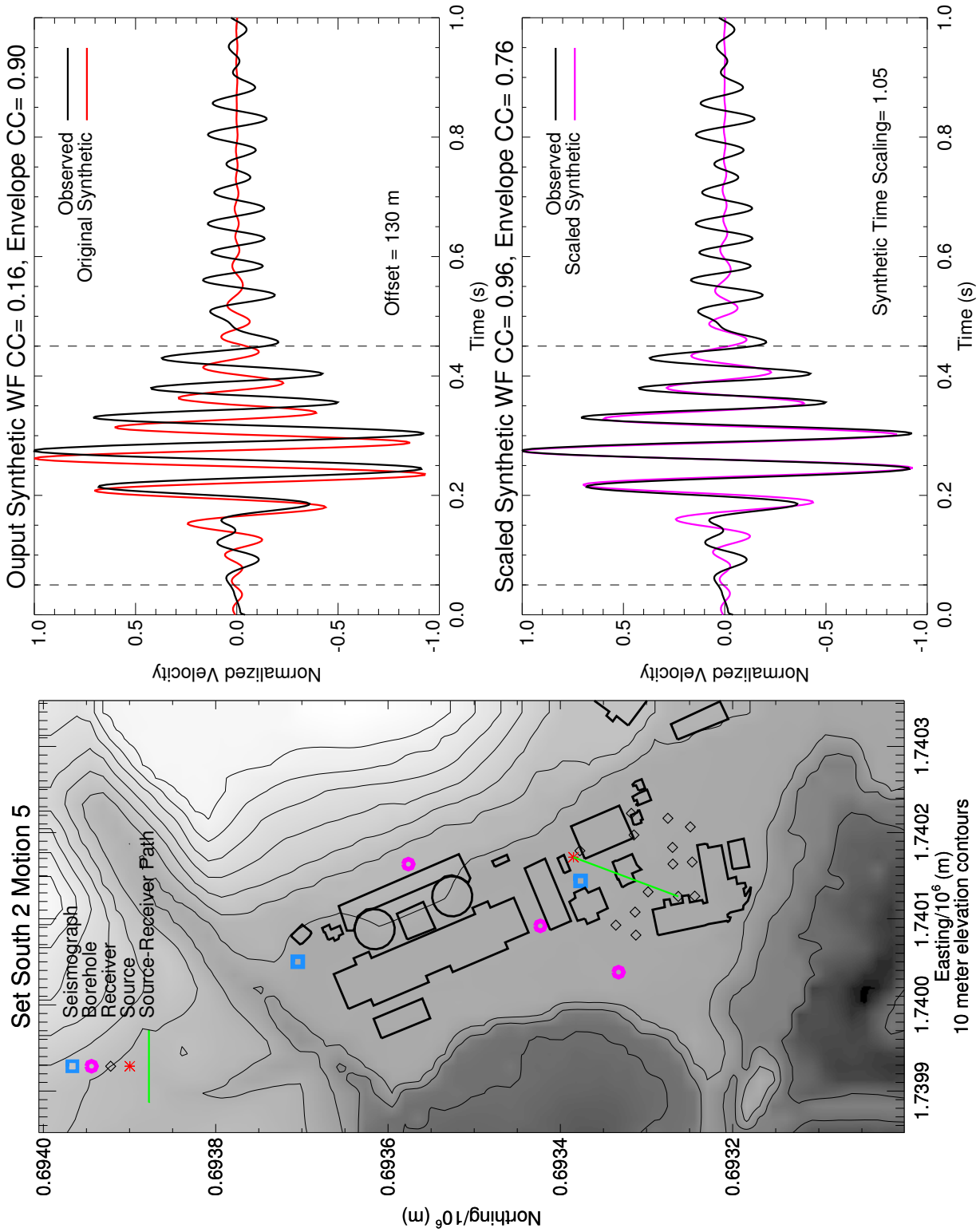

SET SOUTH 2 MOTION 5 CROSS−CORRELATION ANALYSIS
Update of the 3−D Velocity Model for the DCPP Foundation Area
San Luis Obispo, California

FIGURE 3.3−12

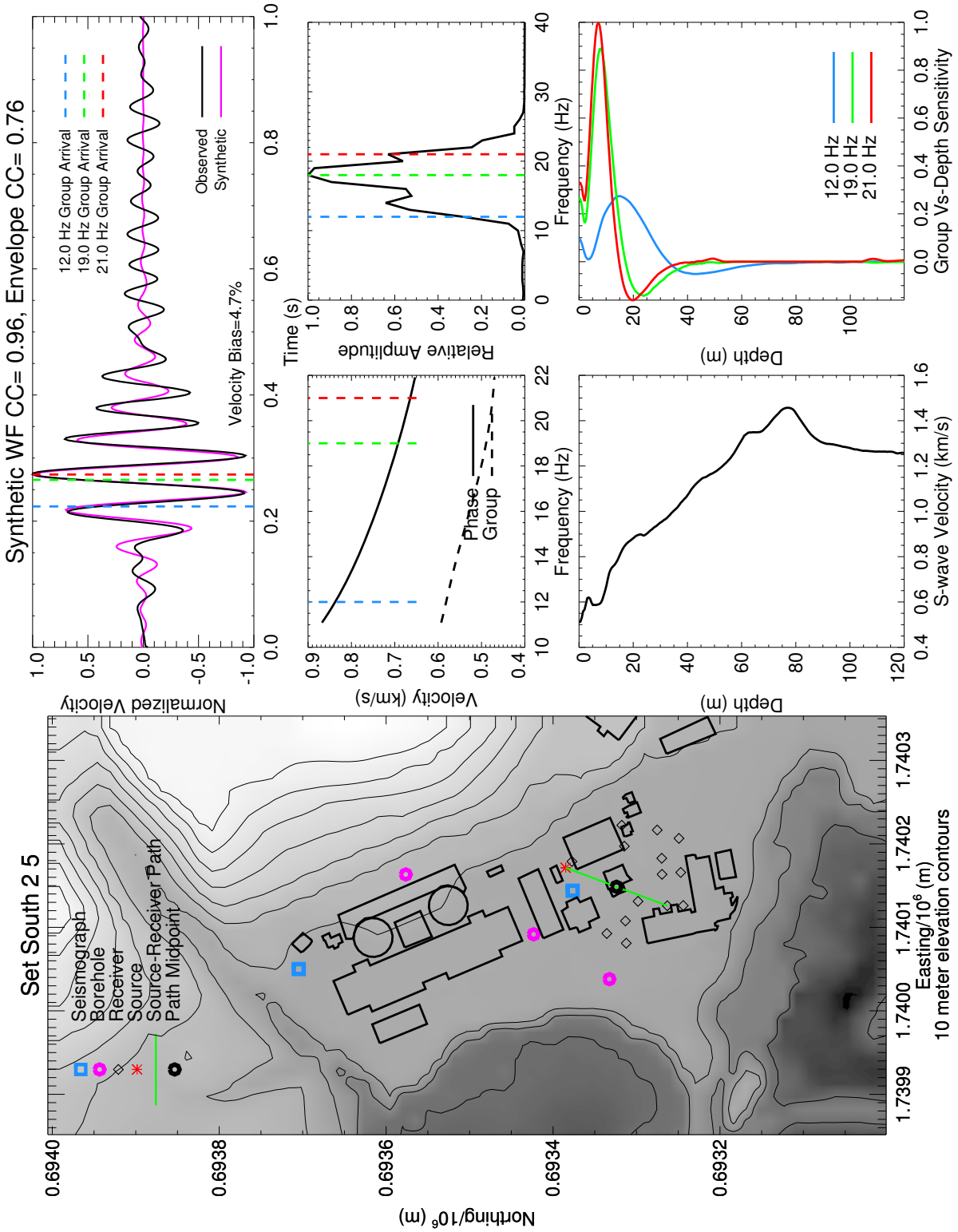

SET SOUTH 2 MOTION 5 SENSITIVITY ANALYSIS
Update of the 3−D Velocity Model for the DCPP Foundation Area
San Luis Obispo, California

FIGURE 3.3−13

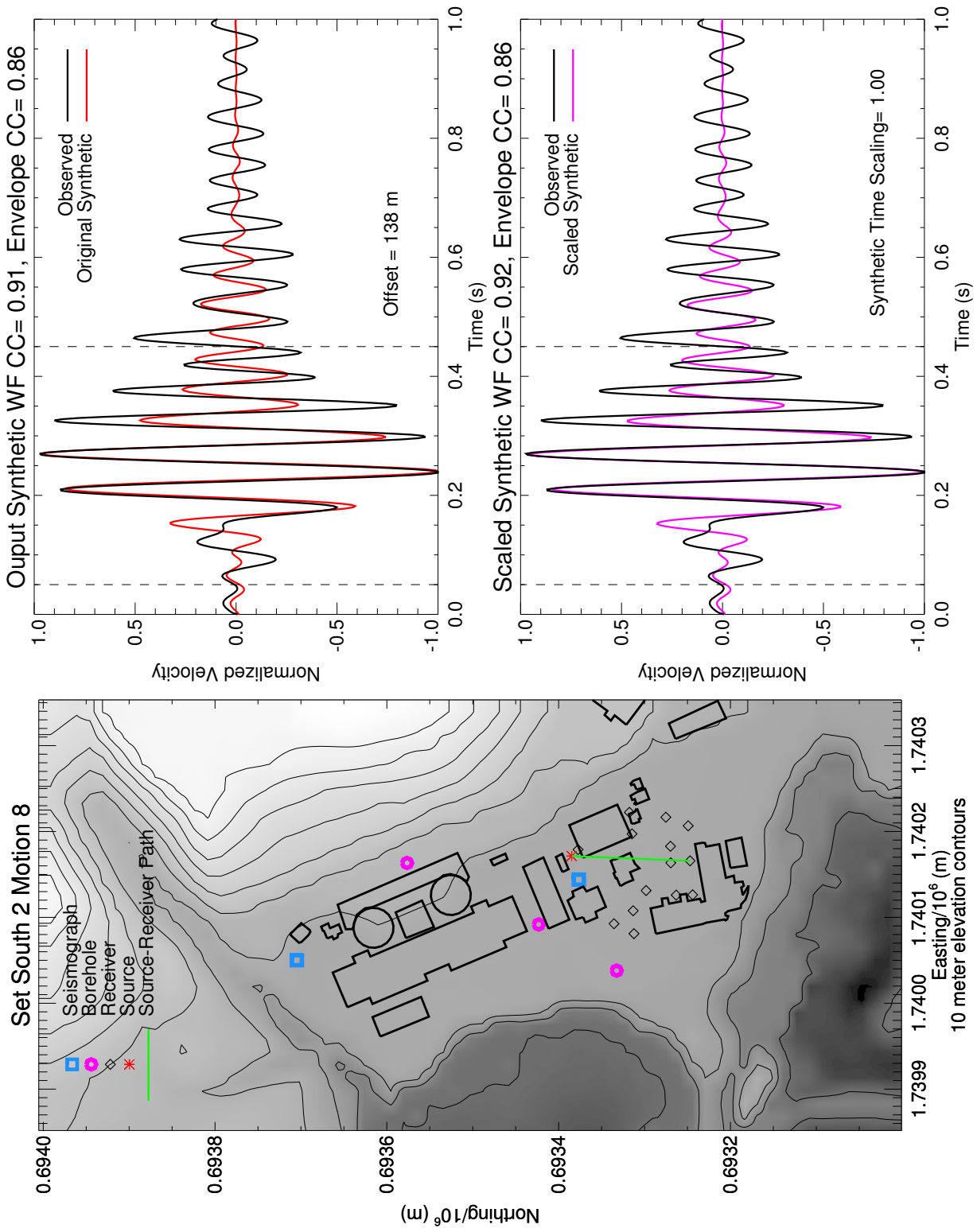

SET SOUTH 2 MOTION 8 CROSS−CORRELATION ANALYSIS
Update of the 3−D Velocity Model for the DCPP Foundation Area
San Luis Obispo, California

FIGURE 3.3−14

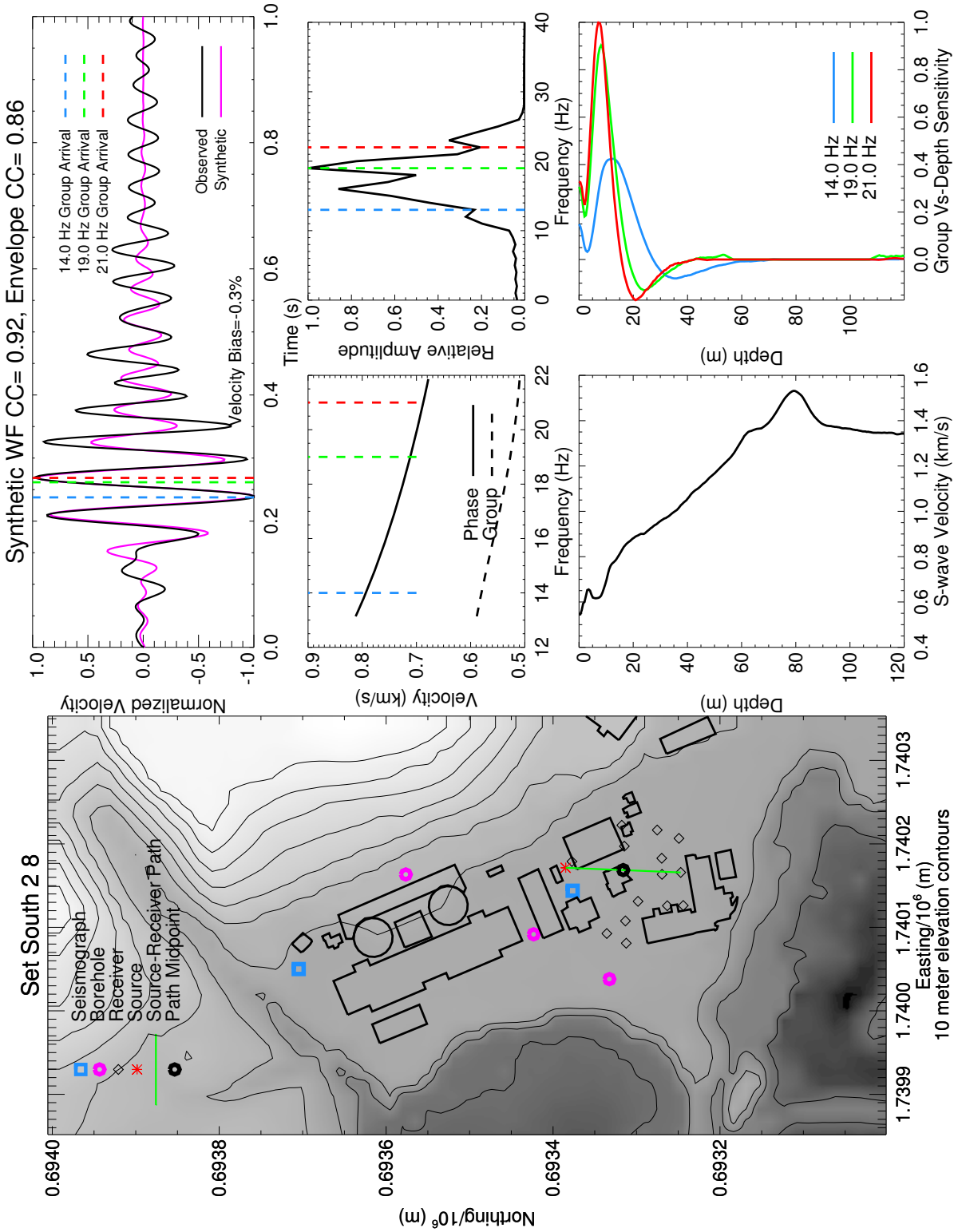

SET SOUTH 2 MOTION 8 SENSITIVITY ANALYSIS
Update of the 3−D Velocity Model for the DCPP Foundation Area
San Luis Obispo, California

FIGURE 3.3−15

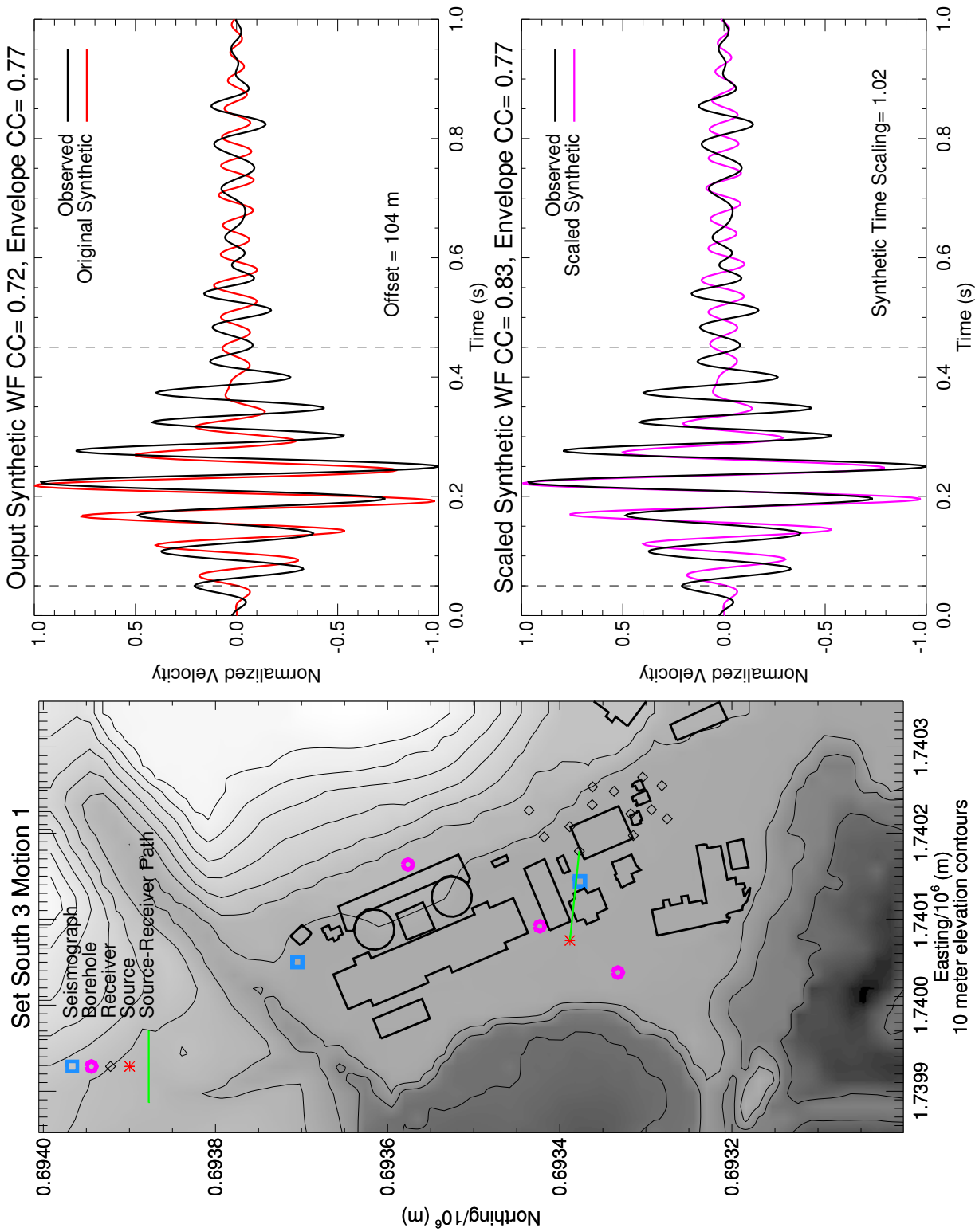

SET SOUTH 3 MOTION 1 CROSS−CORRELATION ANALYSIS
Update of the 3−D Velocity Model for the DCPP Foundation Area
San Luis Obispo, California

FIGURE 3.3−16

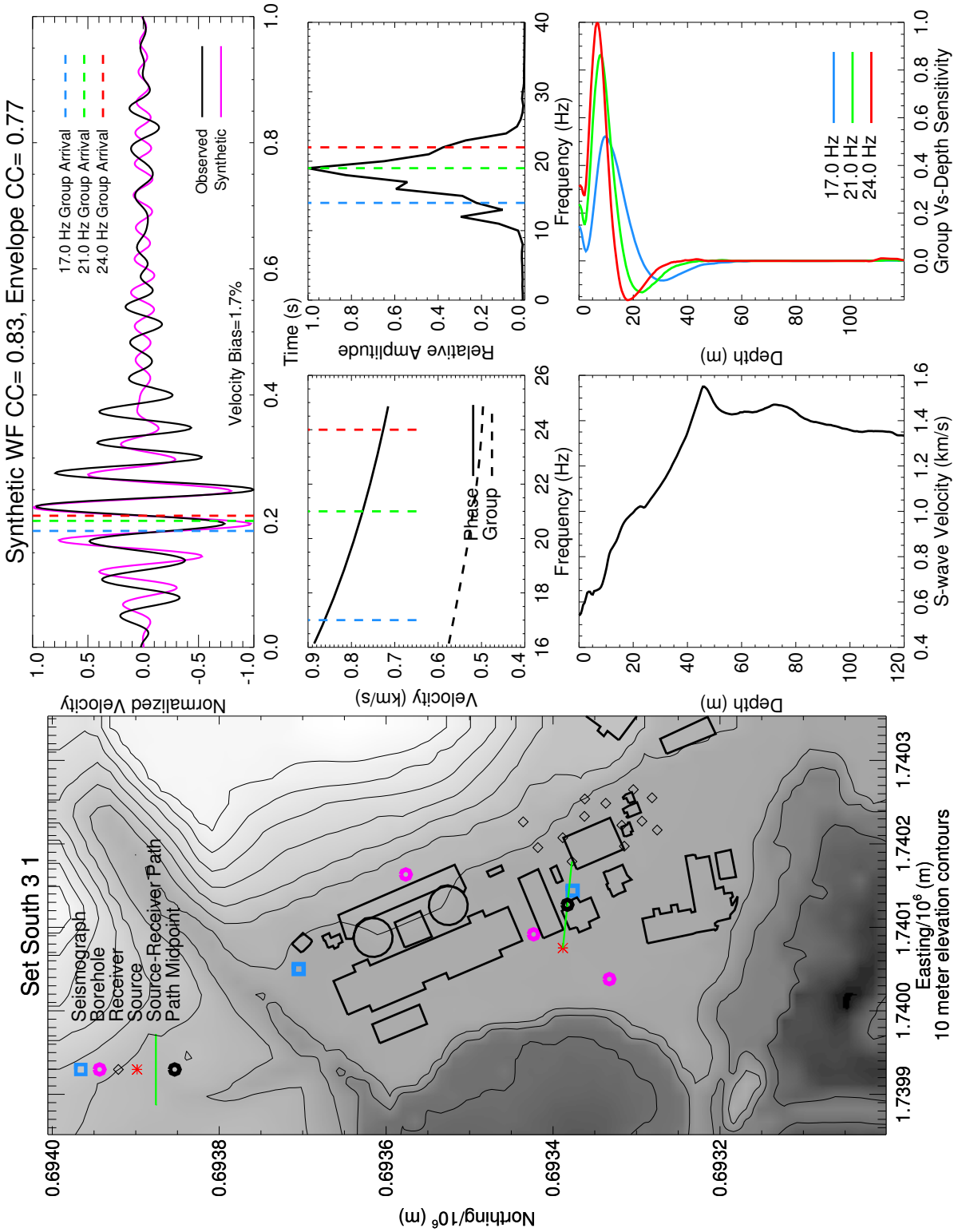

SET SOUTH 3 MOTION 1 SENSITIVITY ANALYSIS
Update of the 3−D Velocity Model for the DCPP Foundation Area
San Luis Obispo, California

FIGURE 3.3−17

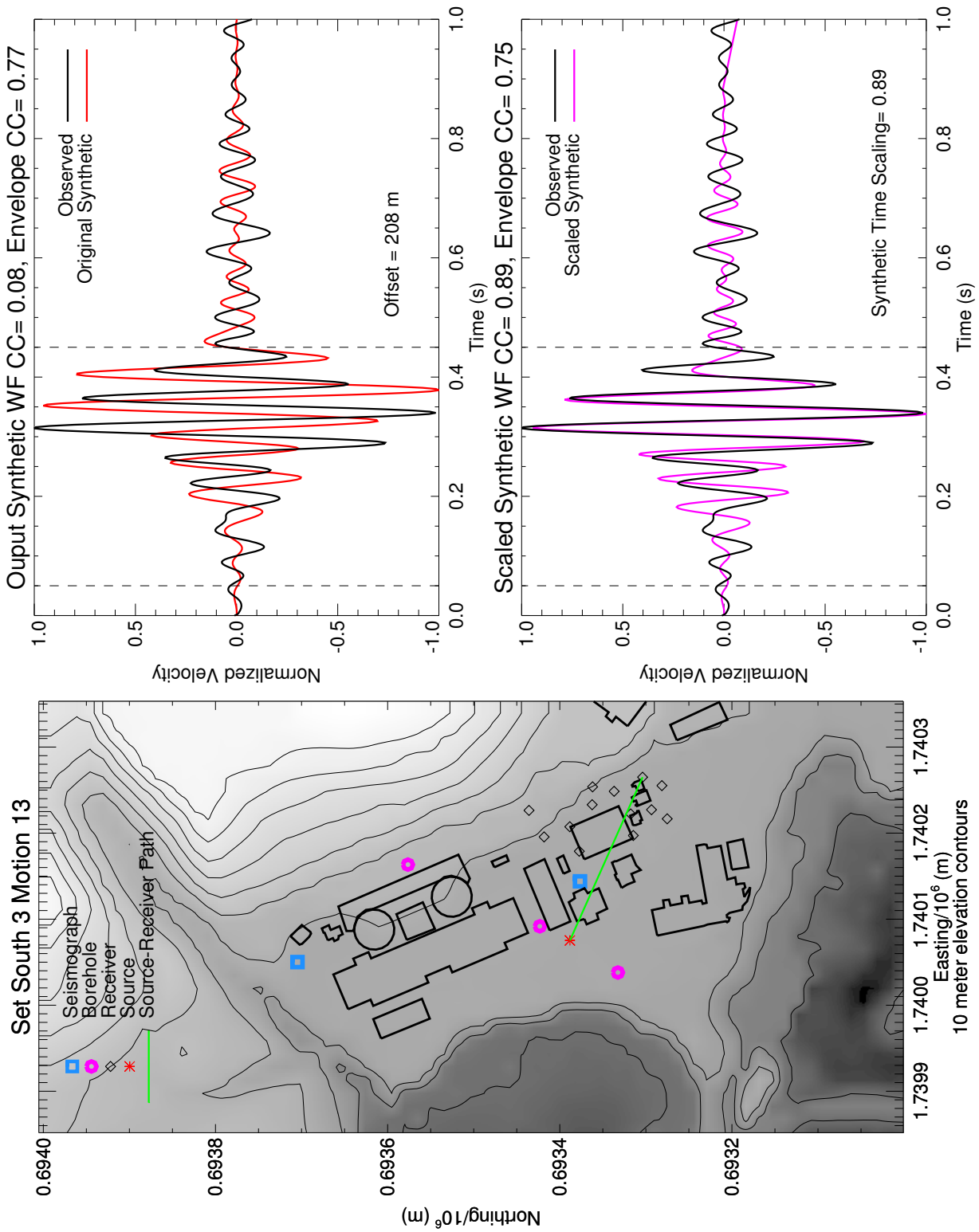

SET SOUTH 3 MOTION 13 CROSS−CORRELATION ANALYSIS
Update of the 3−D Velocity Model for the DCPP Foundation Area
San Luis Obispo, California

FIGURE 3.3−18

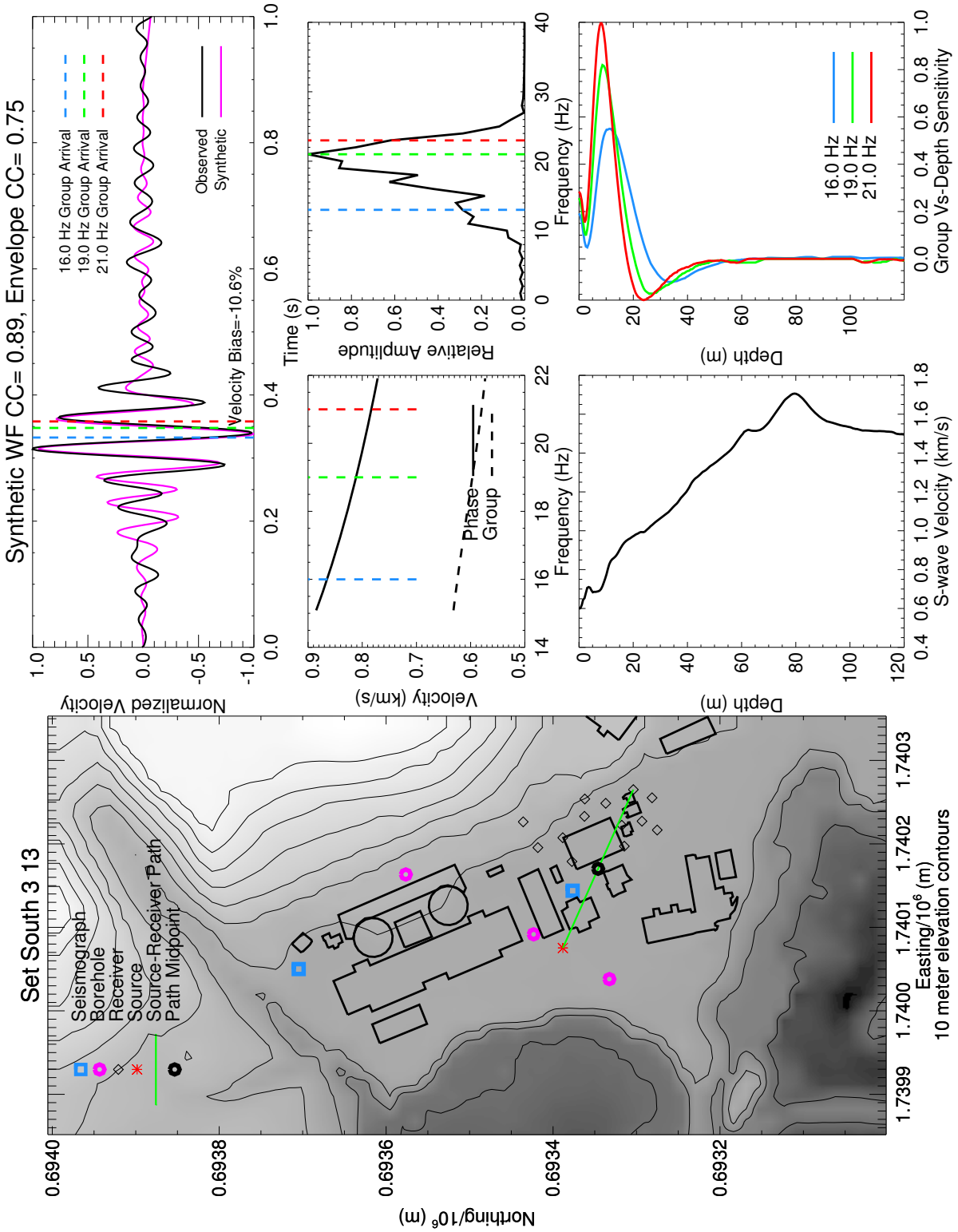

SET SOUTH 3 MOTION 13 SENSITIVITY ANALYSIS
Update of the 3−D Velocity Model for the DCPP Foundation Area
San Luis Obispo, California

FIGURE 3.3−19

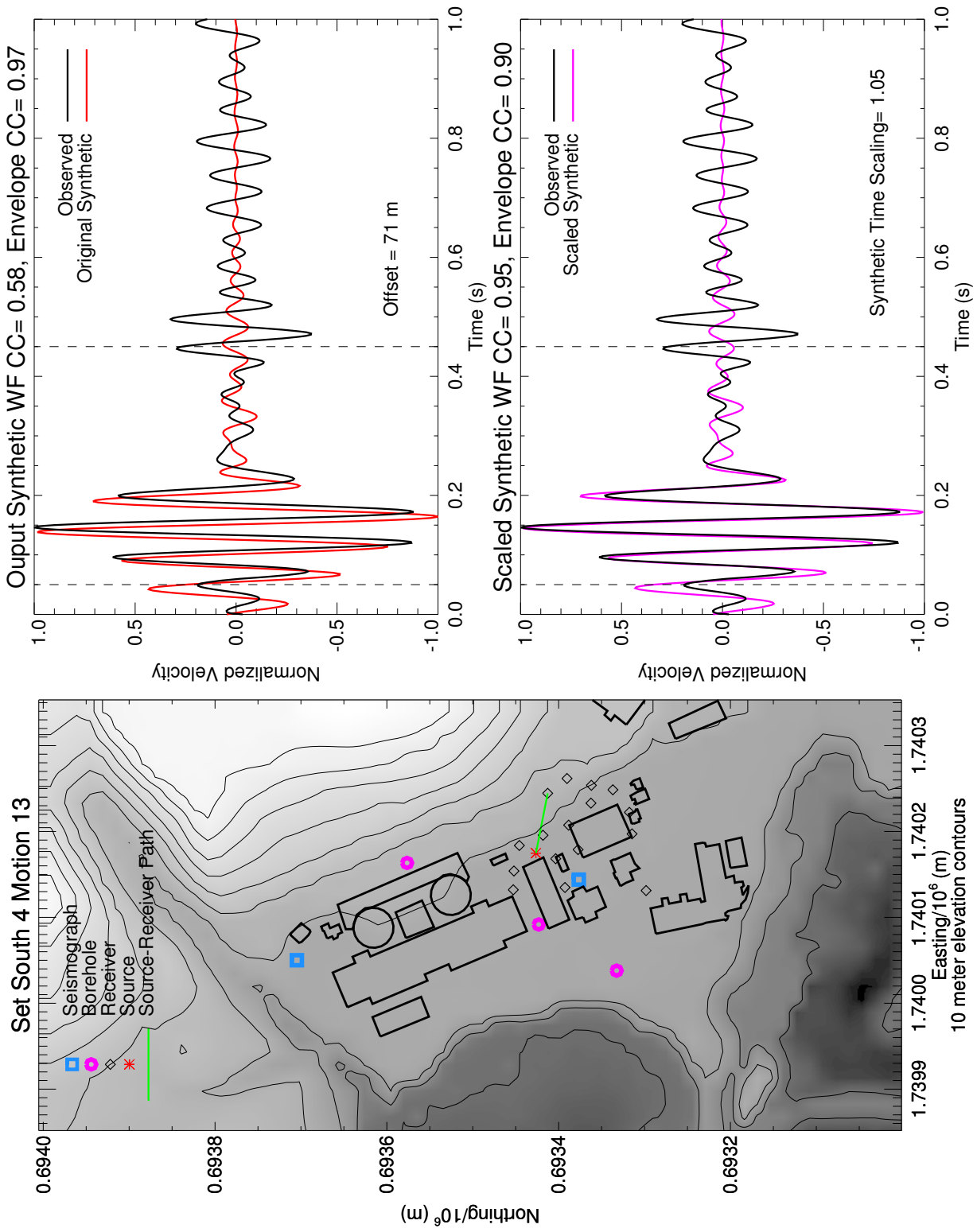

SET SOUTH 4 MOTION 13 CROSS−CORRELATION ANALYSIS
Update of the 3−D Velocity Model for the DCPP Foundation Area
San Luis Obispo, California

FIGURE 3.3−20

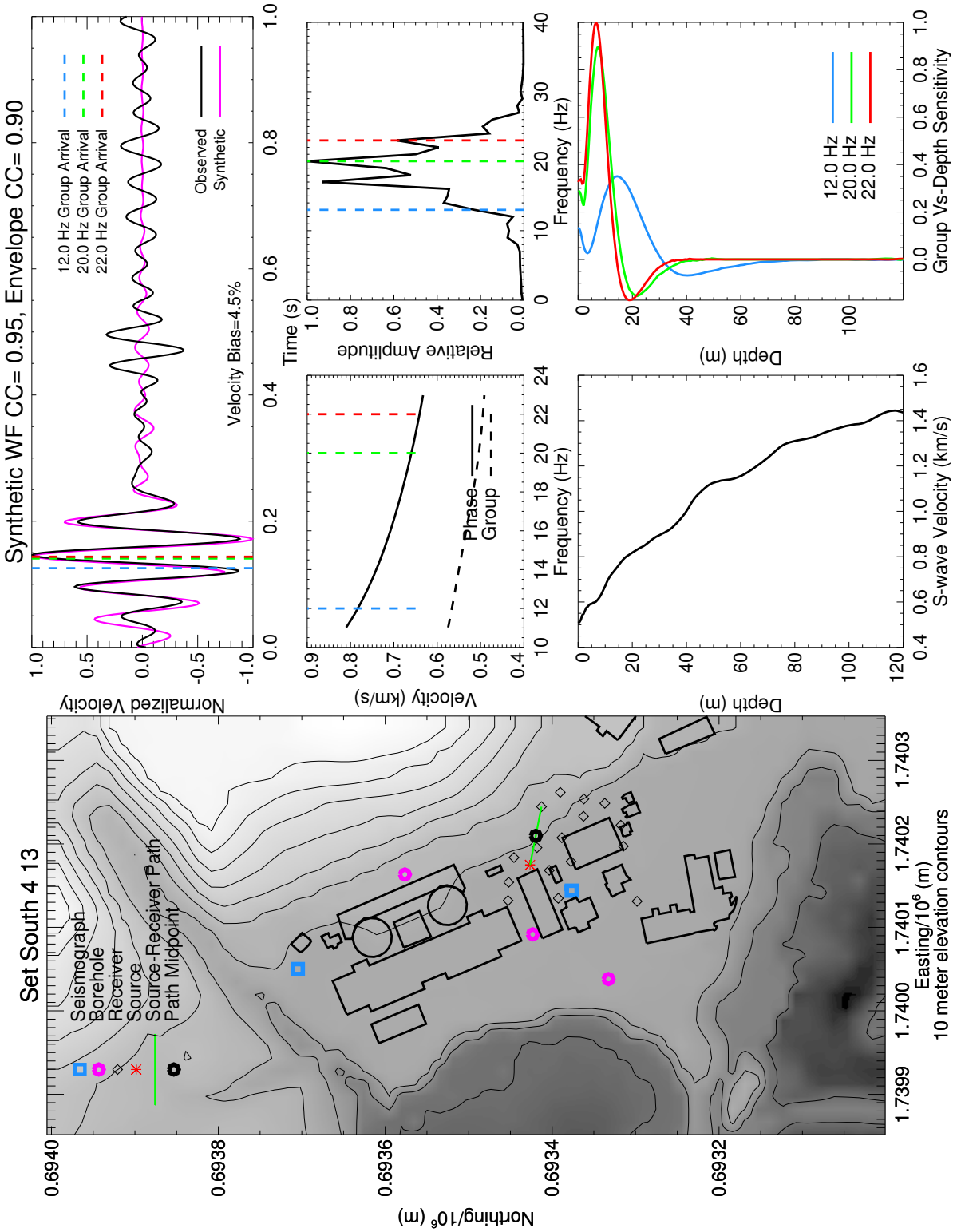

SET SOUTH 4 MOTION 13 SENSITIVITY ANALYSIS
Update of the 3−D Velocity Model for the DCPP Foundation Area
San Luis Obispo, California

FIGURE 3.3−21

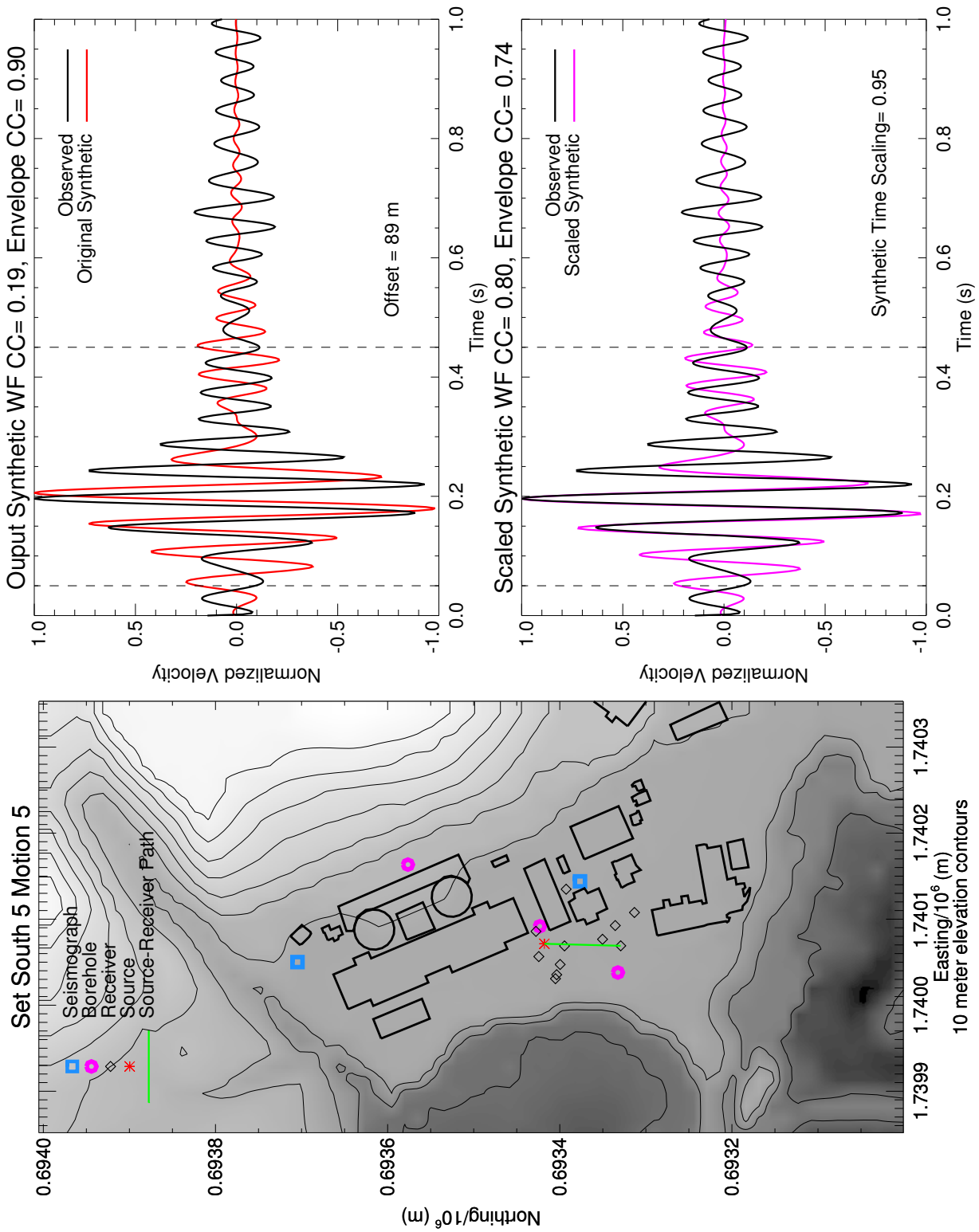

SET SOUTH 5 MOTION 5 CROSS−CORRELATION ANALYSIS
Update of the 3−D Velocity Model for the DCPP Foundation Area
San Luis Obispo, California

FIGURE 3.3−22

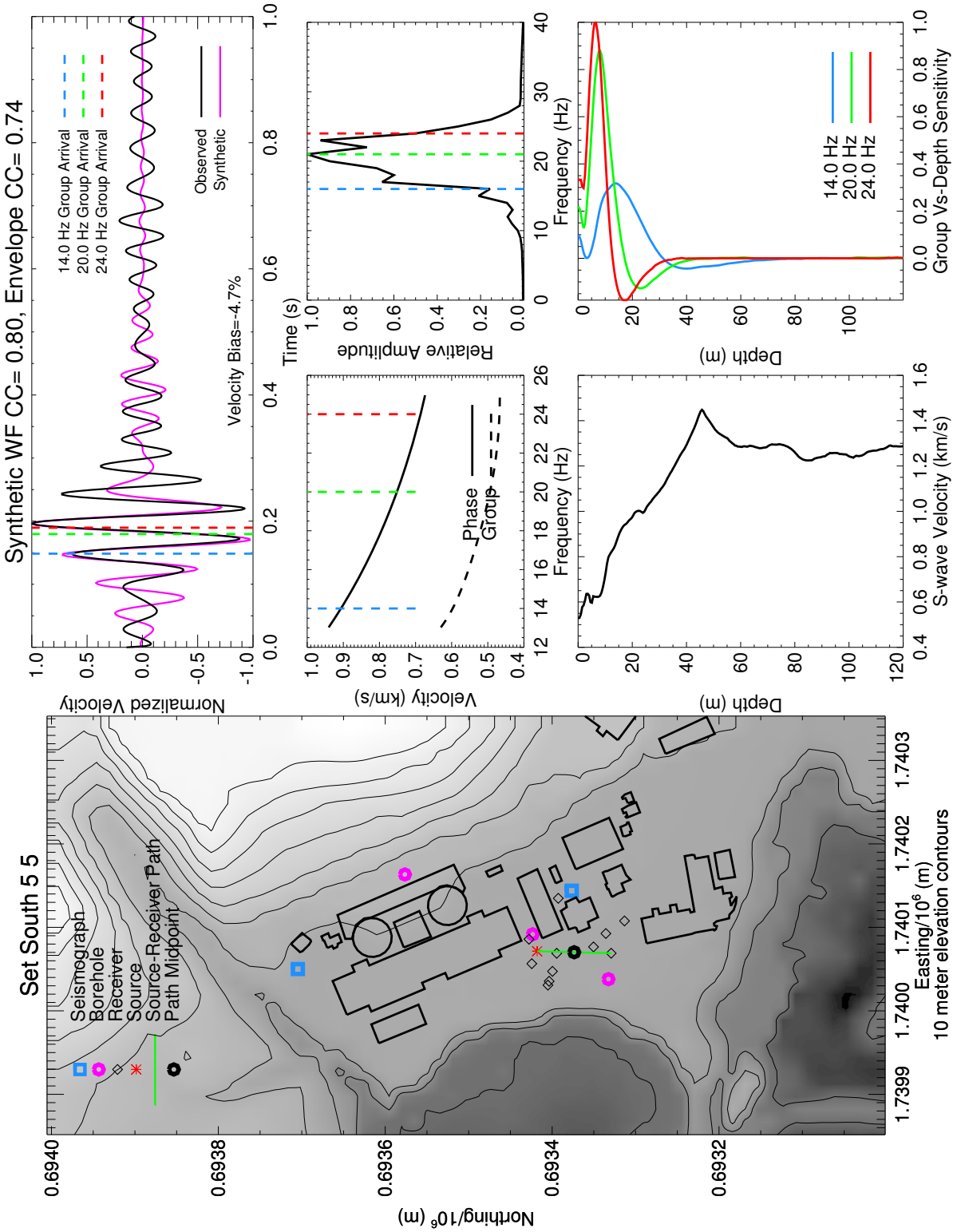

SET SOUTH 5 MOTION 5 SENSITIVITY ANALYSIS
Update of the 3−D Velocity Model for the DCPP Foundation Area
San Luis Obispo, California

FIGURE 3.3−23

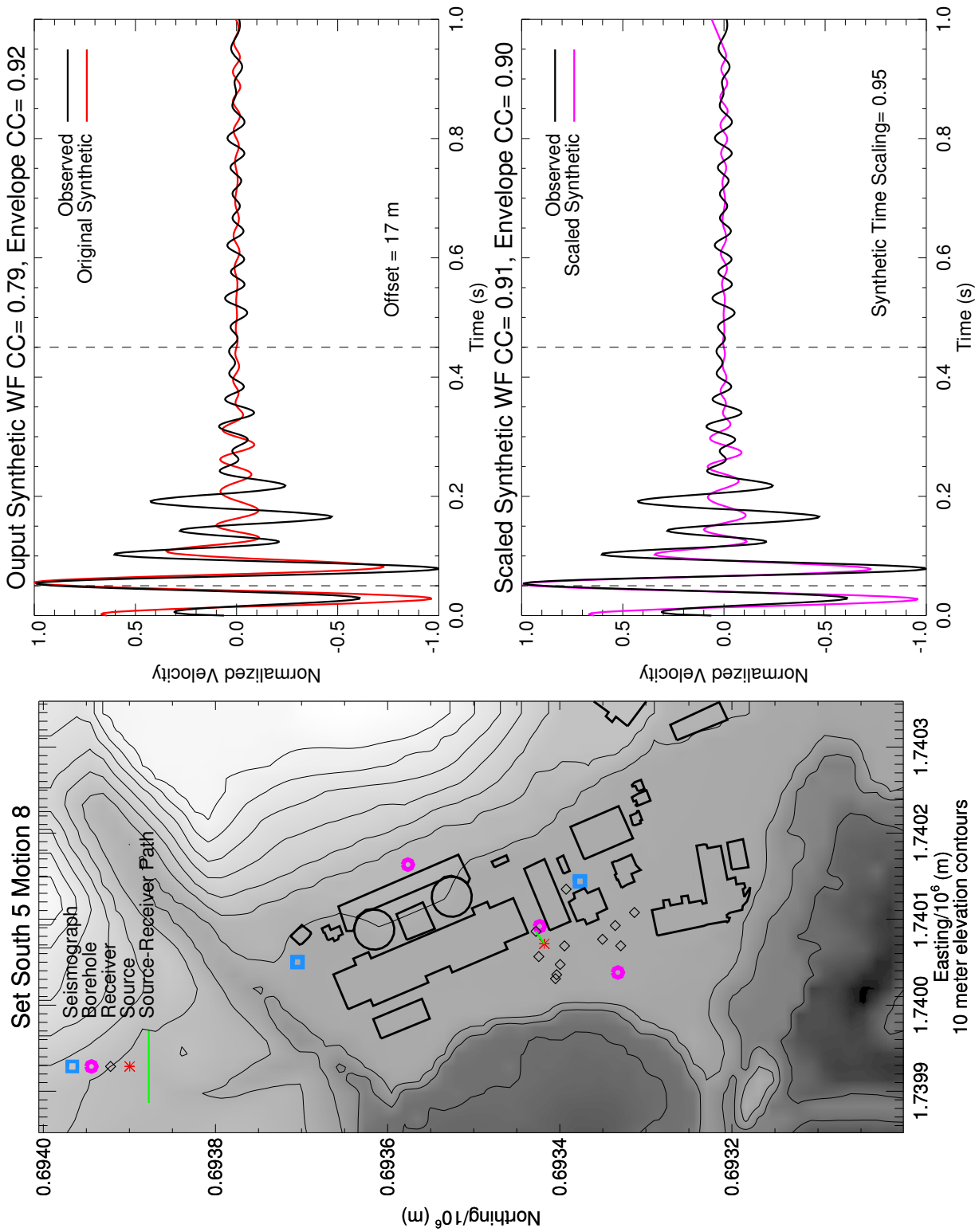

SET SOUTH 5 MOTION 8 CROSS−CORRELATION ANALYSIS
Update of the 3−D Velocity Model for the DCPP Foundation Area
San Luis Obispo, California

FIGURE 3.3−24

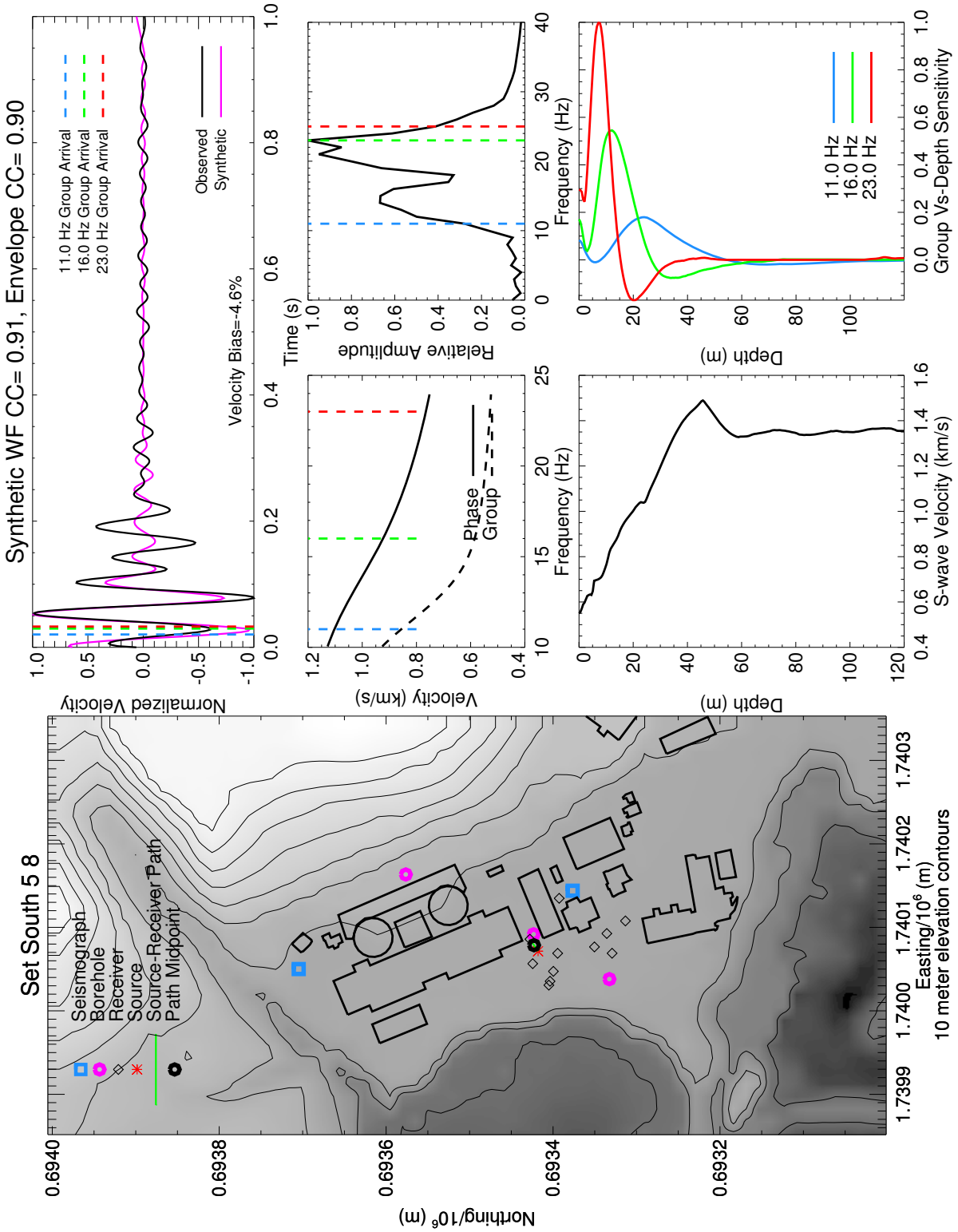

SET SOUTH 5 MOTION 8 SENSITIVITY ANALYSIS
Update of the 3−D Velocity Model for the DCPP Foundation Area
San Luis Obispo, California

FIGURE 3.3−25

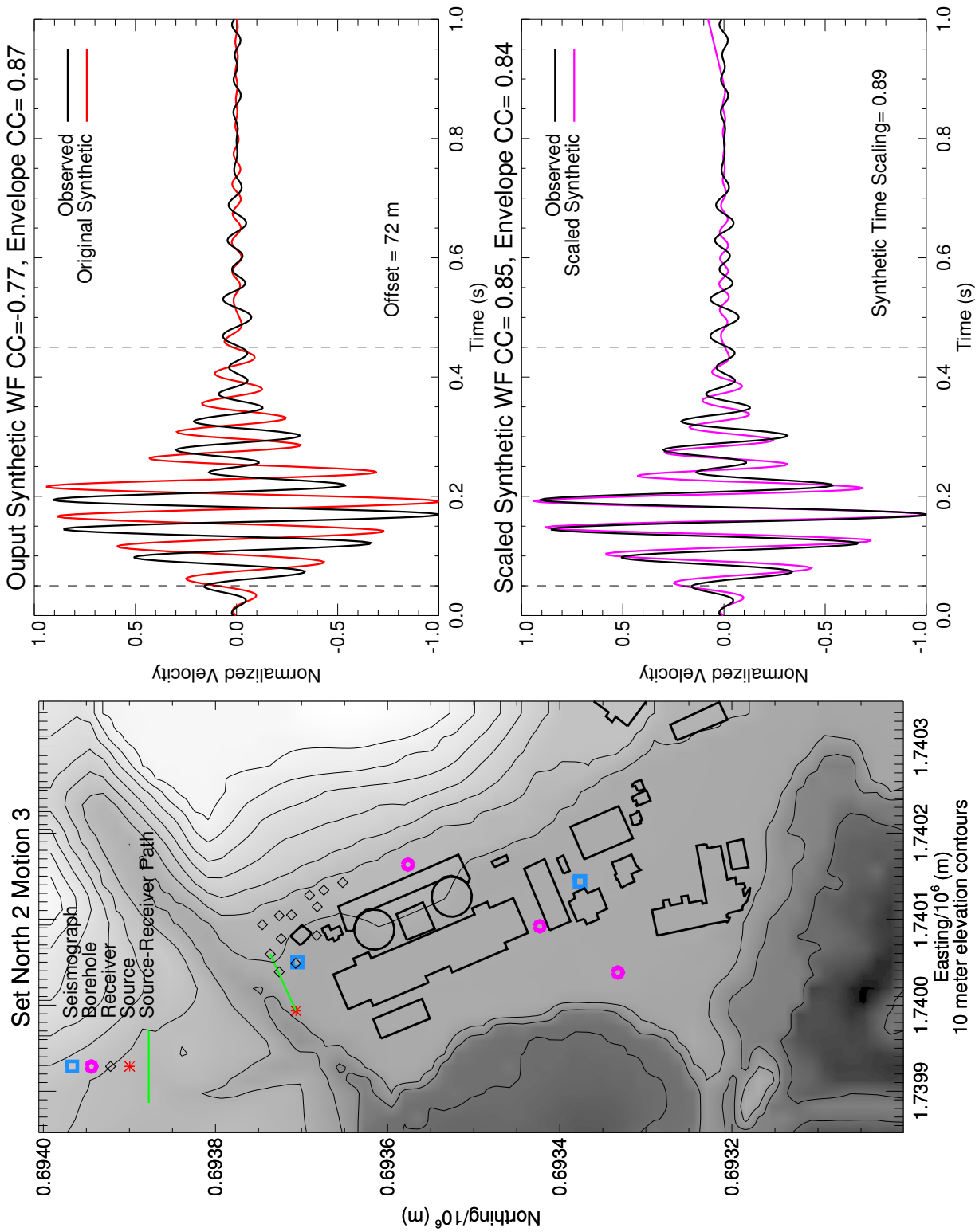

SET NORTH 2 MOTION 3 CROSS−CORRELATION ANALYSIS
Update of the 3−D Velocity Model for the DCPP Foundation Area
San Luis Obispo, California

FIGURE 3.3−26

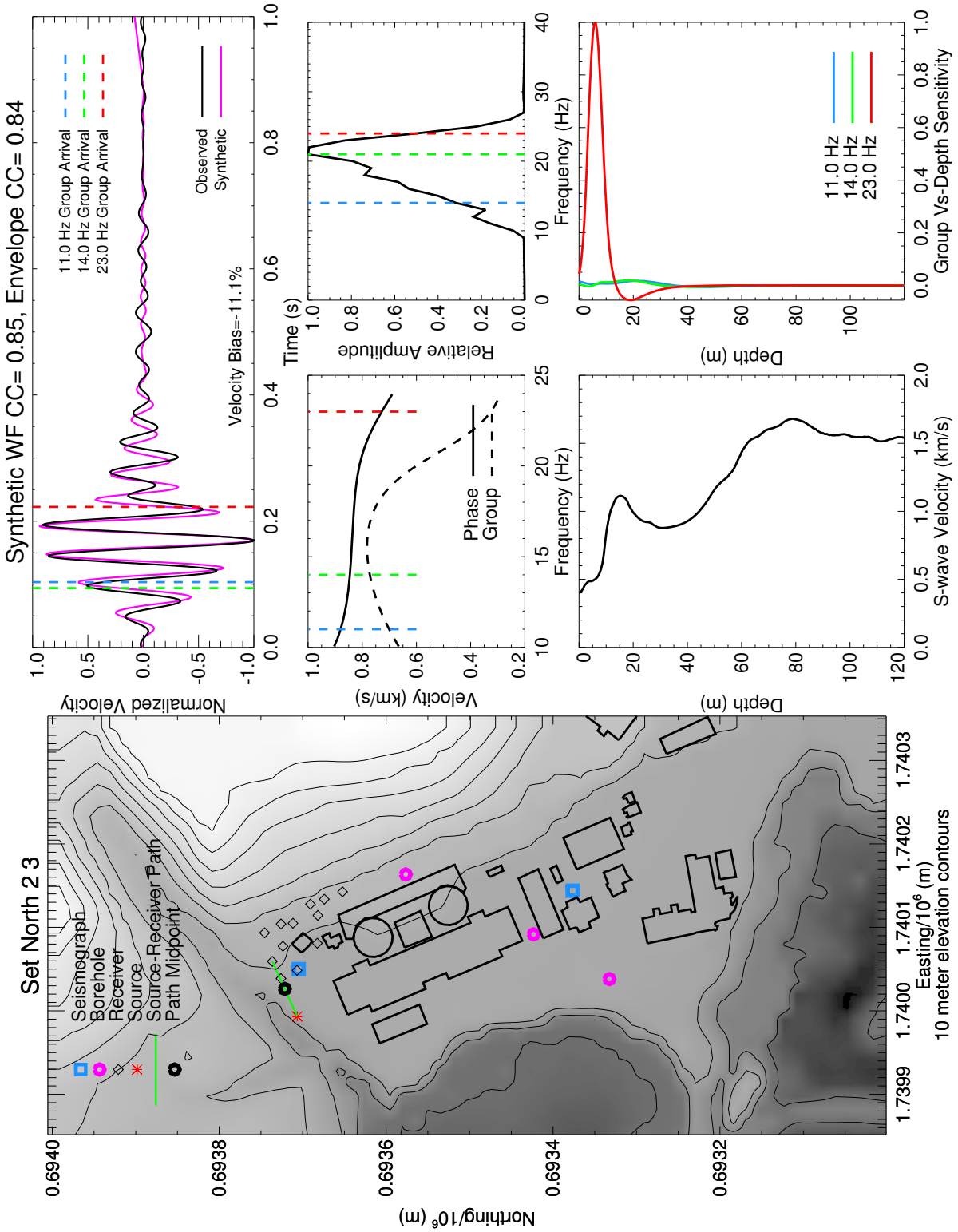

SET NORTH 2 MOTION 3 SENSITIVITY ANALYSIS
Update of the 3−D Velocity Model for the DCPP Foundation Area
San Luis Obispo, California

FIGURE 3.3−27

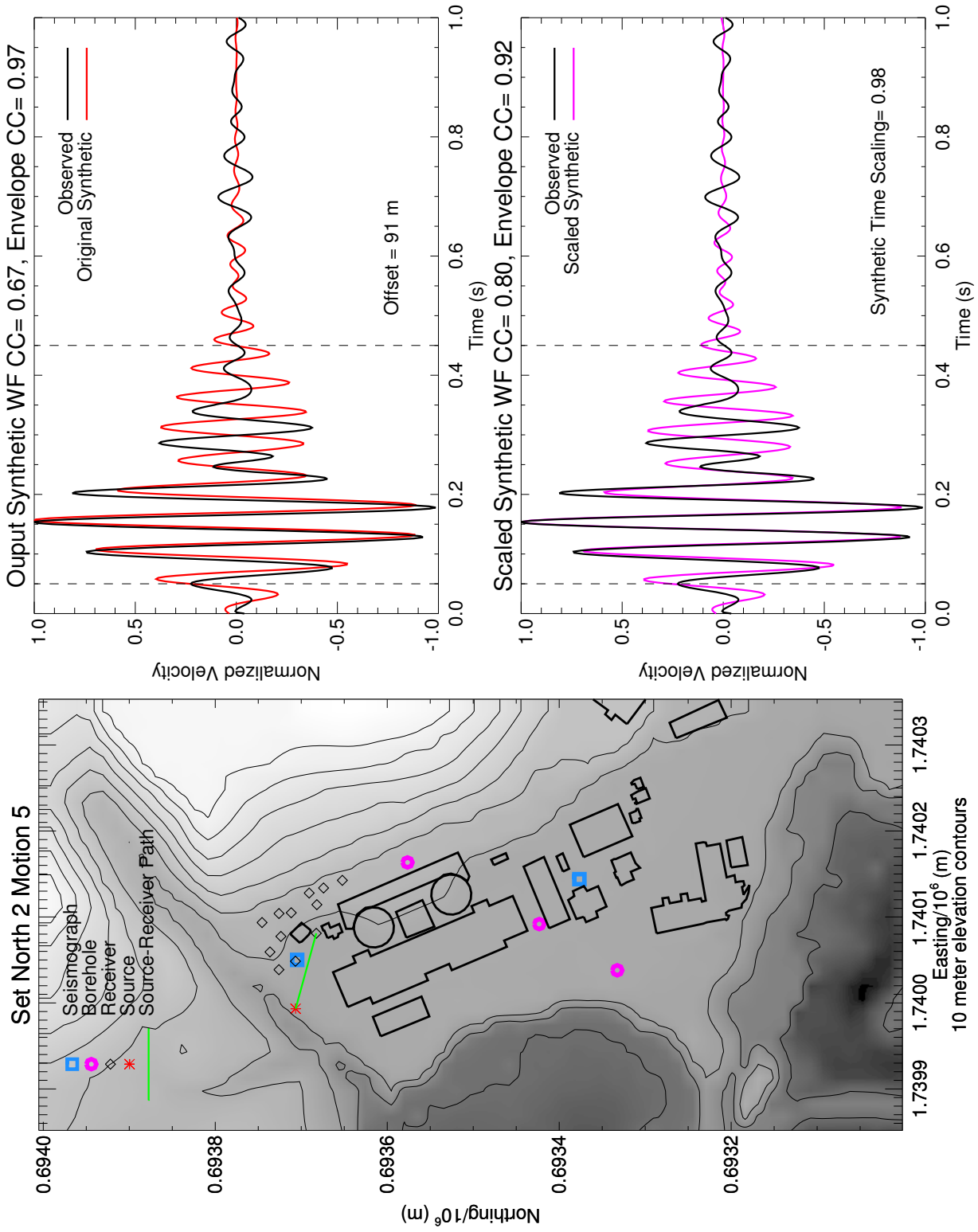

SET NORTH 2 MOTION 5 CROSS−CORRELATION ANALYSIS
Update of the 3−D Velocity Model for the DCPP Foundation Area
San Luis Obispo, California

FIGURE 3.3−28

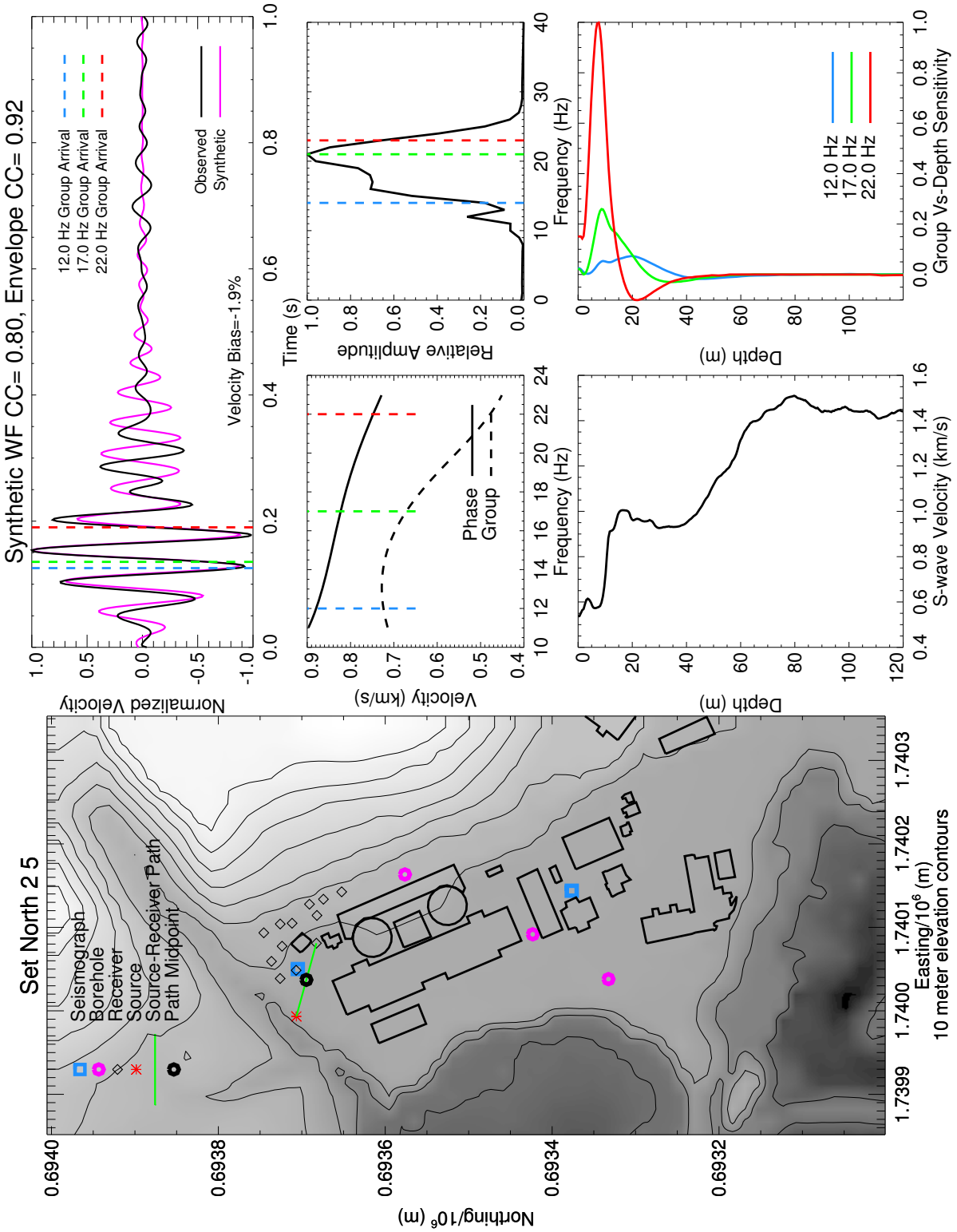

SET NORTH 2 MOTION 5 SENSITIVITY ANALYSIS
Update of the 3−D Velocity Model for the DCPP Foundation Area
San Luis Obispo, California

FIGURE 3.3−29

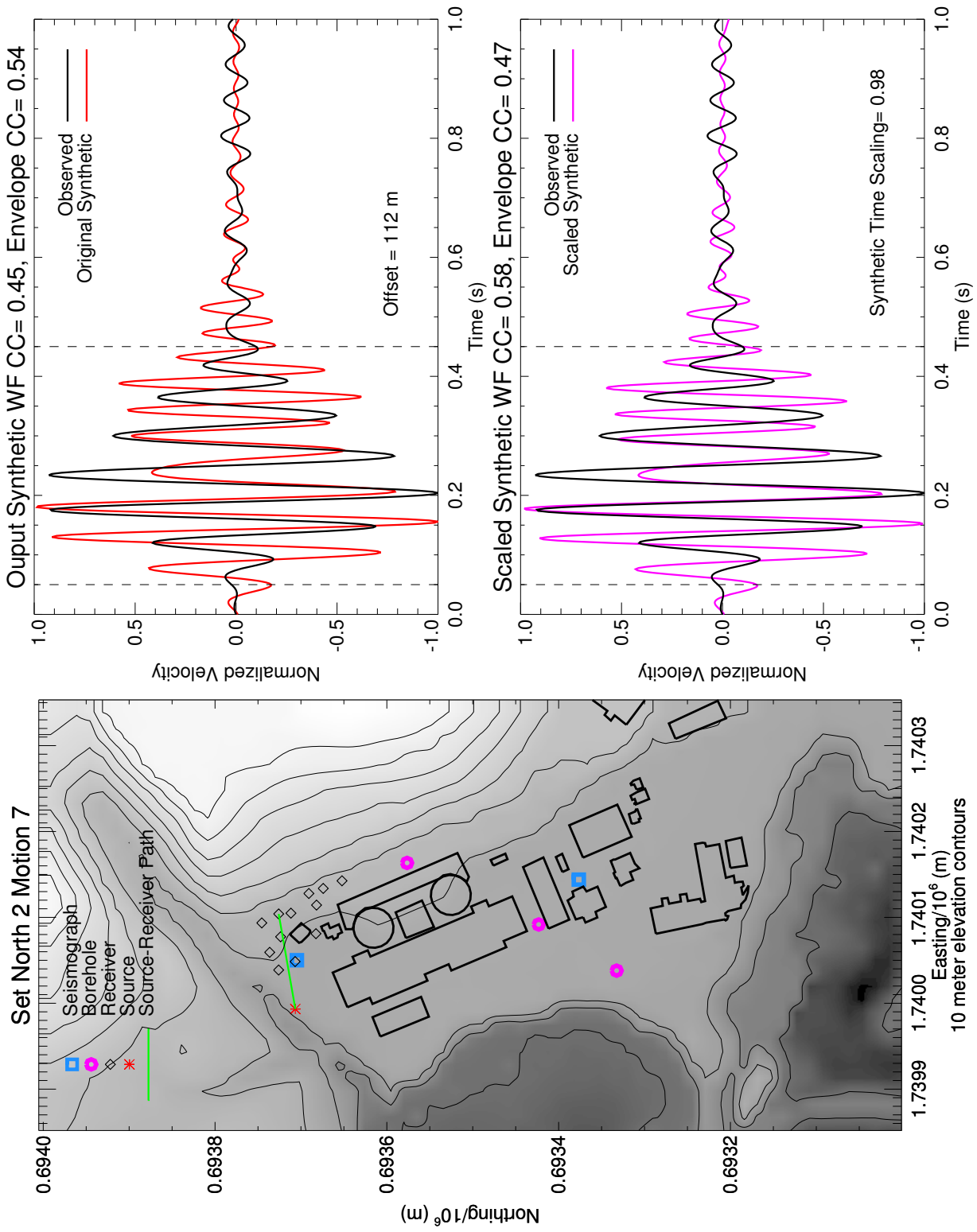

SET NORTH 2 MOTION 7 CROSS−CORRELATION ANALYSIS
Update of the 3−D Velocity Model for the DCPP Foundation Area
San Luis Obispo, California

FIGURE 3.3−30

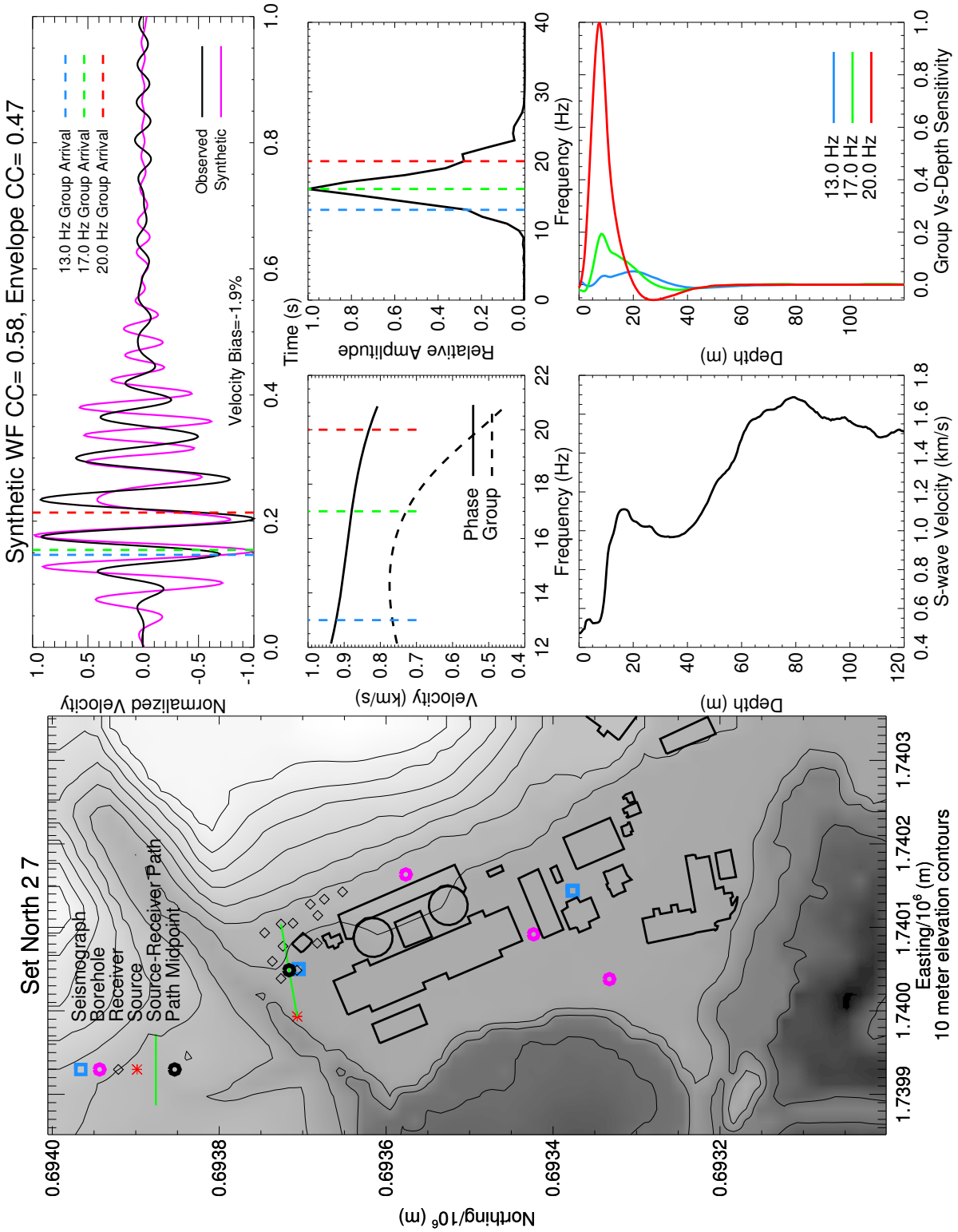

SET NORTH 2 MOTION 7 SENSITIVITY ANALYSIS
Update of the 3−D Velocity Model for the DCPP Foundation Area
San Luis Obispo, California

FIGURE 3.3−31

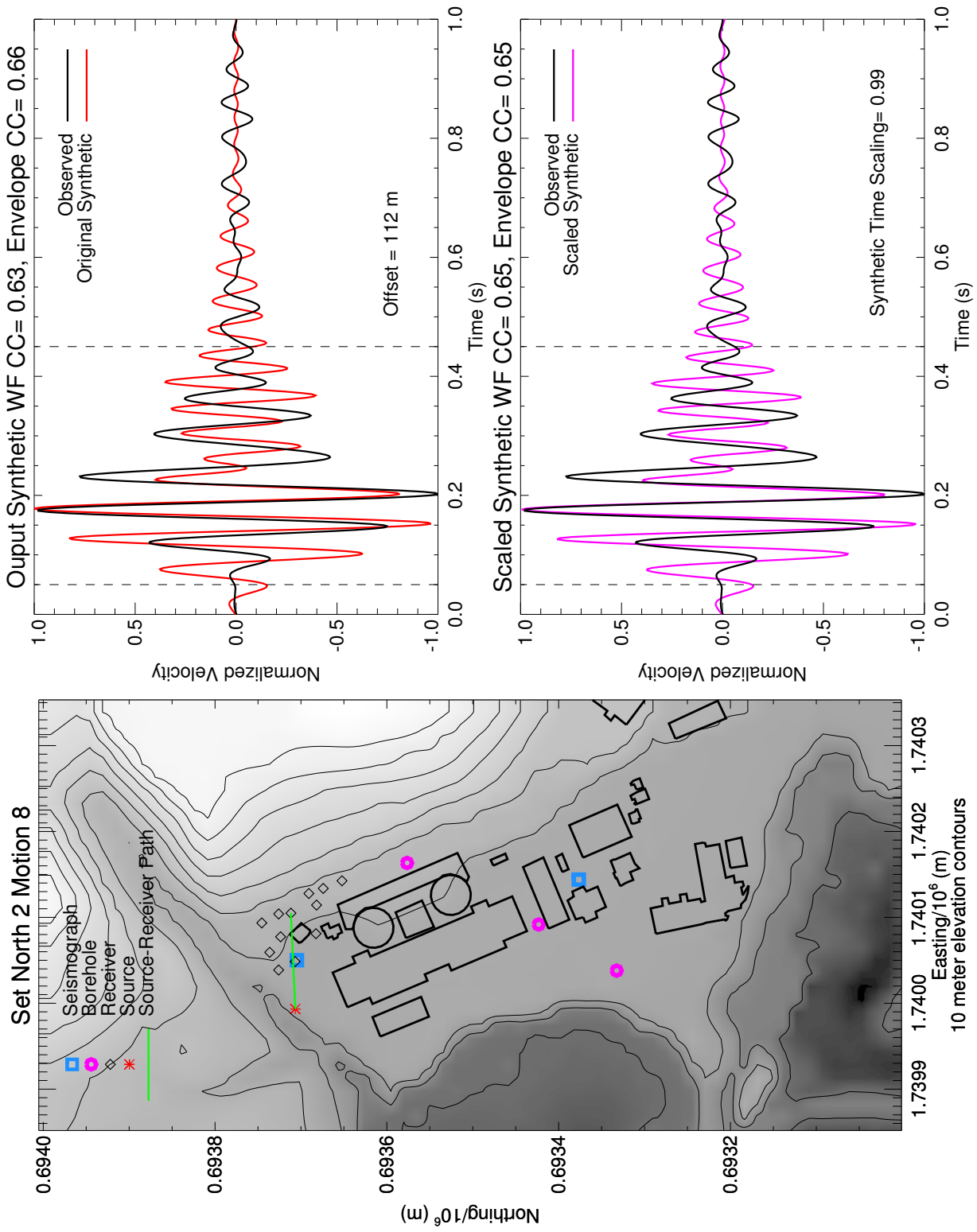

SET NORTH 2 MOTION 8 CROSS−CORRELATION ANALYSIS
Update of the 3−D Velocity Model for the DCPP Foundation Area
San Luis Obispo, California

FIGURE 3.3−32

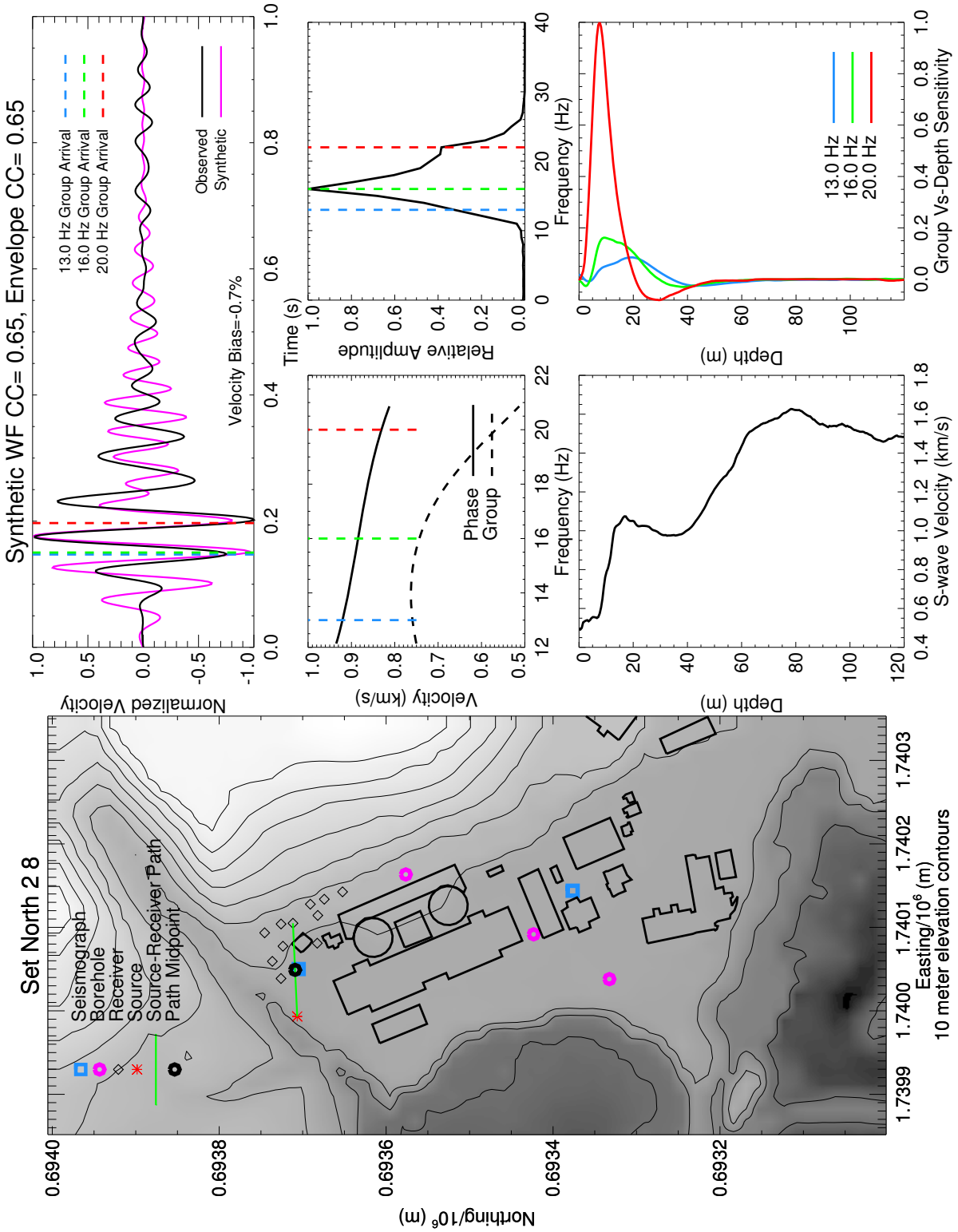

SET NORTH 2 MOTION 8 SENSITIVITY ANALYSIS
Update of the 3−D Velocity Model for the DCPP Foundation Area
San Luis Obispo, California

FIGURE 3.3−33

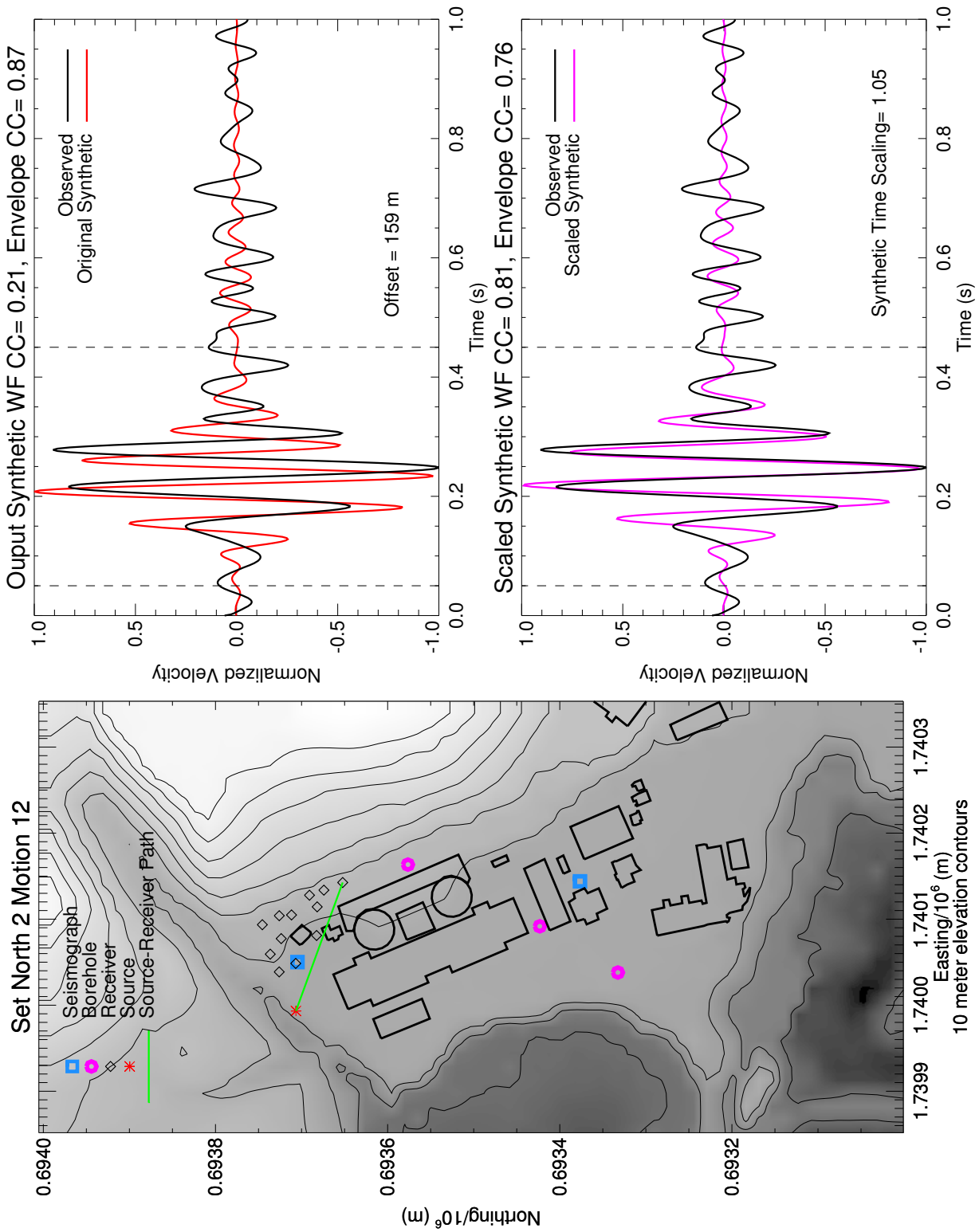

SET NORTH 2 MOTION 12 CROSS−CORRELATION ANALYSIS
Update of the 3−D Velocity Model for the DCPP Foundation Area
San Luis Obispo, California

FIGURE 3.3−34

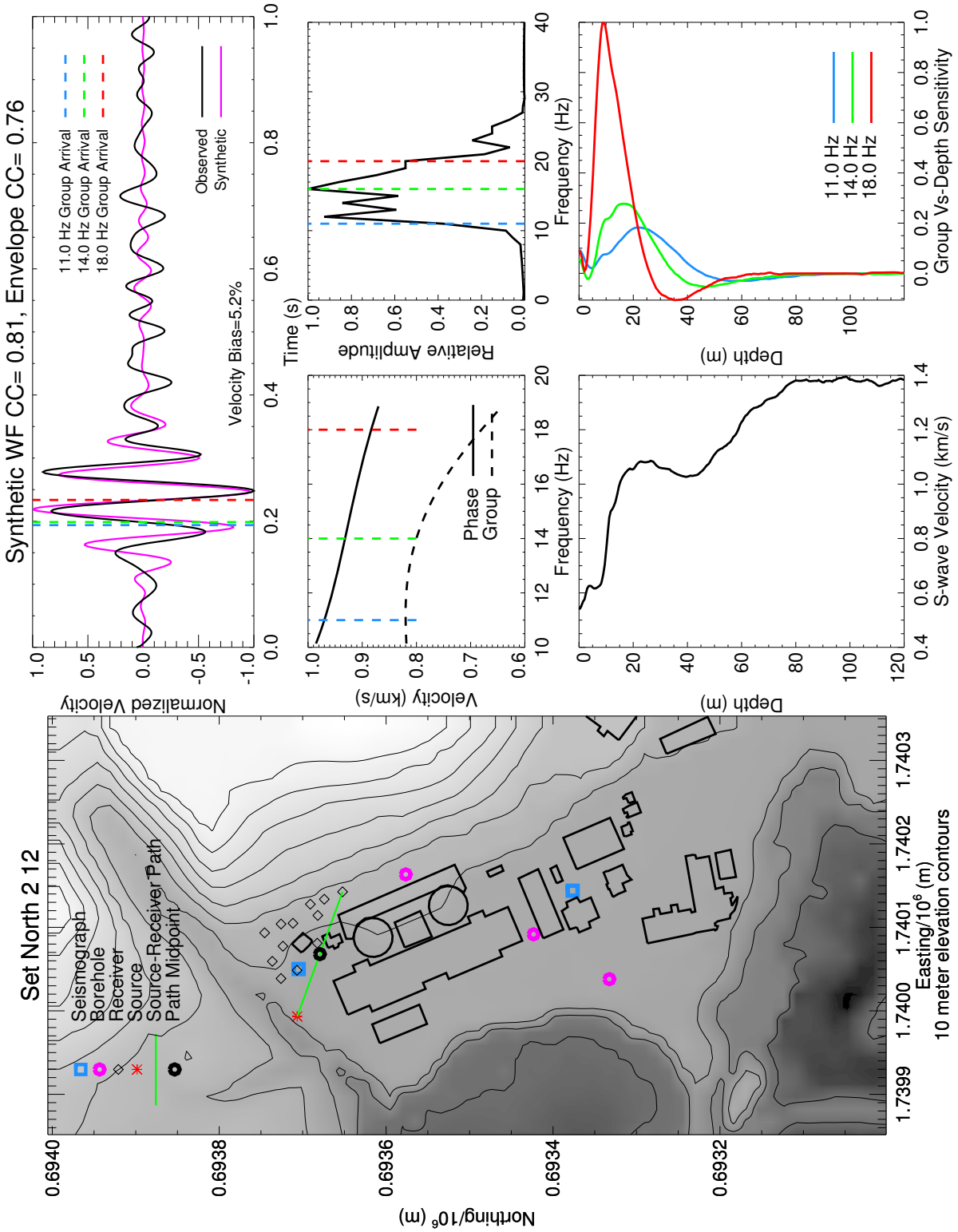

SET NORTH 2 MOTION 12 SENSITIVITY ANALYSIS
Update of the 3−D Velocity Model for the DCPP Foundation Area
San Luis Obispo, California

FIGURE 3.3−35

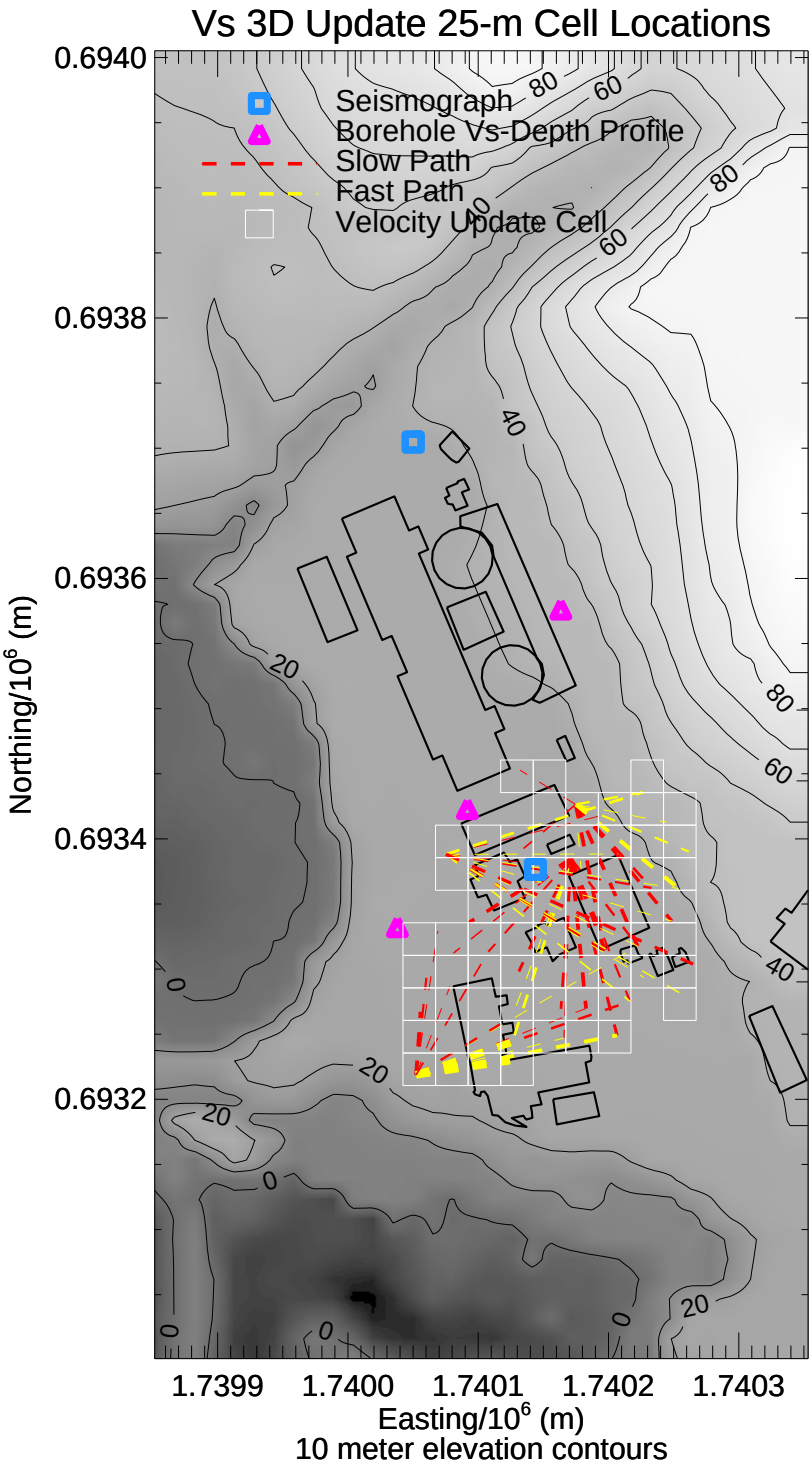

LOCATION OF 2D GROUP−DELAY 25−M TOMOGRAPHY CELLS AND SOURCE−RECEIVER PATHS

Update of the 3−D Velocity Model for the DCPP Foundation Area
San Luis Obispo, California

FIGURE 3.3−36

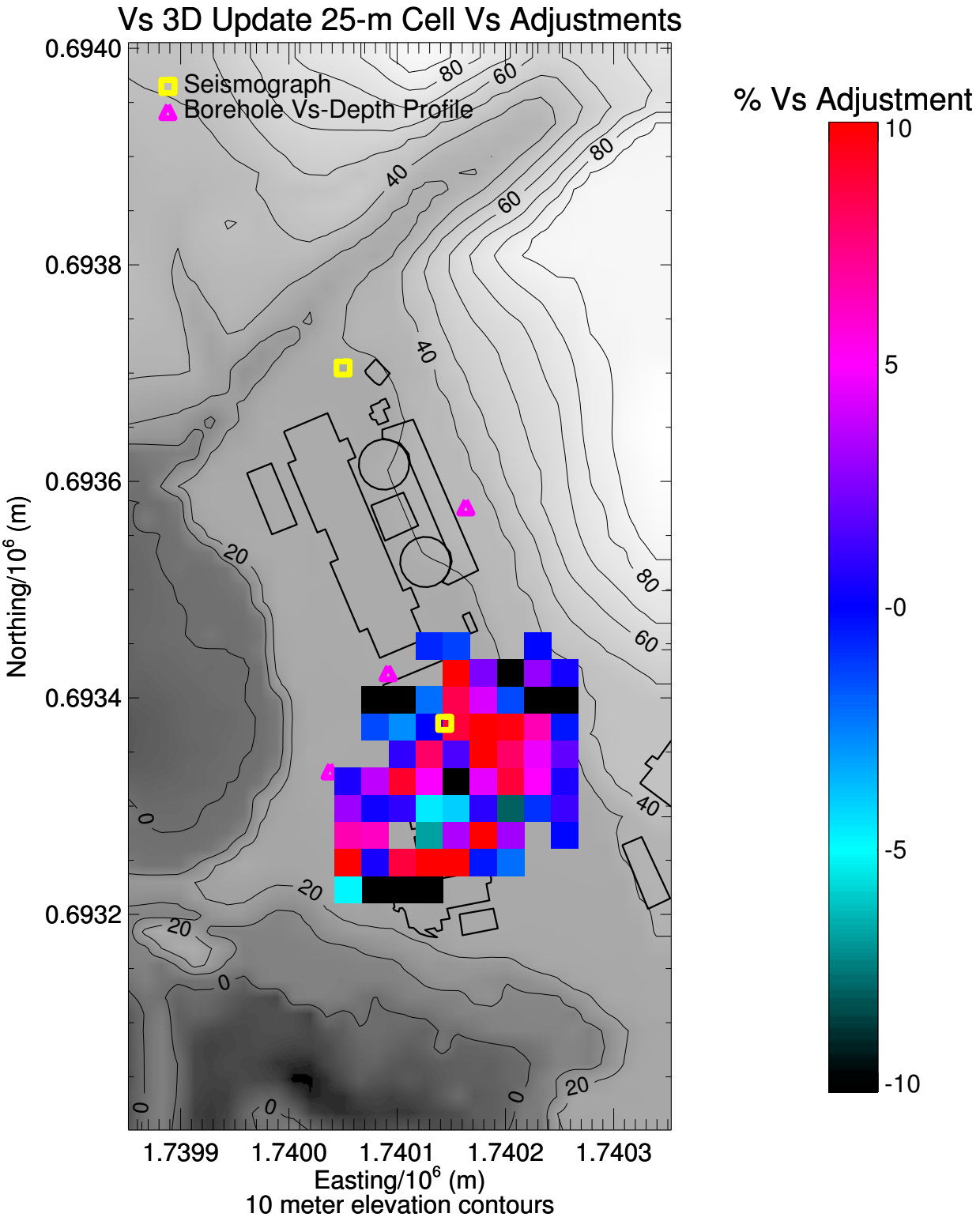

VS ADJUSTMENTS IN THE 25−M TOMOGRAPHY CELLS
Update of the 3−D Velocity Model for the DCPP Foundation Area
San Luis Obispo, California

FIGURE 3.3−37

4.0 DISCUSSION

A comprehensive new set of data and analyses are used to update the DCPP 3-D Vs model. These data directly constrain Vs-depth structure at many locations in the DCPP foundation area. New data and analyses of surface-wave phase-dispersion directly constrain Vs-depth (Kausel and Roesset, 1981) at 100 positions within and around the DCPP foundation area (Figures 2.0-1 and 2.1-2). New analyses of surface-wave phase dispersion using Zland receiver arrays provide comprehensive laterally sampling of large portions of the DCPP foundation (Figure 2.1-6). Vibroseis waveform analyses use 79 source-receiver paths that comprehensively sample beneath and around the two seismic stations with earthquake recordings (Figure 2.1-7). Three downhole shear-wave traveltime measurement data sets (Figure 2.1-1) also provide local constraints on the 3-D Vs structure of the DCPP foundation area. Borehole DDH-B (shown in Figure 2.1-1) doesn't provide Vs data.

The final 3-D DCPP velocity model combines the high-resolution 3-D Vp model derived from joint traveltime-gravity tomography (Fugro, 2014b; Zhou et al., 2014; O'Connell et al., 2014) with an updated 3-D Vs model based on data that directly constrains Vs-depth structure. Uncertainties in the 3-D Vs model are provided in terms of Vs-depth uncertainties for two areas, one containing the DCPP foundation and a second area immediately west of the DCPP foundation extending to the sea cliffs (Figures 2.3-2 and 2.3-5). These Vs uncertainties are based on surface-wave dispersion and Vibroseis waveform modeling tomographic uncertainty analyses that provide quantitative 3-D Vs model uncertainties for site response analyses.

4.1 3-D VS-DEPTH AND DOWNHOLE SHEAR-WAVE TRAVELTIME DATA

Downhole shear-wave traveltime measurements from the three boreholes in the DCPP foundation area are compared to synthetic shear-wave traveltimes from the 3-D Vs model for the portions of the 3-D Vs model within 30 m (< 2 3-D horizontal grid-cell dimensions) of the borehole locations (Figure 4.1-1). The shear-wave arrival time picks in borehole DDH-A-2 southwest of the main DCPP foundation area are all as early or several ms earlier than the earliest shear-wave arrival times of the fastest parts of the 3-D Vs model within 30 m of borehole DDH-A-2 (top of Figure 4.1-1). The synthetic shear-wave traveltimes within 30 m of borehole DDH-C in the top 40 m of DDH-C are very similar to the picked shear-wave traveltimes (middle of Figure 4.1-1). However, picked shear-wave traveltimes in the 40-50 m depth range scatter over 19 ms (0.019) seconds as denoted by the upper double arrow in the borehole DDH-C travel-time-depth plot in Figure 4.1-1, which indicates that it was very difficult to identify the shear-wave first arrival below 40 m depth. Consequently, it appears that shear-wave arrival time picks in borehole DDH-C below 40 m were associated with a peak or trough but not the shear-wave first arrival in borehole DDH-C. Similarly, in borehole DDH-D, shear-wave arrival-time picks are spread over 10 ms (0.01 s) starting at a depth of 55 m (bottom of Figure 4.1-1) and appear to associated with a shear-wave peak or trough that arrivals after the shear-wave first arrival from depths of 55 m and deeper.

The 3-D Vs model Vs-depth profiles within 30 m of boreholes DDH-C and DDH-D have significant low velocity zones (delineated by the horizontal black dashed lines in the middle and bottom Vs-depth profiles in Figure 4.1-2) starting at the depths where there are large scale uncertainties of 0.01-0.02 s in the shear-wave first arrival-time picks in a small depth interval (Figure 4.1-1). Conversely, in borehole DDH-A-2 where shear-wave arrival time picks are single-valued at all depths (top of Figure 4.1-1), there are no significant low-velocity zones (top

of Figure 4.1-2). The difficulties in picking single-values of shear-wave first arrival in the deeper portions of boreholes DDH-C and DDH-D are consistent with attenuation of shear-wave first-arrival energy by the large shear-wave impedances at the top of the large low-velocity zones (Figure 4.1-2), which significantly reduced transmitted shear-wave energy below the top of the low velocity zones. Hence, it became difficult to impossible to consistently pick the first-arrival energy below the top of the deeper low-velocity zones in boreholes DDH-C and DDH-D, so later shear-wave amplitude peaks or troughs were picked instead with comparable apparent velocities (moveout with depth) as the synthetic shear-wave traveltimes (late picks in borehole DDH-C below 40 m depth and in borehole DDH-D below 55 m depth in Figure 4.1-1).

The widest variation in synthetic shear-wave arrival times is observed in borehole DDH-A-2 (Figure 4.1-1) indicating that borehole DDH-A-2 is located in an area with larger lateral variability of Vs in the top 10 m than either of boreholes DDH-C and DDH-D (Figure 4.1-2). If borehole DDH-A-2 is located in an area with significant concrete backfill adjacent to the borehole, the observed shear-wave traveltimes will be systematically faster than the 3-D Vs synthetic traveltimes simply because some traveltime delay associated with soil/backfill/weathering rind will be eliminated by fast concrete. Borehole DDH-A-2 is located adjacent to the buried intake system which does have some buried concrete mats along with steel pipes.

The 3-D Vs-depth structure at and immediately west of borehole DDH-C is verified by Vibroseis waveform modeling (Figures 3.3-24 and 3.3-25) that show the 3-D Vs model is no more than 4% slow because there is a 0.91 waveform cross-correlation of observed and 3-D model synthetic Vibroseis ground motions for the source-receiver path extending from borehole DDH-C to 17 m to the west (Figure 3.3-24) and group-arrival constraints to 50 m depth (as indicated by the group-velocity-depth sensitivity kernels in the lower right plot of Figure 3.3-25). Thus, the observed shear-wave arrival-time distribution uncertainties in borehole DDH-C strongly support the existence of a significant low-velocity zone at borehole DDH-C starting below 40-50 m depth (Figures 4.1-1 and 4.1-2).

The shear-wave downhole arrival-time data from borehole DDH-D constrains Vs-depth just east of the containment structure where there are not direct constraints on Vs-depth from surface-wave dispersion or Vibroseis source-receiver ground motions (Figures 2.0-1, 2.1-2, and 2.1-6). The Vs-depth profile and strong low-velocity zone below 55-m depth in borehole DDH-D are quite similar to the Vs-depth profile near seismic station ESTA 28 north of the DCPP that has phase dispersion Vs-depth sensitivity and resolution to at least 80 m depth (Figure 4.1-3). Both the synthetic DDH-D Vs-depth profile and the Vs-depth profile near ESTA 28 (Figure 4.1-3) have a large Vs gradient from the surface to 25 m depth, moderate velocity increases overall from 25 m depth to 55 m depth is slight velocity reversals, and a low-velocity zone below 55 m depth (Figures 4.1-2 and 4.1-3). All three borehole shear-wave arrival time data sets provide important constraints and observations that are consistent with estimated 3-D Vs-depth in the vicinity of the boreholes (Figure 4.1-1) and strongly support the existence of significant low-velocity zones at depths of 40 m or more in portions of the DCPP foundation area.

4.2 PROBABILISTIC CHARACTERIZATION OF VS-DEPTH IN THE DCPP FOUNDATION AREA

The analyses in Sections 2.0 and 3.0 indicate that the subset of the 3-D Vs model directly below the DCPP foundation area can be laterally averaged to produce ln-mean Vs-

depth and Vs-depth variability to generate 1-D randomized Vs-depth appropriate for sensitivity analyses of DCPP foundation area site response analyses. This is because lateral Vs-depth variability in the DCPP foundation is relatively modest relative to other areas surrounding the DCPP foundation as indicated in Table 3.4-1. Construction of two alternative 3-D Vs-depth models as outlined in Section 3.4 with the weights indicated in Table 3.4-2 provides a first-order approach to evaluate 3-D site response variability.

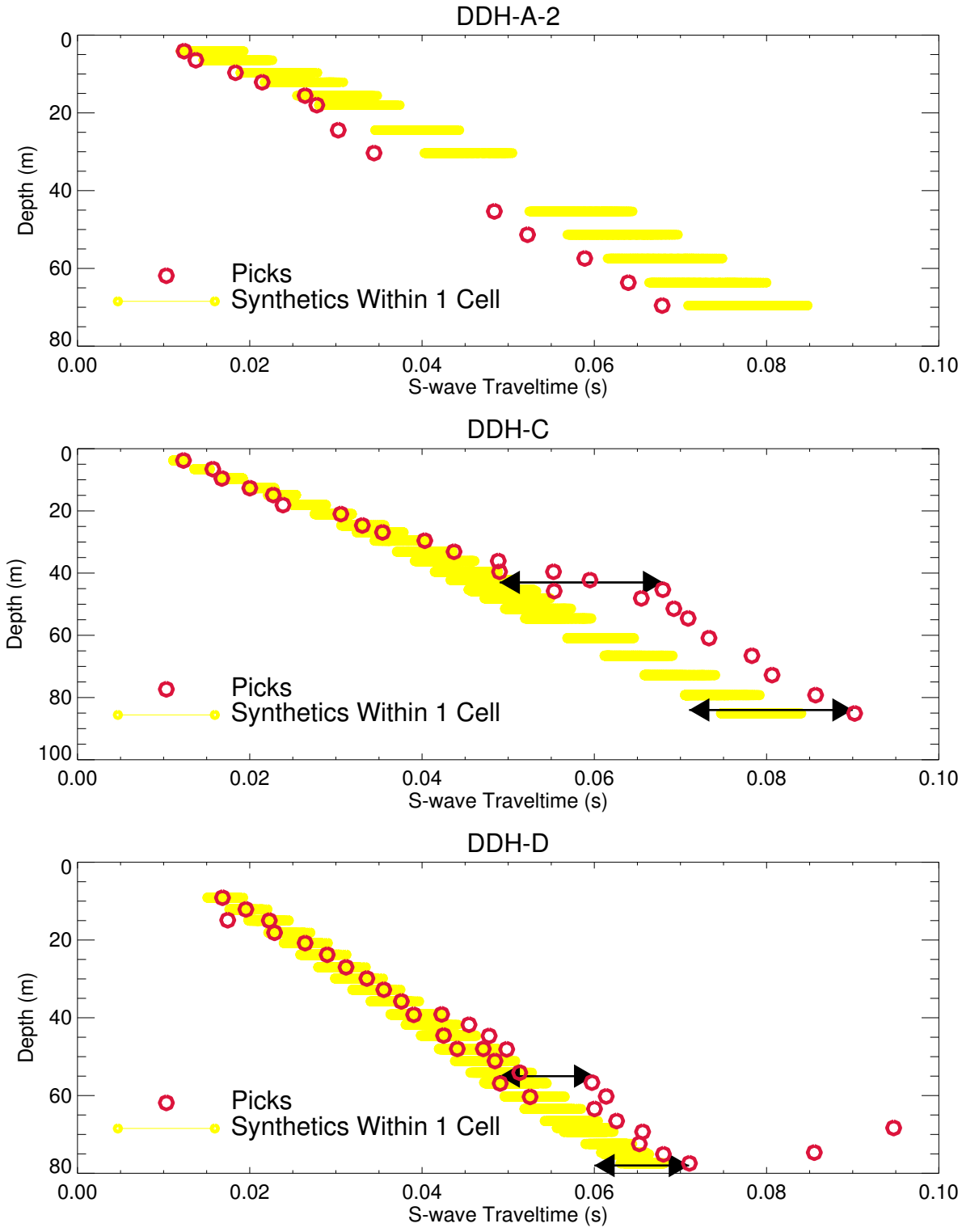

SHEAR−WAVE TRAVELTIMES FROM BOREHOLES DDH−A−2, DDH−C, AND DDH−D (DOUBLE ARROWS SHOW DEPTH RANGES WHERE PICKING UNCERTAINTIES ARE 0.01 S OR MORE)

Update of the 3−D Velocity Model for the DCPP Foundation Area
San Luis Obispo, California

FIGURE 4.1−1

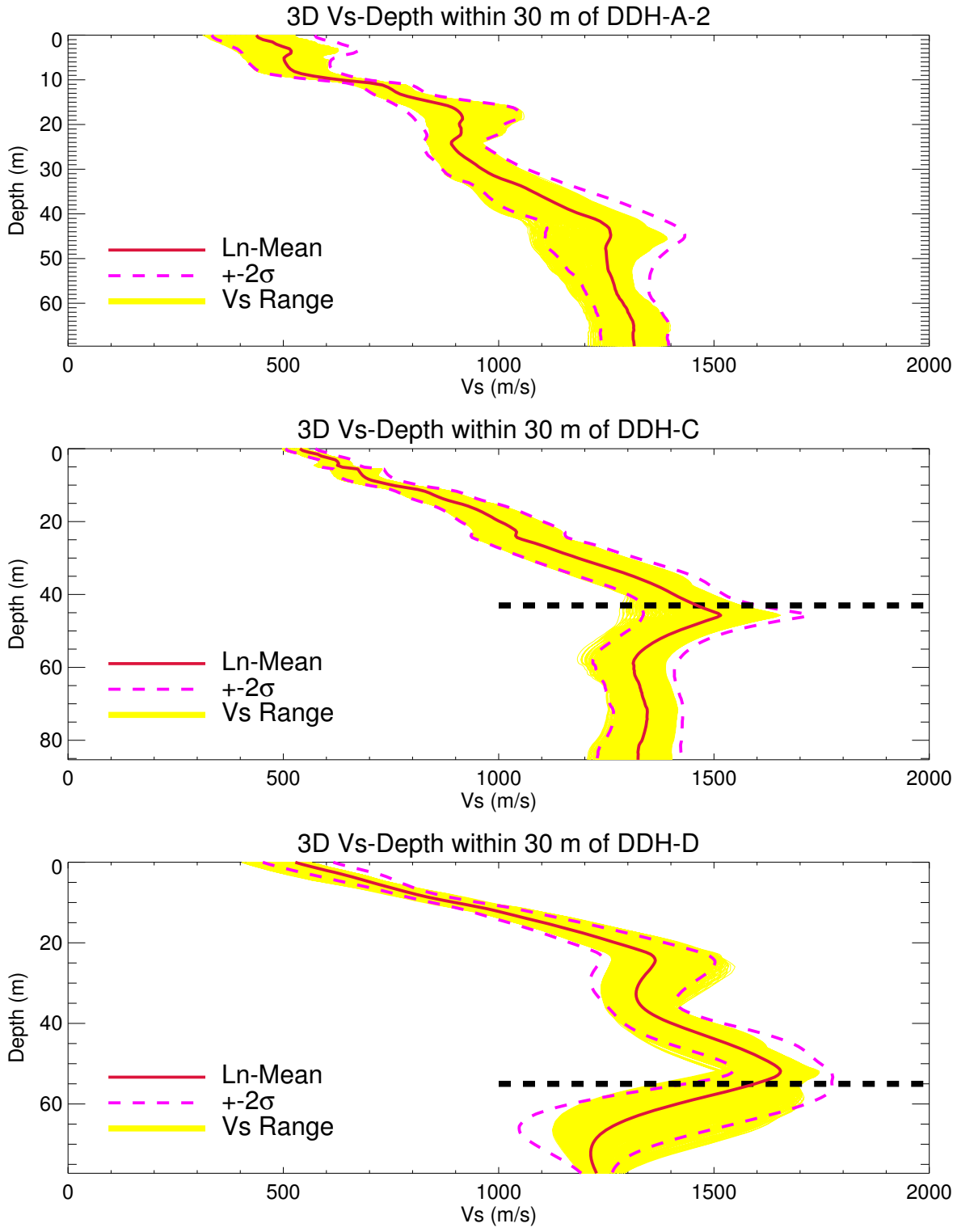

3D VS−DEPTH WITHIN 30 M OF BOREHOLES DDH−A−2, DDH−C, AND DDH−D (BLACK−DASHED LINES DELINEATE DEPTHS WHERE PICK UNCERTAINTIES BECOME LARGE)

Update of the 3−D Velocity Model for the DCPP Foundation Area
San Luis Obispo, California

FIGURE 4.1−2

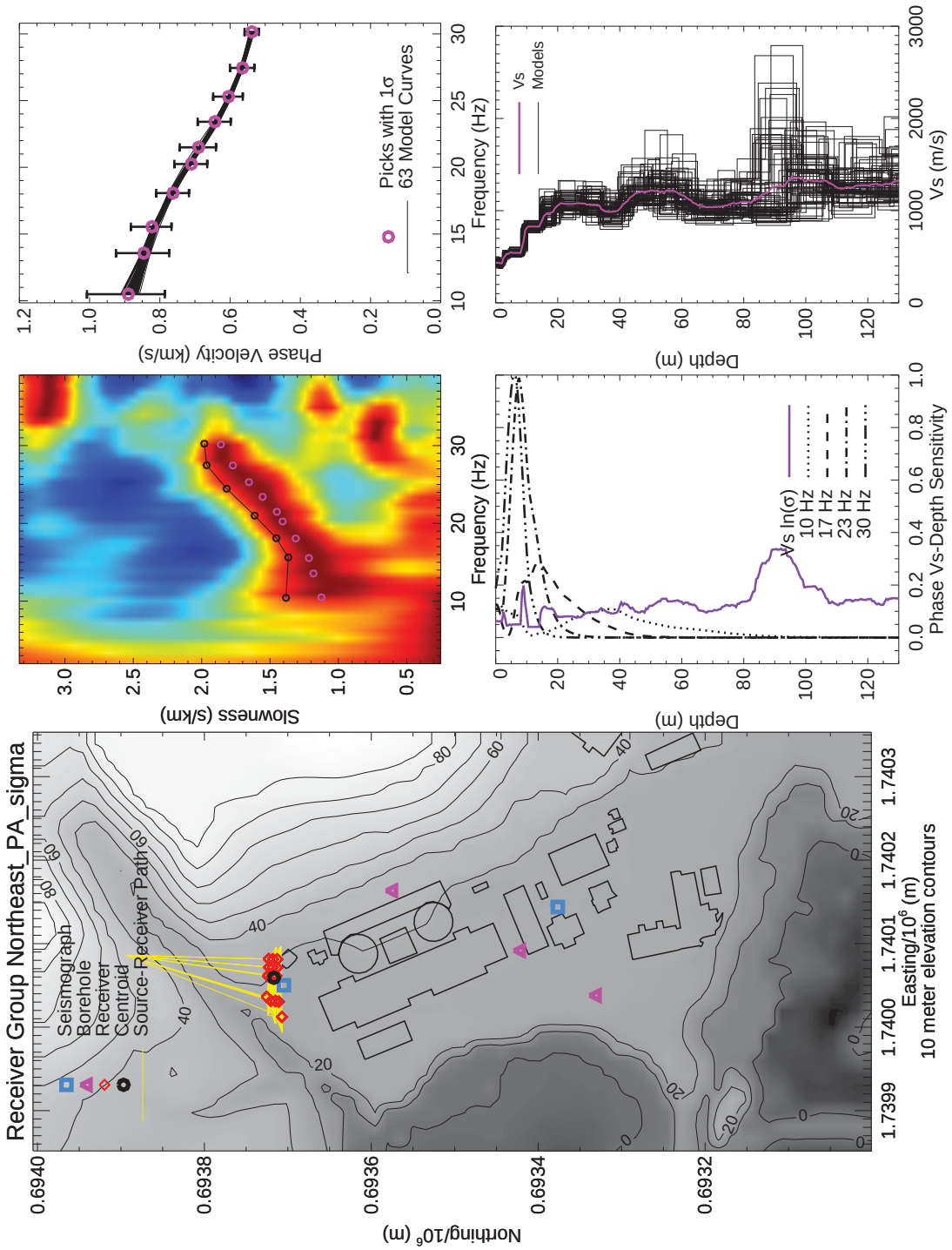

RECEIVER GROUP SIGMA NE PA DISPERSION AND VS−DEPTH ANALYSIS
(A LOW−VELOCITY ZONE STARTS AT 55−60 M DEPTH)
Update of the 3−D Velocity Model for the DCPP Foundation Area
San Luis Obispo, California

FIGURE 4.1−3

5.0 REFERENCES

Agbabian and Associates, 1998, Geophysical Investigations for the DCPP HLW-Dry Cask Storage Facility at the Diablo Canyon Power Plant, Report R9730-6676 to Pacific Gas And Electric Company.

Cartwright, J. and Hansen, D.M. 2006, Magma transport through the crust via interconnected sill complexes. Geology 34, 929-932.

Caterpillar 2000, Handbook of Ripping, http://www.dot.ca.gov/hq/esc/geotech/references/Rock_Cut_Slope_References/31_Handbook_of_Ripping_Caterpiller.pdf

Fugro (2014a), CCCSIP DCPP P- and S-Wave Foundation Velocity Report, Project Report PGEQ-PR-16.

Fugro (2014b), 2011-2012 Onshore 2D-3D Data Processing Report, Project Report PGEQ-PR-08.

Fugro (2015), "3-D Site Response Analyses for Diablo Canyon Power Plant (DCPP)," Report prepared for Pacific Gas and Electric, Fugro Job No. 04.76140022, February.

Galland, O., Planke, S., Neumann, E.R. and Malthe-Sørenssen, A. 2009, Experimental modelling of shallow magma emplacement: Application to saucer-shaped intrusions. Earth and Planetary Science Letters 277: 373-383.

Garofalo, F., Foti, S., Hollender, F., Cornou, C., Bard, P.Y., Cox, B.R., Dechamp, A., Ohrnberger, M., Sicilia, D., Vergniault, C., 2015, The Interpacific Project: an International Cooperative Benchmark for Assessing Reliability and Accuracy of Invasive and Non-invasive Seismic Methods for Site Characterization, Seis. Res. Lett., v. 86, p. 76.

Gressier, J.-P., R. Mourgues, L. Bodet, J.-Y. Matthieu, O.Galland, and P. Cobbold, 2010, Control of pore fluid pressure on depth of emplacement of magmatic sills: An experimental approach, Tectonophysics 489, 1–13.

Hadziioannou, C., E. Larose, O. Coutant, P. Roux, and M. Campillo, 2009, Stability of monitoring weak changes in multiply scattering media with ambient noise correlation: Laboratory experiments, J. Acoust. Soc. Am., 125(6), 3688–3695.

Hansen, D.M. and Cartwright, J.A 2006a, The three-dimensional geometry and growth of forced folds above saucer-shaped igneous sills. Journal of Structural Geology 28: 1520-1535.

Hansen, D.M. and Cartwright, J.A. 2006b, Saucer-shaped sill with lobate morphology revealed by 3D seismic data: implications for resolving a shallow-level sill emplacement mechanism. Journal of the Geological Society, London 163: 509-523.

Itasca (2014a), "FLAC Fast Lagrangian Analysis of Continua, User's Guide", Itasca Consulting Group Inc., version 7.0.422.

Itasca (2014b), "FLAC3D Fast Lagrangian Analysis of Continua in 3 Dimensions, User's Guide", Itasca Consulting Group Inc., version 5.01.129.29607.

Kausel, E., and J. M. Roesset, 1981, Matrices for layered soils, Bulletin Seismological Society of America, Vol. 71, No. 6, 1743-1761.

Lamb, H. (1904), “On the Propagation of Tremors over the Surface of an Elastic Solid,” in Philosophical Transactions of the Royal Society of London, A203, pp 1-42.

Malthe-Sørenssen, A., Planke, S., Svensen, H. and Jamtveit, B., 2004, Formation of saucer-shaped sills. In: Physical geology of high-level magmatic systems, Breitkreuz, C., and Petford, N., eds., Geological Society, London, Special Publication 234: 215-227.

Nasseri-Moghaddam, A. (2006), “Study of the Effect of Lateral Inhomogeneities on the Propagation of Rayleigh Waves in an Elastic Medium,” Ph.D. Thesis presented to the University of Waterloo, Waterloo, Ontario, Canada.

Nasseri-Moghaddam, A., Cascante, G., Phillips, C., and Hutchinson, D.J. (2007), “Effects of Underground Cavities on Rayleigh Waves – Field and Numerical Experiments,” Soil Dynamics and Earthquake Engineering, No. 27, pp 300-313.

O’Connell, D.R.H., and Turner, J.P., 2011, Interferometric multichannel analysis of surface waves (IMASW), Bulletin Seismological Society of America, Vol. 101, No. 5, pp. 2122-2141

O’Connell, D.R.H., K. Brock, G. Stankovic, N., D. Zhou, and W. Wang, 2014, Depth imaging with crooked 2D and irregular 3D seismic data in rugged terrain, SEG Technical Program Expanded Abstracts 2014: pp. 4294-4298. http://dx.doi.org/10.1190/segam2014-1651.1.

Pacific Gas and Electric Co. (PG&E), 1989, “Diablo Canyon Long Term Seismic Program, Diablo Canyon Power Plant, Docket Nos. 50-275 and 50-323,” Response to Questions 431, Volume 4 of 5, Attachment Q43i-4.

Pacific Gas and Electric Co. (PG&E), 2014a, Geologic Mapping and Data Compilation for the Interpretation of Onshore Seismic-Reflection Data, PG&E Geosciences Department Technical Report Number GEO.DCPP.TR.13.03, Final Draft submitted 1/21/2014, 70 pages, two plates, and five appendices.

Pacific Gas and Electric Co. (PG&E), 2014b, "Central Coastal California Seismic Imaging Project Report to the California Public Utilities Commission," Enclosure to PG&E Letter DCL-14-081, "Central Coastal California Seismic Imaging Project, Shoreline Fault Commitment," dated September 10, 2014.

Poulteau, S., Mazzini, A., Galland, O., Planke, S. and Malthe-Sørenssen, A. 2008, Saucer-shaped intrusions: Occurrences, emplacement and implications. Earth and Planetary Science Letters 266: 195-204.

Rocchi, S., Mazzotti, A., Marroni, M., Pandolfi, L., Constantini, P., Giuseppe, B., di Biase, D., Federici, F. and Lo, P.G. 2007, Detection of Miocene saucer-shaped sills (offshore Senegal) via integrated interpretation of seismic, magnetic and gravity data. Terra Nova 19: 232-239.

Santamarina, J.C., Klein, K.A., and Fam, M.A. (2001), “Soils and Waves,” John Wiley and Sons, Ltd.

Wathelet, M., 2008, An improved neighborhood algorithm: parameter conditions and dynamic scaling. Geophysical Research Letters, 35, L09301

Wathelet, M., D. Jongmans, and M. Ohrnberger, 2004, Surface wave inversion using a direct search algorithm and its application to ambient vibration measurements, Near Surface Geophysics 2, 211—221

William Lettis and Associates (WLA), 2001, Diablo Canyon ISFSI Data Report B: Borings in the ISFSI Site Area, Rev 0.

Yang, Y. (2009), “Nondestructive Evaluation of the Depth of Cracks in Concrete Plates Using Surface Waves,” Ph.D. Thesis presented to the University of Waterloo, Waterloo, Ontario, Canada.

Zhou, D., W. Wang , J. Zhang , and D.R.H. O'Connell, 2014. 3D joint inversion of seismic traveltime and gravity data: A case study. SEG Technical Program Expanded Abstracts 2014: pp. 3148-3152. http://dx.doi.org/10.1190/segam2014-1556.1